arXiv:1206.0738v1 [astro-ph.EP] 4 Jun 2012

To appear in *Planets, Stars and Stellar Systems*, ed. P. Kalas & L. French

From Disks to Planets

Andrew N. Youdin and Scott J. Kenyon
Smithsonian Astrophysical Observatory

Contents

1 INTRODUCTION **2**

2 OBSERVATIONAL CONSTRAINTS ON PLANET FORMATION THEORIES **2**
2.1 Lessons from the Solar System . . . 2
2.1.1 The Solar Nebula . . . 3
2.1.2 Isotopic Timescales . . . 5
2.1.3 Water . . . 6
2.2 Disks Surrounding the Youngest Stars . . . 6
2.3 The Exoplanet Revolution . . . 8

3 DISK PROPERTIES AND EVOLUTION **9**
3.1 Basic Disk Dynamics . . . 10
3.2 Transport Mechanisms and the α Disk Model . . . 12
3.3 Viscously Heated Disks . . . 13
3.4 Steady Irradiated Disks . . . 16
3.5 Time Dependence . . . 17
3.6 Disk Instabilities and Fragmentation . . . 18

4 FROM DUST TO PLANETESIMALS **19**
4.1 The "Meter-Size" Barrier . . . 20
4.1.1 Radial Drift and the Basics of Disk Aerodynamics . . . 20
4.1.2 Early Collisional Growth . . . 22
4.2 Gravitational Collapse of Solids into Planetesimals . . . 24
4.3 Aerodynamic Particle Concentration . . . 26
4.4 Observational Constraints on Planetesimal Formation . . . 28

5 PLANETESIMALS TO PLANETS **30**
5.1 Growth of Solid Protoplanets . . . 30
5.1.1 Basic Length and Velocity Scales . . . 31
5.1.2 Gravitationally Focused Collisions . . . 32
5.1.3 Planetesimal Velocity Evolution . . . 35
5.1.4 Fragmentation . . . 37
5.1.5 Planetesimal Accretion with Gas Damping . . . 38
5.1.6 Numerical Simulations of Low Mass Planet Formation . . . 40
5.2 Accretion of Atmospheres . . . 42

5.2.1 Static Protoplanet Atmospheres 42
5.2.2 Enhanced Planetesimal Accretion 44
5.2.3 The Core Accretion Instability 44
5.2.4 Direct Accretion of Disk Gas (and How it Stops) 47
5.2.5 Numerical Simulations of Gas Giant Planet Formation 47
5.3 Direct Formation of Brown Dwarfs and Gas Giants 48

6 SUMMARY **50**

1. INTRODUCTION

Theories for the formation and evolution of planets depended primarily on geophysical data from the Solar System (see Brush 1990, and references therein). Starting in the 1940's, astrophysical data began to provide new insights. Discoveries of pre-main sequence stars in Taurus-Auriga, Orion, and other regions led to the concept that stars form in giant clouds of gas and dust (see Kenyon et al. 2008b, and references therein). Because nearly every young star has a circumstellar disk with enough mass to make a planetary system, theorists began to connect the birth of stars to the birth of planets. Still, the Solar System remained unique until the 1990's, when the first discoveries of exoplanets began to test the notion that planetary systems are common. With thousands of (candidate) planetary systems known today, we are starting to have enough examples to develop a complete theory for the origin of the Earth and other planets.

Here, we consider the physical processes that transform a protostellar disk into a planetary system around a single star. Instead of discussing the astrophysical and geophysical data in detail (e.g., Dauphas & Chaussidon 2011), we focus on a basic introduction to the physical steps involved in building a planet. To begin, we discuss several observational constraints from the wealth of astrophysical and geophysical material in §2. We then describe the global physical properties and evolution of the disk in §3. Aside from the special conditions required for fragments in the disk to collapse directly into giant planets (§5.3), most planets probably grow from micron-sized dust grains. Thus, we consider how a turbulent sea of grains produces the building blocks of planets, planetesimals (§4), and how ensembles of planetesimals collide and merge into planets which may later accrete a gaseous atmosphere (§5). We conclude with a brief summary in §6.

2. OBSERVATIONAL CONSTRAINTS ON PLANET FORMATION THEORIES

We begin with the main observational constraints on planet formation processes, including raw materials, timescales, and outcomes. Detailed studies of the Solar System and the disks around the youngest stars yield strict limits on the mass available and the time required to make a planetary system. The diverse population of exoplanets illustrate the many outcomes of planet formation.

2.1. Lessons from the Solar System

Until the discovery of exoplanets, the Solar System was the only known planetary system. The Solar System will continue to provide the most detailed data on planet formation, despite obvious

issues of statistical significance and anthropic bias.

2.1.1. The Solar Nebula

The alignment of major planets in the ecliptic plane suggests that they formed within a flattened disk or "nebula." The philosopher Immanuel Kant and the mathematician Pierre-Simon Laplace are often credited for this "nebular hypothesis." However, the scientist and theologian Emanuel Swedenbourg first recorded this insight in his 1734 *Principia*. For a long time the nebular hypothesis competed with the theory, proposed by the naturalist Buffon, that planets were tidally extracted from the Sun during an encounter. Though Laplace dismissed the encounter theory as being inconsistent with the circular orbits of the planets, it survived to reach peak popularity in the early 20th century as the Chamberlin-Moulton hypothesis (Jeffreys 1929). Once Payne (1925, 1925b) identified hydrogen as the most abundant element in stars, the nebular hypothesis regained favor. Adding the tidal theory's idea of planetesimals – small solid particles that condense out of hot gas – the nebular hypothesis began to develop into a robust theory for planet formation.

The minimum mass solar nebula (MMSN) provides a simple estimate of the mass available in planet forming disks. The recipe for the MMSN is to distribute the mass currently in the solar system's planets into abutting annuli, adding volatile elements (mainly hydrogen gas) until the composition is Solar. Kuiper (1951) and Cameron (1962, see his Table 5) estimated the mass of the MMSN as a few percent of a solar mass. Weidenschilling (1977b) and Hayashi (1981) fit the now canonical $R^{-3/2}$ surface density law, bravely smoothing the mass deficits in the regions of Mercury, Mars, and the asteroid belt, and the abundance uncertainties for the giant planets. The roughness of the fit is immaterial: the MMSN is not a precise initial condition, but a convenient fiducial for comparing disk models.

We use the same MMSN as Chiang & Youdin (2010) with disk surface density profiles:

$$\Sigma_{\rm g} = 2200\, F \left(\frac{R}{\rm AU}\right)^{-3/2} \ {\rm g\,cm^{-2}} \tag{2-1}$$

$$\Sigma_{\rm p} = 33\, F\, Z_{\rm rel} \left(\frac{R}{\rm AU}\right)^{-3/2} \ {\rm g\,cm^{-2}}\,, \tag{2-2}$$

where subscripts "g" and "p" respectively denote gas and particles (condensed solids) and R is the distance from the Sun. The parameter F scales the total mass; $F = 1$ is a reference MMSN. Integrated out to 100 AU, the MMSN disk mass is $0.03 M_\odot$.

The parameter $Z_{\rm rel}$ scales the ratio of solids-to-gas, or disk metallicity as

$$Z_{\rm disk} = \Sigma_{\rm p}/\Sigma_{\rm g} = 0.015 Z_{\rm rel}\,, \tag{2-3}$$

evolves during the planet formation process, as evidenced by the enrichment of heavy elements relative to H in Jupiter and Saturn. Our fiducial value is normalized to the Lodders (2003) analysis

of (proto-)Solar abundances, which can be approximately summarized as:

$$Z_{\rm rel} \simeq \begin{cases} 1 & T \lesssim 40\,{\rm K} \\ 0.78 & 40\,{\rm K} \lesssim T \lesssim 180\,{\rm K} \\ 0.33 & 180\,{\rm K} \lesssim T \lesssim 1300 \text{ — } 2000\,{\rm K} \\ 0 & T \gtrsim 1300 \text{ — } 2000\,{\rm K} \end{cases} . \tag{2-4}$$

The abundance of solids decreases with increasing temperature due to the sublimation of (most significantly) methane ice above 40 K, water ice above 180 K, and dust over a range of temperatures from roughly 1300 — 2000 K, covering the condensation temperatures for different minerals. Note that this definition of disk metallicity ignores the heavy elements in the gas phase, which are at least temporarily unavailable to produce planetary cores. For the disk temperature, this work adopts eq. (3-29), the result for an irradiated disk with a self-consistently flared surface (Chiang & Goldreich 1997).

In the Solar System today, the temperatures of solids are set by an equilibrium between heating and cooling. Although gravitational contraction (Jupiter) and tidal heating (many satellites, including the Moon) contribute some heating in a few objects, the Sun is the primary source of heating. Radiation from the Sun peaks at a wavelength of $\lambda_{max,\odot} \approx 0.5$ μm. Objects with radius r, peak wavelength $\lambda_{max,g} < r$, and no atmosphere radiate as nearly perfect blackbodies. Equating the energy they receive from a central star ($\pi r^2 {\rm L}_\star / 4\pi R^2$) with the energy they emit ($4\pi r^2 \sigma_{\rm SB} T_{eq,bb}^4$) leads to an equilibrium temperature ,

$$T_{eq,bb} = 278 \left(\frac{{\rm L}_\star}{{\rm L}_\odot} \right)^{1/4} \left(\frac{R}{\rm AU} \right)^{-1/2} \ {\rm K} \ , \tag{2-5}$$

where $\rm L_\odot$ is the luminosity of the Sun. Small grains with $r \gtrsim 1$ μm and $r \lesssim \lambda_{max,g}$ emit radiation inefficiently. In most cases, the radiative efficiency is

$$\epsilon = \begin{cases} 1 & \lambda \leq \lambda_0 \\ (\lambda/\lambda_0)^q & \lambda > \lambda_0 \end{cases} , \tag{2-6}$$

where λ_0 is the critical wavelength and $q \approx 1$–2 depends on grain properties. Usually λ_0 is roughly equal to the grain radius r. Because they can only radiate efficiently at short wavelengths, these grains have much larger temperatures. For $q = 1$,

$$T_{eq,s} = 468 \left(\frac{{\rm L}_\star}{{\rm L}_\odot} \right)^{1/5} \left(\frac{R}{\rm AU} \right)^{-2/5} \left(\frac{\lambda_0}{\mu{\rm m}} \right)^{-1/5} \ {\rm K} \ . \tag{2-7}$$

To derive eq. (2-7), include the efficiency in the grains' emitted radiation ($\propto 1/\epsilon$) and relate the wavelength of peak emission to the grain temperature with Wein's Law ($\lambda \propto 1/T_{eq,s}$).

Coupled with the condensation temperatures in eq. (2-4), these definitions allows us to identify the "snow line." Also known as the "frost line," this annulus in the disk[1] which separates an inner region of rocky objects from an outer region of icy objects (Kennedy & Kenyon 2008). For

[1] or, more generally, a spherical shell surrounding the central star

blackbody grains, the water condensation temperature of 180 K implies $R_{snow} \approx 2.7$ AU, roughly coincident with the asteroid belt. Similarly, the methane condensation temperature of 40 K yields another region beyond the outer edge of the Kuiper belt at 48 AU where solid objects have a combination of water and methane ice. Inside of ~ 0.1 AU, dust evaporates; rocky grains cannot exist so close to the Sun.

2.1.2. Isotopic Timescales

Meteorites delivered to Earth from the asteroid belt provide the most detailed chronology of the early Solar System (e.g., Dauphas & Chaussidon 2011). Primitive meteorites from asteroids that did not undergo differentiation (or other significant alteration) preserve the best record of their formation. These primitive meteorites are called chondrites because they contain many chondrules. Chondrules are glassy inclusions, with a typical size $\sim 0.1 - 1$ mm. They provide evidence for high temperature melting events in the Solar nebula. The nature of these melting events is debated and beyond our scope (Connolly et al. 2006). Calcium Aluminum Inclusions (CAIs) are also present in primitive meteorites. CAIs experienced even more extreme heating than chondrules.

With ages up to 4567.11 ± 0.16 Myr (Russell et al. 2006), CAIs are the oldest known objects in the Solar System. This age is consistent with current results for the main sequence age of the Sun (Bonanno et al. 2002). The absolute ages of CAIs are measured by lead-lead dating, which makes use of half-lives, $t_{1/2}$, of uranium isotopes that are conveniently long. The decay chain of $^{235}\mathrm{U} \rightarrow ^{207}\mathrm{Pb}$ has $t_{1/2} = 0.704$ Gyr, while $^{238}\mathrm{U} \rightarrow ^{206}\mathrm{Pb}$ has $t_{1/2} = 4.47$ Gyr.

Radioisotopes with short half-lives yield accurate relative ages of meteorite components. These isotopes are "extinct;" they have decayed completely to daughter products whose abundances relative to other isotopes result in an age. The extinct isotope ^{26}Al decays to ^{26}Mg in $t_{1/2} = 0.73$ Myr. The abundance of ^{26}Mg relative to ^{27}Al and to ^{24}Mg yields an age for the sample. Aside from its use as a chronometer, ^{26}Al is a powerful heat source in young protoplanets.

Both absolute (lead-lead) and relative (^{26}Al) ages support a planet formation timescale of a few Myr. Most CAIs formed in a narrow window of $1 - 3 \times 10^5$ yr; chondrule formation persisted for ~ 4 Myr or longer. Russell et al. (2006) discuss systematic uncertainties. Here, we emphasize the remarkable agreement of the few Myr formation time derived from primitive meteorite analyses and protoplanetary disk observations (§2.2).

The assembly of terrestrial planets from planetesimals requires tens of Myr. Isotopic analysis of differentiated Solar System bodies (including Earth, Mars and meteorites) probe this longer timescale. The decay of radioactive hafnium into tungsten, $^{182}\mathrm{Hf} \rightarrow ^{182}$ W with $t_{1/2} = 9.8$ Myr, dates core-mantle segregation. Tungsten is a siderophile (prefers associating with metals) while hafnium is a lithophile (prefers the rocky mantle); thus, Hf-W isotope ratios are the primary tool to date differentiation (Chapter by Barlow). Studies of Hf-W systematics indicate that asteroid accretion continued for ~ 10 Myr, Mars' core formed within 20 Myr, and the Earth's core grew over 30–100 Myr (Kleine et al. 2009). Astronomical observations of debris disks (§2.2) and dynamical studies of terrestrial planet accretion (§5) support these longer timescales.

2.1.3. Water

After hydrogen, water is the most abundant molecule in disks (e.g., Najita et al. 2007). Inside the snow line, water exists in the gaseous phase, though it dissociates at $T \gtrsim 2500$ K. As water vapor interior to the ice line diffuses past the snow line, it condenses into icy grains. The snow line thus acts as a cold trap, where the enhanced mass in water ice (eq. [2-4]), should accelerate the growth of planetesimals and perhaps gas giant planets (Stevenson & Lunine 1988).

Water is abundant throughout the Solar System (e.g., Rivkin et al. 2002; Jewitt et al. 2007, and references therein). Outside of the Earth, water appears in spectra of comets, Kuiper belt objects, and satellites of giant planets (including the Moon) and bound within minerals on Mars, Europa, and some asteroids. Because they can be analyzed in great detail, meteorites from asteroids provide a wealth of information on water in the inner Solar System. Many meteorites show evidence for aqueous alteration prior to falling onto the Earth. Most groups of carbonaceous chondrites and some type-3 ordinary chondrites contain hydrated minerals, suggesting association with liquid water. Despite some evidence that grains might react with water prior to their incorporation into larger solids, most analyses of the mineralogy suggest hydration on scales of mm to cm within chondrites and other meteorites (Zolensky & McSween 1988).

The water content of Solar System bodies helps trace the evolution of the snow line (Kennedy & Kenyon 2008). Hydration within meteorite samples demonstrates that the snow line was at least as close as 2.5–3 AU during the formation of the asteroids (Rivkin et al. 2002). Radiometric analyses suggest hydration dates from 5–10 Myr after the formation of the Sun, close to and perhaps slightly after the formation of chondrules. Ice on the Earth and on Mars suggests the possibility that the snow line might have been as close as 1 AU to the proto-Sun, a real possibility for passively irradiated disks (§3.4). Within the terrestrial zone, the rise in water abundance from Venus (fairly dry) to Earth (wetter) to Mars and the asteroids (wetter still) points to processes that either distributed water throughout the inner Solar System (with a preference for regions near the snow line) or inhibited accretion of water (either vapor or ice) from the local environment. Abundance analyses, including D/H and noble gases, help to probe the (still imperfectly known) history of water in the inner Solar System.

2.2. Disks Surrounding the Youngest Stars

Observations of young stars provide additional constraints on the early evolution of planetary systems. In nearby star-forming regions (Orion, Taurus, etc), nearly every star with an age of 1 Myr or less has an optically thick circumstellar disk (Williams & Cieza 2011). The disk frequency seems independent of stellar mass. The data suggest the disks are geometrically thin, with a vertical extent of roughly 10% to 20% of their outer radius. They are composed of molecular gas and dust grains with sizes ranging from a few microns up to several mm. Around solar-type stars, young disks have typical luminosities of order $L_\odot$ and radii of order 100 AU.

Estimating disk masses is challenging. Aside from a few transitions possible only in warm material near the central star, H_2 is undetectable. The next most abundant molecule, CO, is optically thick and provides a crude lower limit to the total mass. Current estimates rely on a conversion from the dust emission at mm wavelengths to a dust mass and then to a mass in gas. These estimates are highly uncertain due to ignorance of dust-to-gas ratios and grain size

distributions. The typical assumptions give disk masses ~ 0.01 $M_\odot$, a factor of 2–4 smaller than the MMSN. The dispersion for ensembles of a few hundred systems is roughly an order of magnitude (Andrews & Williams 2005; Williams & Cieza 2011). The size of the typical disk is similar to the semimajor axes of orbits in the Kuiper belt.

Current data demonstrate that more massive young stars have more massive disks. Recent observational programs concentrate on whether the ratio of disk mass to stellar mass is roughly constant or increases with stellar mass. Despite the larger scatter in this ratio at every stellar mass, the relation is probably linear (Williams & Cieza 2011).

High resolution radio observations reveal interesting limits on the distributions of surface density and temperature within the brightest and most massive disks around nearby stars. Although disks with a broad range of surface density gradients are observed ($\Sigma \propto R^{-n}$ with $n \approx -0.6$ to 1.5), most observations indicate a typical $n \approx 0.5$–1.5 (Andrews & Williams 2005; Isella et al. 2009; Williams & Cieza 2011). Thus, the surface density gradient in the MMSN is steeper than the average protostellar disk but within the range observed in disks around other young stars.

The evolution of protostellar disks sets severe limits on the timescale for planet formation. Optical and ultraviolet spectra of young stars show that material from the disk flows onto the central star. The rate of this flow, the mass accretion rate, drops from well in excess of 10^{-8} $M_\odot$ yr^{-1} at 1 Myr to much less than 10^{-11} $M_\odot$ yr^{-1} at 10 Myr (Williams & Cieza 2011). Declining mass accretion rates imply much less gas near the young star. At the same time, the fraction of young stars with opaque dusty disks declines from nearly 100% to less than 1%. Fewer dusty disks implies the solid material has been incorporated into large (km-sized or larger) objects, accreted by the central star, or driven out of the system by radiation pressure or a stellar wind. Direct constraints on the amount of gas left in 10 Myr old systems without opaque disks are limited to a few systems.

Among older stars with ages of 3–10 Myr, many disks have substantial mass beyond 30–50 AU but have inner holes apparently devoid of much gas or dust. The frequency of these "transition" disks suggests the evolution opaque disk $\rightarrow$ opaque disk with inner hole $\rightarrow$ no opaque disk takes from 0.1–0.3 Myr up to 1–2 Myr (Currie & Sicilia-Aguilar 2011; Espaillat et al. 2012).

Once the opaque disk disappears, many pre-main and main sequence stars remain surrounded by 1–10 μm dust grains (Wyatt 2008). This material lies in a belt with radial extent $\delta R \approx 0.1-0.5R$ and vertical height $\delta z \approx 0.05-0.1R$, with $R \approx$ 1–100 AU. Infrared spectroscopy suggests the grains have compositions similar to material in the comets and the dust (Zodiacal Light) of the Solar System. The total mass, a few lunar masses, exceeds the mass of dust in the inner solar system by factors of 100–1000. These properties are independent of stellar metallicity and many other properties of the central star. However, the frequency of and the amount of dusty material in these dusty disks peaks for stars with ages of 10–20 Myr and then declines approximately inversely with time (Currie et al. 2008).

These disks place interesting limits on the reservoir of large objects around stars with ages of 10–20 Myr. Among several possible grain removal mechanisms, the most likely are radiation processes and collisions (Backman & Paresce 1993). Grains orbiting the star feel a headwind from the incoming radiation from the central star, which causes the grain to spiral into the star (Burns et al. 1979). If the grains have a mass density $\rho_\bullet$, the orbital decay time for this Poynting-Robertson

drag is

$$t_{pr} = \left(\frac{4\pi r \rho_\bullet}{3}\right)\left(\frac{c^2 R^2}{\mathrm{L}_\star}\right) = 710\ \rho_\bullet\ \left(\frac{r}{\mu\mathrm{m}}\right)\left(\frac{R}{\mathrm{AU}}\right)^2\ \left(\frac{\mathrm{L}_\star}{\mathrm{L}_\odot}\right)^{-1}\ \mathrm{yr}\ . \tag{2-8}$$

The decay time, $t_{pr} \sim 1$ Myr, is much shorter than the 100 Myr to 10 Gyr main sequence lifetime of the central star. The large frequency of dusty disks among 50–500 Myr (1–10 Gyr) old A-type (G-type) stars suggests the grains are continually replenished over the main sequence lifetime. By analogy with the Solar System, where trails of dust result from collisions of asteroids (Nesvorný et al. 2003), high velocity collisions among large (but undetectable) objects can replenish the dust. Adopting typical sizes for asteroids, $\sim$ 1–10 km, a reservoir containing ~ 10 $\mathrm{M}_\oplus$ of material can explain the amount of dust around young stars and the time evolution of the dust emission among older stars. Because this mass is between the initial mass of solids in protostellar disks ($\sim$ 100–1000 $\mathrm{M}_\oplus$) and the dust mass in the Solar System ($\lesssim 10^{-4}$ $\mathrm{M}_\oplus$), these systems are often called "debris disks" (Wyatt 2008, also Chapter by Moro-Martin).

2.3. The Exoplanet Revolution

The current pace of exoplanet discovery is extraordinarily rapid. Here, we highlight the main insights exoplanets bring to theories of planet formation.

Within the discovery space accessible with current techniques, exoplanets fill nearly all available phase space (e.g., Cumming et al. 2008; Gould et al. 2010; Howard et al. 2011; Johnson et al. 2011, and references therein). Among $\sim$ 10% to 30% of middle-age solar-type stars, exoplanets lie within a few stellar radii from the central star out to several AU. Because there are many multiplanet systems, the sample of short period planets implies more planets than stars (Youdin 2011b). Though detection becomes more difficult, the frequency of exoplanets seems to grow with increasing distance from the parent star. The orbits have a broad range of eccentricities, with a peak at $e \sim 0.2$. Planet masses range from a rough upper limit at 10–20 M_J to a few Earth masses. Around stars with the same mass, lower mass planets are more frequent than higher mass planets. More massive stars tend to have more massive planets.

There is some evidence that exoplanets are more likely around metal-rich stars (Gonzalez 1997; Johnson et al. 2010). With the large samples available, this "planet-metallicity correlation" is now unambiguous for gas giants with masses ranging from the mass of Saturn up to ~ 10 M_J. Among lower mass planets, small samples currently prevent identifying a clear correlation. Larger samples with the *Kepler* satellite will yield a better test of the planet-metallicity correlation as a function of planet mass.

The origin of any planet-metallicity correlation establishes some constraints on formation theories. If the initial metallicity of the disk is identical to the current metallicity of the star, then gas giants – and perhaps other planets – form more frequently in more metal-rich disks. However, planets could pollute the stellar atmosphere after the rest of the gaseous disk disperses, raising the metallicity of the star above the initial metallicity of the disk. In this case enhanced metallicity would be a result not a cause of planet formation. Current data contradicts the pollution hypothesis (Fischer & Valenti 2005; Pasquini et al. 2007), but more study of the diverse exoplanet population is warranted.

To quantify the planet-metallicity correlation, Johnson et al. (2010) fit the frequency, f, of

giant planets as a joint power-law in stellar mass, $M_\star$, and metallicity, $Z_{\rm Fe} \propto \log_{10}([{\rm Fe/H}])$,

$$f \propto M_\star^\alpha Z_{\rm Fe}^\beta \ . \tag{2-9}$$

For giant planets in the California Planet Survey, $\alpha = 1.0 \pm 0.2$ and $\beta = 1.2 \pm 0.2$. Ignoring the dependence with stellar mass ($\alpha \equiv 0$) introduces a bias, but yields a stronger relation with metallicity, ($\beta = 1.7 \pm 0.3$). For more massive stars with $M_\star > 1.4 M_\odot$, $\alpha = 1.5 \pm 0.4$ and $\beta = 0.73 \pm 0.35$. Thus, the formation of giant planets around more massive stars is more sensitive to stellar mass and less sensitive to metallicity than for lower mass stars.

With exoplanet samples growing so rapidly, new analyses will change at least some of these conclusions. The most firm conclusions – that exoplanetary systems are common and have nearly as much diversity as possible – provides a good counterpoint to the wealth of detail available from *in situ* analyses of the Solar System.

3. DISK PROPERTIES AND EVOLUTION

Stars form within collapsing clouds of gas and dust. When a cloud collapses, most infalling material has too much angular momentum to fall directly onto the nascent protostar. This gas forms a rotationally supported circumstellar disk (Cassen & Moosman 1981; Terebey et al. 1984). If the angular momentum in the disk is transported radially outward, gas can accrete onto the central star. Although jets launched near the protostar (Shu et al. 2000) or from the disk (Pudritz et al. 2007) or both can remove significant angular momentum from the disk, most analyses concentrate on how angular momentum flows through the disk.

At early times, the disk mass $M_{\rm disk}$ is similar to the stellar mass $M_\star$. For a circumstellar disk with surface density Σ and radial flow velocity v_R, the rate material flows through the disk as a function of radial coordinate R is

$$\dot{M} = -2\pi R v_R \Sigma \ . \tag{3-1}$$

Positive $\dot{M}$ corresponds to gas flowing towards, and eventually draining onto, the central star. If the mass infall rate from the surrounding molecular cloud $\dot{M}_i$ exceeds $\dot{M}$, the disk mass grows. If $M_{\rm disk}$ exceeds $\sim 0.3 M_\star$, gravitational instabilities within the disk can produce a binary companion (Adams et al. 1989; Kratter et al. 2010a). Smaller instabilities may form brown dwarfs or giant planets (§5.3). At late times, several processes – including the clearing action of protostellar jets and winds (Shu et al. 1987) – stop infall. Without a source of new material, the disk mass gradually declines with time.

In general, all of the physical variables characterizing the cloud and the disk change with radius and time. However, $\dot{M}_i$, $\dot{M}$, and Σ often change slowly enough that it is useful to construct steady disk models with a constant $\dot{M}$ throughout the disk. Here, we develop the basic equations governing the evolution of the disk and use steady disks to show the general features of all circumstellar disks.

An evolving gaseous disk sets the physical conditions in which small particles grow into planets. Physical conditions within the disk limit how planetesimals can form (§4) and how solid planets grow out of planetesimals (§5.1.5). Once solid planets form, the gaseous disk provides the mass reservoir for giant planet atmospheres (§5.2) and drives planet migration (see chapter by Morbidelli).

3.1. Basic Disk Dynamics

To introduce basic concepts in disk dynamics we describe orbital motion in a gas disk and the radial flow induced by viscosity. The orbital velocity of the gas v_ϕ, is set by the balance of radial forces – centrifugal, pressure and gravitational[2] – as

$$-\frac{v_\phi^2}{R} + \rho^{-1}\frac{\partial P}{\partial R} + \frac{GM_\star}{R^2} = 0 \ , \tag{3-2}$$

where ρ is the gas density and P is the gas pressure. Away from the immediate vicinity of protoplanets, gravity from the central star typically dominates. Even a self-gravitating thin disk has $M_{\rm disk} \ll M_\star$. For $P = P_0(R/R_0)^{-n}$ (the index n need only be locally valid), the orbital motion is

$$v_\phi = v_K \left(1 - \frac{nc_s^2}{\gamma v_K^2}\right)^{1/2} \ , \tag{3-3}$$

in terms of the Kepler velocity, $v_K = \sqrt{GM_\star/R}$, and the sound speed, $c_s = \sqrt{\gamma P/\rho}$, with γ the adiabatic index. Plausible disk models have an outwardly decreasing pressure ($n > 0$) almost everywhere. Thus pressure support typically gives sub-Keplerian rotation, but the correction is quite small, $v_\phi - v_K \sim -10^{-3} v_K$. It is often safe to ignore the pressure correction to orbital motions, but not when studying the motion of solids relative to gas (Weidenschilling 1977a; Youdin 2010, §4.1.1).

Accretion disks also have radial inflow, which is constrained by the laws of mass, angular momentum and energy conservation. Indeed accretion disks can be considered as machines that radiate energy as they transport mass inwards and angular momentum outwards. The viscous disk model offers the simplest means to understand how a disk manages this feat. Consider a thin ring with two adjacent annuli at distances R_1 and R_2 from a star with mass $M_\star$ (Fig. 1). Material orbits the star with angular velocities, $\Omega_1 = \sqrt{GM_\star/R_1^3}$ and $\Omega_2 = \sqrt{GM_\star/R_2^3}$. If the gas has viscosity, the differential rotation, $\Omega_1 - \Omega_2 < 0$ for $R_2 > R_1$, produces a frictional (shear) force that attempts to equalize the two angular velocities. The resulting torques produce an outward flow of angular momentum. By moving a small amount of disk material onto distant, high-angular momentum orbits, large amount of mass can fall inwards to low angular momentum orbits. Mass accretion is biased towards inflow because specific (i.e. per unit mass) angular momentum can increase to very large values, but cannot fall below zero. The heat generated by viscous dissipation affects the disk temperature and the predicted spectra as described in §3.3.

For a disk with surface density Σ and viscosity ν, mass continuity and conservation of angular momentum lead to a non-linear diffusion equation for Σ (e.g., Lynden-Bell & Pringle 1974; Pringle 1981),

$$\frac{\partial \Sigma}{\partial t} = 3R^{-1}\ \frac{\partial}{\partial R}\ \left(R^{1/2}\ \frac{\partial}{\partial R}\ \{\nu \Sigma R^{1/2}\}\right)\ +\ \dot{\Sigma}_{ext}. \tag{3-4}$$

The first term on the right hand side corresponds to viscous evolution; the second is a source term which is positive for infall from the cloud ($\dot{\Sigma_{\rm ext}} = \dot{\Sigma}_i$) and negative for mass loss due to photoevaporation, disk winds, or accretion onto giant planets. Consider a simple model with $\nu =$

[2]The radial speeds associated with accretion produce negligible advective accelerations, $Dv_R/Dt \sim v_R^2/R$.

constant, $\dot{\Sigma}_{\rm ext} = 0$, and $\Sigma(R, t = 0) = m\delta(R - R_0)/2\pi R_0$. i.e. the initial mass m is in a narrow ring at radius R_0. The time evolution of the surface density is

$$\Sigma(x, \tau) = \frac{m}{\pi R_0^2}\, \tau^{-1}\, x^{-1/4}\, e^{-(1+x^2)/\tau}\, I_{1/4}(2x/\tau)\ , \tag{3-5}$$

where the scaled distance and time are $x = R/R_0$ and $\tau = t/t_0 = 12\nu t/R_0^2$, and $I_{1/4}$ is the modified Bessel function. Fig. 2 shows how this viscous solution asymptotically transports all of the mass to $R = 0$ and all of the angular momentum to infinity. This evolution occurs on the viscous timescale τ.

We now consider the evolution of disks with a more general viscosity law, $\nu = \nu_0(R/R_0)^\beta$. With a constant powerlaw β, exact similarity solutions to eq. (3-4) exist (Lynden-Bell & Pringle 1974). To develop intuition, we instead physically derive the approximate solution. After several viscous timescales have passed, the disk "forgets" the initial conditions (as seen in Fig. 2). Conservation of angular momentum alone (without applying mass conservation needed to derive eq. [3-4]) gives

$$\frac{\partial \Sigma}{\partial t} = \frac{1}{R^{3/2}} \frac{\partial}{\partial R} \left[\frac{\dot{M}\sqrt{R}}{2\pi} - \frac{3}{2}\nu\Sigma\sqrt{R} \right] . \tag{3-6}$$

The two terms in square brackets represent the advection of angular momentum and viscous torques. For a steady disk with $\partial\Sigma/\partial t = 0$, the term in square brackets must equal a constant (independent of R). This constant represents the torque at the inner boundary, which can be neglected far from that boundary (as we show explicitly in eq. [3-17]). Thus angular momentum conservation gives

$$\Sigma \simeq \frac{\dot{M}}{3\pi\nu} \propto R^{-\beta}\ , \tag{3-7}$$

where the final proportionality assumes the powerlaw viscosity and constant $\dot{M}$. From eq. (3-1) the accretion speed follows as

$$v_R = -\frac{3\nu}{2R}\,. \tag{3-8}$$

To derive the evolution of disk mass (and $\dot{M}$) in this limit, we adopt R_0 as the outer edge of the disk. The outer radius changes on the local viscous timescale

$$R_0 \sim \sqrt{\nu t} \sim (\nu_0 t)^{1/(2-\beta)}\,. \tag{3-9}$$

To conserve angular momentum and energy, the disk expands, requiring $\beta < 2$. Conservation of angular momentum, $J \sim M_{\rm disk}\Omega(R_0)R_0^2$, drives the evolution of the disk mass as

$$M_{\rm disk} \sim \frac{J}{\sqrt{GM_\star}} (\nu_0 t)^{-1/(4-2\beta)}\,. \tag{3-10}$$

The accretion rate through the disk is

$$\dot{M} = \frac{dM_{\rm disk}}{dt} \propto t^{-(5-2\beta)/(4-2\beta)}\,. \tag{3-11}$$

This physical derivation emphasizes the role of conservation laws in setting the global viscous evolution of the disk. The results are consistent with similarity solutions derived using Green's functions (Lynden-Bell & Pringle 1974).

3.2. Transport Mechanisms and the α Disk Model

The source of a physical mechanism to drive disk accretion is a longstanding problem. The molecular viscosity, $\nu_{\rm mol} = c_{\rm s}\lambda$ — the product of sound speed, $c_{\rm s}$, and collisional mean free path, λ — is far too small. For the MMSN, $\lambda = \mu m_H c_s/\Omega\Sigma\sigma_{H_2} \approx 0.8R^{11/4}$ cm, where $\mu = 2.4$ is the mean molecular weight, m_H is the mass of a hydrogen atom, and σ_{H_2} is the collision cross-section for the dominant constituent of the gas, H_2. The resulting accretion timescale

$$t_{\rm acc,mol} = \frac{M_{\rm disk}}{\dot{M}} \sim \frac{R^2}{\nu_{\rm mol}} \sim 7 \times 10^{13} \left(\frac{R}{\rm AU}\right)^{-4/7} \ {\rm yr} \tag{3-12}$$

vastly exceeds the age of the universe. Viable mechanisms for angular momentum transport are sometimes identified as "anomalous" sources of viscosity. Because long range interactions are often important, the analogy between a transport mechanism and the local viscosity is inexact. For sufficiently small scale fluctuations, however, even self-gravitating disks are well approximated by the viscous prescription (Lodato & Rice 2004).

Anomalous viscosity is most often associated with turbulence in the disk. Because the size of turbulent eddies can greatly exceed λ, the effective turbulent viscosity can vastly exceed the molecular one, even for slow, subsonic turbulence. However, turbulence by itself does not explain accretion, velocity fluctuations must correlate for angular momentum to be transported outwards. Moreover it is difficult (if not impossible) for Keplerian shear to drive turbulence; the angular momentum gradient in disks is quite stable according to the Rayleigh criterion (Stone & Balbus 1996).

Over the past 50 years, theorists have considered a wide range of transport mechanisms: convective eddies, gravitational instabilities, internal shocks, magnetic stresses, orbiting planets, sound waves, spiral density waves, and tidal forces. Currently the "magneto-rotational instability" (MRI) is the leading candidate for a transport mechanism in low mass disks (Balbus & Hawley 1991; Papaloizou & Nelson 2003). In this mechanism, modest magnetic fields thread ionized material orbiting the central star. An outward (or inward) perturbation of fluid stretches and shears the magnetic fields. The resulting torque amplifies the original perturbation and, crucially, transports angular momentum outwards. Although this mechanism is attractive, the low ionization fraction of protostellar disks restricts the MRI to surface layers of the disk at many radii. Disks may then contain extensive "dead zones" (Gammie 1996), where levels of transport and turbulence are reduced. In massive protostellar disks, gravitational waves and gravitoturbulence are another likely source of angular momentum transport (Lin & Pringle 1987).

To sidestep fundamental uncertainties of transport mechanisms, it is convenient to adopt a simple viscosity model (Shakura & Sunyaev 1973; Lynden-Bell & Pringle 1974). Setting $\nu = \alpha c_s H$ – where $H = c_s/\Omega$ is the vertical scale height of the disk – leads to the popular "α-disk" model. The dimensionless parameter $\alpha < 1$ (even $\ll 1$) since large values would lead to rapid shock dissipation and/or gravitational fragmentation. Similar to the mixing length parameterization of convection, α-disk models allow progress despite ignorance of the underlying dynamics. Detailed simulations typically quote measured transport rates in terms of effective α values.

This definition allows us to define the three important timescales in a viscous disk (e.g., Lynden-Bell & Pringle 1974; Pringle 1981). The shortest disk timescale is the dynamical (orbital)

timescale, $t_d \sim \Omega^{-1}$:

$$t_d \approx 0.17 \text{ yr } \left(\frac{M_\star}{\mathrm{M}_\odot}\right)^{-1/2} \left(\frac{R}{\mathrm{AU}}\right)^{3/2} . \tag{3-13}$$

The disk establishes hydrostatic equilibrium in the vertical direction on the same timescale $t_v \approx H/c_s \approx \Omega^{-1} \approx t_d$.

The disk cooling time, $t_c \approx U/D$ is the ratio of the thermal energy content (per unit area), $U = C_v \Sigma T$, to the energy generation or dissipation rate, D. For a viscous disk $D = 9\nu\Sigma\Omega^2/4$ (Pringle 1981); C_v is the specific heat at constant volume. With $C_v T = (\gamma - 1)^{-1} P/\rho$ for an ideal gas, the cooling time is

$$t_c \approx \frac{4}{9\gamma(\gamma-1)} \; \alpha^{-1} \; \Omega^{-1} . \tag{3-14}$$

In this classical result, the thermal timescale depends only on the local dynamical timescale, the dimensionless viscosity (α), and the equation of state (γ). For a molecular gas, $\gamma \approx 7/5$. The cooling time is a factor of roughly α^{-1} larger than the dynamical time:

$$t_c \approx 0.08 \text{ yr } \alpha^{-1} \left(\frac{M_\star}{\mathrm{M}_\odot}\right)^{-1/2} \left(\frac{R}{\mathrm{AU}}\right)^{3/2} . \tag{3-15}$$

The viscous timescale – $t_\nu = R^2/3\nu$ – measures the rate matter diffuses through the disk. Using our expressions for the sound speed and the viscosity, $t_\nu \approx (\alpha\Omega)^{-1}(R/H)^2$. Thus, the viscous timescale is

$$t_\nu \gtrsim 0.17 \text{ yr } \alpha^{-1} \left(\frac{R}{H}\right)^2 \left(\frac{M_\star}{\mathrm{M}_\odot}\right)^{-1/2} \left(\frac{R}{\mathrm{AU}}\right)^{3/2} . \tag{3-16}$$

Typically the disk is thin, $H/R \approx 0.03$–0.1; thus, the viscous timescale is 100–1000 times longer than the cooling time.

The radial velocity in eq. (3-8) becomes $v_R \approx \alpha c_s H/R \approx 0.1\alpha(H/R)^2 v_\phi$. With $\alpha < 1$ and $H/R < 1$, v_R is much smaller than both the orbital velocity and the sound speed.

3.3. Viscously Heated Disks

As shown above, $t_\nu \gg t_c > t_d$ for $\alpha < 1$, so the thermal properties of the disk adjust rapidly to changes in the surface density distribution. This property is very useful in describing the thermal properties of many astrophysical disks, including active galactic nuclei, interacting binaries, and pre-main sequence stars (Pringle 1981). We now describe the basic energetics of accretion disks with constant $\dot{M}$

Since gas remains on Keplerian orbits as it accretes, the specific energy release in falling from $R + dR$ to R is $GM_\star dR/(2R^2)$, since half the potential energy goes into the increase in kinetic energy. The energy release per unit area for a disk accreting at $\dot{M}$ is $F_K(R) = G\dot{M}M_\star/(4\pi R^3)$. This result is completely independent of how the energy was released.

The energy released by viscous dissipation does not simply match the local change in kinetic energy. To fully describe the energetics of steady viscous disks, we must keep the integration

constant when integrating eq. (3-6) over radius to get,

$$\nu\Sigma = \frac{\dot{M}}{3\pi}\left(1 - \sqrt{\frac{R_J}{R}}\right) \ . \tag{3-17}$$

The integration constant, R_J, represents the torque $\dot{J}$ exerted at the inner boundary, R_{in} as $\dot{J} = \dot{M}\sqrt{GM_\star}(\sqrt{R_{in}} - \sqrt{R_J})$. The standard choice $R_J = R_{in}$ is a zero torque boundary condition. Negative torques are not allowed for steady disks, as $R_J > R_{in}$ would require $\nu\Sigma < 0$. For $R_J = 0$, the maximum torque $\dot{J}_{max} = \dot{M}\sqrt{GM_\star R_{in}}$ matches the flow of angular momentum past the inner boundary.

The laws of fluid dynamics in cylindrical coordinates (Shu 1992) give the viscous dissipation as[3]

$$D(R) = \nu\Sigma\left(R\frac{\partial\Omega}{\partial R}\right)^2 = \frac{3GM_\star\dot{M}}{4\pi R^3}\left(1 - \sqrt{\frac{R_J}{R}}\right) \ . \tag{3-18}$$

As advertised, this expression does not simply match the local release of Keplerian orbital energy; far from the boundary ($R \gg R_J$), $D(R) \approx 3F_K(R)$. Viscous disks transport energy (in addition to angular momentum) from the inner disk to the outer disk. Nevertheless, the rapid falloff with R means that most energy is dissipated close to the disk's inner edge.

Now consider the total energy release from large R to the inner boundary. The Keplerian energy release is just $L_K = GM_\star\dot{M}/(2R_{in})$. The total viscous luminosity is

$$L_d = 2\pi\int_{R_{in}}^{\infty} D(R)2\pi R dR = \frac{3}{2}\frac{GM_\star\dot{M}}{R_{in}}\left(1 - \frac{2}{3}\sqrt{\frac{R_J}{R_{in}}}\right) \tag{3-19}$$

For the zero torque boundary condition ($R_J = R_{in}$) the luminosity simply matches the release of Keplerian energy. However the disk's luminosity increases due to work done by torques at the inner edge, up to $L_d = 3L_K$ for $R_J = 0$. For typical parameters in protostellar disks

$$L_d = \frac{f_d GM_\star\dot{M}}{2R_{in}} \approx 0.16 f_d L_\odot \left(\frac{\dot{M}}{10^{-8}\ \mathrm{M_\odot\ yr^{-1}}}\right)\ \left(\frac{M_\star}{M_\odot}\right)\ \left(\frac{R_{in}}{\mathrm{R_\odot}}\right)^{-1} \ , \tag{3-20}$$

where f_d ranges from 1 (no torque) to 3 (maximum torque).

The maximum disk luminosity occurs for a disk that extends to the stellar stellar surface, $R_{in} = R_\star$. The total accretion luminosity,

$$L_{acc} = \frac{f_\star GM_\star\dot{M}}{2R_\star} \, , \tag{3-21}$$

with $1 \lesssim f_\star \lesssim 2$, includes all the energy loss needed to come to rest on the rotating stellar surface. For a star rotating at breakup $f_\star \approx 1$. For a slowly rotating star the damping of the orbital kinetic energy gives twice the energy release $f_\star \approx 2$. Any difference $L_{acc} - L_d \geq 0$ is emitted at

[3]Note that eq. 3.10 in Pringle (1981) has a factor of two typo in the intermediate result (involving ν) but reaches the correct final result (in terms of $\dot{M}$).

the stellar surface. This difference must be positive (accretion should not cool the star), further constraining f_d. As a consistency check, note that a disk with an inner boundary at the surface of a star, $R_{in} = R_\star$, that rotates at breakup, must satisfy the zero torque boundary condition to avoid $L_{acc} < L_d$.

In many cases, the accreting star has a magnetosphere that truncates the disk at $R_{in} > R_\star$ (e.g., Ghosh & Lamb 1979). Material then flows onto the star along magnetic field lines, collimated onto hot spots, which are hot because the accretion energy is emitted from a small fraction of the stellar photosphere. In most young stars, $R_{in} \approx$ 3–5 $R_\star$ (e.g., Kenyon et al. 1996; Bouvier et al. 2007). Thus the hot spot luminosity

$$L_{hot} = L_{acc} - L_d = L_{acc} \left(1 - \frac{f_d R_\star}{f_\star R_{in}} \right) \tag{3-22}$$

can easily reach 60-80% of the total accretion luminosity. For star that corotates with the disk's inner edge, $f_d \approx f_\star \approx 1$ is expected (Shu et al. 1994).

To calculate the temperature structure of viscously heated disks, note that the upper and lower halves of the disk each radiate half of $D(R)$. If the vertical optical depth $\tau > 1$, the disk photosphere then has effective temperature T_e,

$$\sigma_{\rm SB} T_e^4 = \frac{3GM_\star \dot{M}}{8\pi R^3} \left(1 - \sqrt{\frac{R_J}{R}} \right) \ . \tag{3-23}$$

Though T_e is calculated as if the disk radiates as a blackbody, the disk's atmosphere will radiate as a stellar atmosphere with spectral lines, especially when $T_e \gtrsim$ 1000–1500 K. The effective temperature declines as $T_e \propto R^{-3/4}$ for $R \gtrsim$ a few $R_\star$:

$$T_e = 85 \text{ K} \left(\frac{\dot{M}}{10^{-8} \text{ M}_\odot \text{ yr}^{-1}} \right)^{1/4} \left(\frac{M_\star}{M_\odot} \right)^{1/4} \left(\frac{R}{\text{AU}} \right)^{-3/4} (1 - \sqrt{R_J/R}) \ . \tag{3-24}$$

In a simple, grey-atmosphere approach, the midplane temperature T_d is a factor of $\tau^{1/4}$ larger than T_e and is used to derive the scale height H, the viscosity ν, and other physical variables. More rigorous approaches calculate T_e and T_d using a self-consistent prescription for the opacity throughout the disk.

The temperature distribution in eq. (3-23) allows us to derive the surface density of an α disk. Assuming the midplane temperature scales like the effective temperature ($T_d \approx T_e \propto R^{-3/4}$), $\nu \propto c_s^2 \Omega^{-1} \propto r^{3/4}$ for the α prescription. Then eq. (3-7) gives

$$\Sigma(R) = \Sigma_0 \left(\frac{R}{\text{AU}} \right)^{-3/4} \tag{3-25}$$

where Σ_0, the surface density at 1 AU, depends on the mass accretion rate. Solving for the midplane temperature with realistic opacities yields $\Sigma \propto R^{-\beta}$ with $\beta \approx$ 0.6–1 (e.g., Stepinski 1998; Chambers 2009).

3.4. Steady Irradiated Disks

Although viscous dissipation drives the overall evolution, radiation from the central star also heats the disk (Friedjung 1985; Adams & Shu 1986; Kenyon & Hartmann 1987). If the disk is an infinite, but very thin, sheet, it absorbs roughly 25% of the light radiated by the central star. For a 1 $L_\odot$ central star and disk accretion rates $\dot{M} \lesssim 10^{-8}$ $M_\odot$ yr^{-1}, emission from irradiation exceeds emission from viscous dissipation (eq. [3-20]). If the disk re-radiates this energy at the local blackbody temperature, the radial temperature gradient of a flat, irradiated disk follows the gradient for a viscous disk, $T_d \propto R^{-3/4}$ (Friedjung 1985; Adams & Shu 1986).

Disks with vertical scale height H absorb and re-radiate even more starlight (Kenyon & Hartmann 1987). Chiang & Goldreich (1997) derive a general formalism for H and T_d in a "passive" disk with negligible $\dot{M}$. Defining θ as the grazing angle that starlight hits the disk, the temperature of a disk that emits as a blackbody is

$$T_d \approx \left(\frac{\theta}{2}\right)^{1/4} \left(\frac{R_\star}{R}\right)^{1/2} T_\star \; , \tag{3-26}$$

where $T_\star$ is the stellar temperature. The grazing angle is

$$\theta \approx 0.4\frac{R_\star}{R} + R\frac{d}{dR}\left(\frac{h}{R}\right) \; , \tag{3-27}$$

where h is the height of the photosphere above the disk midplane. For a blackbody disk in vertical hydrostatic equilibrium, the grazing angle is the sum of a nearly flat component close to the star and a flared component far from the star:

$$\theta \approx 0.005 \left(\frac{R}{\rm AU}\right)^{-1} + 0.05 \left(\frac{R}{\rm AU}\right)^{2/7} \; . \tag{3-28}$$

The disk temperature beyond a few tenths of an AU is then

$$T_d \approx 155 \text{ K } \left(\frac{R}{\rm AU}\right)^{-3/7} \left(\frac{R_\star}{R_\odot}\right)^{1/2} \left(\frac{T_\star}{T_\odot}\right) \; . \tag{3-29}$$

For $\dot{M} \approx 10^{-8}$ $M_\odot$ yr^{-1}, the irradiated disk is roughly twice as hot as a viscous accretion disk.

This temperature relation leads to a steeper surface density gradient in α disks. With $\nu \propto c_s^2 \Omega^{-1}$ and $c_s^2 \propto T_d$, $\nu \propto r^{15/14}$. Using this viscosity in eq. (3-7),

$$\Sigma(R) = \Sigma_{0,irr} \left(\frac{R}{\rm AU}\right)^{-15/14} \; , \tag{3-30}$$

where

$$\Sigma_{0,irr} = \frac{2 \text{ g cm}^{-2}}{\alpha} \left(\frac{\dot{M}}{10^{-8} \text{ } M_\odot \text{ yr}^{-1}}\right) \; . \tag{3-31}$$

The surface density gradient for an irradiated disk is steeper than the gradient for a viscous disk and is reasonably close to the gradient for the MMSN.

For identical α, hotter irradiated disks have larger viscosity and smaller surface density than cooler viscous disks. Integrating eq. (3-30) over radius, the mass of an irradiated disk is

$$M_d \approx \left(\frac{10^{-4} M_\odot}{\alpha}\right) \left(\frac{\dot{M}}{10^{-8}\ M_\odot\ \mathrm{yr}^{-1}}\right) \left(\frac{R_d}{100\ \mathrm{AU}}\right)^{15/14} . \tag{3-32}$$

When $\alpha \approx 10^{-3} - 10^{-2}$, this estimate is close to the observed masses of protostellar disks around young stars.

3.5. Time Dependence

Deriving more robust estimates of disk evolution requires a direct solution of eq. (3-4). This exercise requires a model for the viscosity and a prescription for the thermodynamics and opacity of disk material. Analytic approaches assume a constant mass accretion rate through the disk. If α and τ are simple functions of the local variables Σ and T, then the diffusion equation can be solved exactly for $\Sigma(t)$, $\dot{M}(t)$, and other disk properties (Stepinski 1998; Chambers 2009). Numerical approaches allow α and $\dot{M}$ to vary with radius. Some solutions consider iterative solutions to the temperature and vertical structure (e.g. Hueso & Guillot 2005); others solve for the vertical structure directly using techniques developed for the atmospheres of stars (e.g. Bell & Lin 1994; D'Alessio et al. 1998).

To compare these approaches, we consider a simple model for a viscous disk irradiated by a central star. We assume that the optical depth of cool disk material is dominated by dust grains with a constant opacity κ_0; warmer dust grains evaporate and have a smaller opacity:

$$\kappa = \begin{cases} \kappa_0\ , & T_d \le T_{evap} \\ \kappa_0 \left(\frac{T_d}{T_{evap}}\right)^n , & T_d > T_{evap} \end{cases} \tag{3-33}$$

For material with roughly solar metallicity, typical values are $\kappa_0 \approx 2$ cm^2/g, $T_{evap} \approx 1380$ K, and $n = -14$ (e.g., Chambers 2009). With this opacity, we derive a self-consistent disk temperature and scale height (as in Hueso & Guillot 2005) and solve for the time evolution of Σ using an explicit solution to the diffusion equation (as in Bath & Pringle 1982).

Fig. 3 compares analytic and numerical results for a disk with $\alpha = 10^{-2}$, initial mass $M_{d,0}$ = 0.04 M$_\odot$, and initial radius R_0 = 10 AU surrounding a star with M$_\star$ = 1 M$_\odot$. The numerical solution tracks the analytic model well. At early times, the surface density declines steeply in the inner disk ($\Sigma \propto R^{-1.2}$; where dust grains evaporate) and more slowly in the outer disk ($\Sigma \propto R^{-0.6}$; where viscous transport dominates). At late times, irradiation dominates the energy budget; the surface density then falls more steeply with radius, $\Sigma \propto R^{-1}$.

Other approaches lead to similar time evolution in the surface density. Early on, a massive disk is dominated by viscous heating. For these conditions, the simple analytic estimate of the surface density yields $\Sigma \propto R^{-n}$ with $n = 3/4$ (eq. [3-25]), close to results for the numerical solution ($n = 0.6$) and other analytic and numerical ($n = 0.6 - 1$) approaches (Bath & Pringle 1982; Lin & Pringle 1990; Stepinski 1998; Chambers 2009; Alexander & Armitage 2009). As the disk ages, it evolves from a viscous-dominated to an irradiation-dominated system. Thus, the exponent n in the surface density relation approaches the limit ($n = 15/14$) derived in eq. (3-30).

Fig. 4 compares the evolution of the disk mass and accretion rate at the inner edge of the disk. In both solutions, the disk mass declines by a factor of roughly two in 0.1 Myr, a factor of roughly four in 1 Myr, and a factor of roughly ten in 10 Myr. Over the same period, the mass accretion rate onto the central star declines by roughly four orders of magnitude.

3.6. Disk Instabilities and Fragmentation

In addition to evolution on the viscous timescale shown in Fig. 3, all disks vary their energy output on much shorter timescales. In compact binary systems, these fluctuations range from small, 10%–20%, amplitude flickering on the local dynamical time scale to large-scale eruptions, factors of 10–100, that can last for several times the local viscous time scale (Warner 1995). Although many pre-main sequence stars also display distinctive brightness variations (Joy 1945; Herbig 1962), the FU Ori variables provide the cleanest evidence for large-scale variations of the disk, rather than the environment or the central star (Hartmann & Kenyon 1996).

Theory suggests several types of instabilities in viscous disks (see Pringle 1981). In standard derivations of the structure of steady disks, radiative cooling balances heating from viscous stresses. However, radiative losses are set by local disk parameters; local parameters and an input accretion rate set viscous energy generation. Usually radiative losses can keep up with changes in disk structure; sometimes, radiation cannot balance viscous stresses, leading to a thermal instability. A limit cycle arises, where regions of the disk alternate between states where radiative losses exceed (and then fall below) the viscous energy input. This mechanism may produce FU Ori and other eruptions in the disks of pre-main sequence stars (Hartmann & Kenyon 1996).

Viscous instabilities occur when changes in the local surface density do not produce parallel increases in the local mass transfer rate. From eq. (3-7), $\dot{M} \propto \nu\Sigma$. In a steady disk, ν is fairly independent of Σ; thus, $\dot{M}$ changes in step with Σ. For the MRI viscosity mechanism, however, larger Σ leads to larger optical depths, less ionization, and smaller α. Thus, an MRI disk with growing (falling) surface density can produce a smaller (larger) viscosity, leading to an ever greater over- or under-density in the surface density.

Although thermal and viscous instabilities change the temperature and surface density throughout the disk, they evolve on timescales much longer than the local orbital period. Massive disks can evolve on shorter timescales. If the local gravity in a region with size λ overcomes rotational support ($G\Sigma \gtrsim \Omega^2\lambda$) and thermal support ($G\Sigma \gtrsim c_s^2/\lambda$), this region can (begin to) collapse (Safronov 1960; Toomre 1964; Goldreich & Lynden-Bell 1965; Paczynski 1978). Together these conditions require $c_s^2/(G\Sigma) \lesssim \lambda \lesssim G\Sigma/\Omega^2$. Collapse at any wavelength requires the disk satisfy the "Toomre instability criterion,"

$$Q \equiv \frac{c_s \Omega}{\pi G \Sigma} \lesssim 1 \ . \tag{3-34}$$

Setting the disk mass $M_d \approx \Sigma R^2$, a stable disk has

$$c_s \gtrsim \frac{M_d}{M_\star} \ v_\phi \ . \tag{3-35}$$

When the disk first forms, $M_d \approx M_\star$. Such "disks" cannot be thin because $H/R \sim c_s/v_\phi \gtrsim 1$.

In a viscous accretion disk, the stability criterion can be re-written in terms of the accretion rate (Gammie 2001). With $\dot{M} = 3\pi\nu\Sigma$ and $\nu = \alpha c_s^2 \Omega^{-1}$ an unstable disk has $\dot{M}_Q \gtrsim 3\alpha c_s^3/G$. To

evaluate the temperatures of unstable disks, we use $c_s = (\gamma kT/\mu m_H)^{1/2}$ and set $\gamma = 7/5$ and $\mu = 2.4$ for molecular gas:

$$\dot{M}_Q \gtrsim 2.4\ 10^{-4}\ \alpha T^{3/2}\ \mathrm{M}_\odot\ \mathrm{yr}^{-1}\ , \tag{3-36}$$

with T in Kelvins. For the observed accretion rates in very young stars, $\dot{M} \sim 10^{-7}$ $\mathrm{M}_\odot$ yr^{-1}, unstable disks have $\alpha T^{3/2} \lesssim 0.4$. If α is large (10^{-2}), only very cold disks are unstable (T $\sim$ 10–15 K); smaller α (e.g., 10^{-3}) allows instability in warmer disks (T $\sim$ 50–60 K).

4. FROM DUST TO PLANETESIMALS

The accumulation of dust grains into planetesimals — solids greater than a kilometer in size — is the first step in the formation of terrestrial planets and giant planet cores. Several observational and theoretical reasons suggest the formation of planetesimals is a separate step. Observationally, remnant planetesimals in the Solar System and in extrasolar debris disks shows that growth sometimes stalls before planets accumulate all planetesimals. Comets from the Oort cloud also suggest an intermediate stage between dust grains and planets (see Chapter by Moro-Martin).

Theoretically, the physical processes responsible for the growth of planetesimals differ from those relevant to the final stages of planet formation. As Section 5 describes, few-body gravitational encounters — both scattering and gravitationally focused collisions — establish the rates of growth for icy and terrestrial planets. By contrast, the sticking of dust grains involves electrostatic forces. During planetesimal formation, particle dynamics is qualitatively different. Drag forces exerted by the gas disk dominate the motions of small solids. Though not negligible, the drag exerted on km-sized or larger planetesimals is weaker than gravitational interactions (§5.2).

While planetesimal formation is a common occurrence in circumstellar disks, understanding how it happens has proved elusive. Observations of planetesimal formation in action are indirect. Particles beyond cm-sizes contribute negligibly to images and spectra of circumstellar disks. Primitive meteorites record the conditions during planetesimal formation, but the implications for formation mechanisms are difficult to interpret — we need a better instruction manual.

Especially beyond millimeter sizes, experiments show that particle collisions often result in bouncing or breaking instead of sticking (Blum & Wurm 2000; Zsom et al. 2010; Weidling et al. 2012). Inefficient growth by coagulation is further complicated by the rapid infall of centimeter to meter sized solids into the star. These difficulties — often termed the "meter-sized barrier" — are explained in more detail in §4.1.

Gravitational collapse is one way to overcome the growth barrier. The mutual gravitational attraction of a collection of small solids could lead to a runaway collapse into planetesimals — even when sticking is inefficient and radial drift is fast. While appealing, this path encounters theoretical difficulties when stirring by turbulent gas is included. Section 4.2 describes the current status of the gravitational collapse hypothesis.

Even when self-gravity is weak, aerodynamic effects can concentrate solids in the disk. Particles tend to seek high pressure regions in the disk. This tendency causes the inward drift mentioned above. Particles can also concentrate in localized pressure maxima. Predicting the sizes and lifetimes of pressure maxima is a difficult (and currently unsolved) problem of disk meteorology.

In addition to the passive response of solids to the gas disk, active particle concentration occurs when particles cause their own clumping by altering the flow of gas. Instabilities caused by gas

drag, notably the streaming instability, provide a clumping mechanism that is both powerful and amenable to study by direct numerical simulations. The strong clumping driven by the streaming instability is capable of triggering gravitational collapse into ~ 100 km planetesimals. Both passive and active particle concentration mechanisms are reviewed in §4.3.

Theories based on complex non-linear dynamics must be tested against, and refined by, observations. We discuss observational consequences of planetesimal formation models in §4.4. Unless stated otherwise, the numerical estimates in the section use the passively heated MMSN disk (§3). For more detailed reviews of planetesimal formation, see Chiang & Youdin (2010) and Youdin (2010). For a thorough review of collision experiments and their relevance to planetesimal formation, see Blum & Wurm (2008).

4.1. The "Meter-Size" Barrier

We discuss in more detail the two components of the "meter-size" barrier to planetesimal formation. The review of radial drift timescales in §4.1.1 also serves as an introduction to the dynamics of solids in a gas disk. The discussion of collisional growth and destruction in §4.1.2 couples dynamical models of collision speeds to the complex physics of contact mechanics.

4.1.1. Radial Drift and the Basics of Disk Aerodynamics

The aerodynamic migration of small solids imposes the most stringent timescale constraint on planet formation: ≈ 100 years. Aerodynamic radial drift arises because solids encounter a headwind as they orbit through the gas disk (eq. [3-3]). This headwind removes angular momentum from particle orbits, causing their inspiral. Infall speeds are fastest for solids near roughly meter sizes. The critical size is actually below a meter in standard disk models — especially in their outer regions. So the "meter-size" barrier is a slight misnomer, but it has a better ring than the "millimeter-to-tens-of-centimeters-size" barrier.

Radial pressure gradients in gas disks set the speed of the headwind. Plausible disk models are hotter and denser in the inner regions; on average, the radial pressure gradient is directed outwards. If the radial pressure gradient is directed inwards, a tailwind — and outward particle migration — results.

We express the headwind speed as the difference between the Keplerian velocity, $v_{\rm K} = \sqrt{GM_\star/R} = \Omega R$, and the orbital speed of the gas, $v_{{\rm g},\phi}$:

$$\eta v_{\rm K} \equiv v_{\rm K} - v_{{\rm g},\phi} \approx -\frac{\partial P/\partial \ln R}{2\rho_{\rm g} v_{\rm K}} \approx 25 \left(\frac{R}{\rm AU}\right)^{1/14} \ {\rm m\ s^{-1}}\,, \tag{4-1}$$

where P and $\rho_{\rm g}$ are the pressure and density of the gas, and $\eta \sim c_{\rm s}^2/v_{\rm K}^2 \sim (H/R)^2 \sim 10^{-3}$ is a dimensionless measure of pressure support. In disks hotter than our passive model, headwinds and drift speeds are faster.

To derive eq. (4-1), compute radial force balance assuming (correctly) that the radial pressure acceleration, $f_{P,R} = -\rho_{\rm g}^{-1}\partial P/\partial R$, is weak compared to the centrifugal acceleration. Equivalently we can reproduce eq. (4-1) by balancing the pressure and Coriolis forces, $f_{P,R} + f_{{\rm Cor},R} = 0$ with $f_{{\rm Cor},R} = -2\Omega\eta v_{\rm K}$.

Drag forces set the response of particle orbits to the gas headwind. We express the drag acceleration felt by a solid particle as

$$\boldsymbol{f}_{\rm drag} = -\Delta\boldsymbol{v}/t_{\rm s}\,, \tag{4-2}$$

where $\Delta\boldsymbol{v}$ is the particle velocity relative to the gas and $t_{\rm s}$ is the aerodynamic damping timescale for this relative particle motion.

The value of $t_{\rm s}$ depends on particle properties – such as the internal density, $\rho_\bullet$, and spherical radius, s — and on properties of the gas disk — $\rho_{\rm g}$ and $c_{\rm s}$ – as:

$$t_{\rm s} = \begin{cases} t_{\rm s}^{\rm Ep} \equiv \rho_\bullet s/(\rho_{\rm g} c_{\rm s}) & \text{if } s < 9\lambda/4 \quad (4\text{-}3a) \\ t_{\rm s}^{\rm Stokes} \equiv t_{\rm s}^{\rm Ep}\cdot 4s/(9\lambda) & \text{if } 9\lambda/4 < s < \lambda/({\rm 4Ma}) \quad (4\text{-}3b) \\ t_{\rm s}^{\rm int}\cdot (s/\lambda)^{3/5}\,{\rm Ma}^{-2/5}/4 & \text{if } \lambda/({\rm 4Ma}) < s < 200\lambda/{\rm Ma} \quad (4\text{-}3c) \\ t_{\rm s}^{\rm turb} \equiv t_{\rm s}^{\rm Ep}\cdot 6/{\rm Ma} & \text{if } s > 200\lambda/{\rm Ma} \quad (4\text{-}3d) \end{cases}$$

where ${\rm Ma} \equiv |\Delta\boldsymbol{v}|/c_{\rm s}$, $\lambda \propto 1/\rho_{\rm g}$ is the gas mean free path, and ${\rm Re} \equiv 4s{\rm Ma}/\lambda$ is the Reynolds number of the flow around the particle. The cases are written in order of increasing particle size: Epstein's Law of drag from molecular collisions, Stokes' Law for viscous drag when ${\rm Re} < 1$, an approximate intermediate Re case, and the drag from a fully developed turbulent wake for ${\rm Re} > 800$. The turbulent drag force is more relevant for fully formed planetesimals and is commonly expressed as

$$F_{\rm drag} = -m\frac{|\Delta\boldsymbol{v}|}{t_{\rm s}^{\rm turb}} = -\frac{C_D}{2}\pi s^2\rho_{\rm g}|\Delta\boldsymbol{v}|^2\,, \tag{4-4}$$

where the drag coefficient, $C_D \approx 0.44$ (Adachi et al. 1976; Weidenschilling 1977a).

The dynamical significance of drag forces is measured by comparing the stopping time and the orbital frequency, via the parameter

$$\tau_{\rm s} \equiv \Omega t_{\rm s}\,. \tag{4-5}$$

For $\tau_{\rm s} \ll 1$, particles are carried along with the gas; for $\tau_{\rm s} \gg 1$, gas drag is a small correction to Keplerian orbits. Fig. 5 plots $\tau_{\rm s}$ for a range of particle sizes in our passively heated MMSN. At least in the inner disk, objects near meter-sizes have $\tau_{\rm s} \approx 1$. In the outer disk, where gas densities are lower, smaller solids have the critical $\tau_{\rm s} = 1$. As we now show, $\tau_{\rm s} = 1$ solids have the fastest radial drift speeds.

To derive the particle drift caused by the gas headwind, we consider the equations of motion for a particle in cylindrical coordinates, r and ϕ,

$$\ddot{R} - R\dot{\phi}^2 = -v_{\rm K}^2/R - \dot{R}/t_{\rm s} \tag{4-6}$$

$$R\ddot{\phi} + 2\dot{R}\dot{\phi} = -(R\dot{\phi} - v_{{\rm g},\phi})/t_{\rm s}\,. \tag{4-7}$$

To find the steady drift solutions, we make several approximations that are valid when drag forces are strong. We neglect the radial inertial acceleration, $\ddot{R}$, and express the azimuthal motion as a small deviation from the Keplerian frequency, $\dot{\phi} = \Omega + \delta v_\phi/R$ where $|\delta v_\phi| \ll \Omega R$. The azimuthal acceleration is then $\ddot{\phi} \approx \dot{\Omega} \approx -3\Omega\dot{R}/(2R)$.

The radial drift speed follows from equations (4-1), (4-5), (4-6) and (4-7) as

$$\dot{R} \approx -2\eta v_{\rm K}\left(\frac{\tau_{\rm s}}{1+\tau_{\rm s}^2}\right)\,. \tag{4-8}$$

Solids with $\tau_s = 1$ have the fastest infall speed, $-\dot{R} = \eta v_K$. The corresponding timescale

$$\min(t_R) \sim (\eta\Omega)^{-1} \sim 200(R/\mathrm{AU})^{13/14} \text{ yr} \tag{4-9}$$

is a very strong constraint on growth. This constraint is the main element of the meter-sized growth barrier. Fig. 6 plots the radial drift timescales for a range of particle sizes.

To complete this brief introduction to particle aerodynamics, we give the azimuthal drift speed of solids through the (sub-Keplerian) gas as

$$R\dot{\phi} - v_{g,\phi} = \delta v_\phi + \eta v_K = \eta v_K \frac{\tau_s^2}{1+\tau_s^2} \,. \tag{4-10}$$

Large, $\tau_s \gg 1$ solids experience the full ηv_K headwind, yet their radial drift is slow because their inertia is so large. Small, $\tau_s \ll 1$ solids are dragged by the gas and only feel a mild headwind. We thus see why radial drift is fastest near $\tau_s \approx 1$. For these intermediate sizes, drag forces are strong enough to overcome particle inertia, but not so strong as to cause perfect coupling.

These idealized calculations explain the basics of radial drift. A pressing question is whether ignored effects could mitigate the radial drift problem. The existence of a headwind is the most crucial assumption, and it can vanish in localized pressure maxima as addressed below. Even when these maxima exist, headwinds still prevail in the majority of the disk. We also assume that aerodynamic drag only affects the solids, and not the gas component of the disk. When the distributed mass density of solids ρ_p becomes comparable to the gas density ρ_g, then it is no longer acceptable to ignore the feedback of drag forces on the gas. Nakagawa et al. (1986) showed how drift speeds become slower when $\rho_p \gtrsim \rho_g$. This feedback is also the source of powerful drag instabilities — both shearing and streaming — that we address below. Thus there is no simple way to ignore the radial drift problem — its resolution has consequences for how planetesimals form.

4.1.2. Early Collisional Growth

Planetesimal formation begins with the collisional agglomeration of dust grains into larger solids, a process that is observed to proceed up to mm-sizes in T Tauri disks (Williams & Cieza 2011). The conceptually simplest mechanism to form planetesimals is for this collisional growth to proceed past kilometer sizes. However both direct experiment and theoretical arguments show that coagulation beyond mm-sizes is inefficient at best. This inefficiency is particularly problematic due to the timescale constraints imposed by radial drift. The combination of inefficient sticking and rapid infall together comprise the formidable "meter-size" barrier.

Although collision rates do not rule out rapid growth, they place tight constraints on the sticking efficiency To make this conclusion, we approximate the mean collision time as $t_{coll} \sim 1/(\Omega\tau)$, where $\tau \sim \Sigma_p/(\rho_\bullet s)$ is the vertical optical depth. This approximation for the collision rate is good when $\tau_s \gg 1$, and we show below that it suffices for $\tau_s = 1$. The ratio of collision to drift timescales for $\tau_s = 1$ solids is thus roughly

$$\left.\frac{t_{coll}}{t_{drift}}\right|_{\tau_s=1} \sim \frac{\eta}{Z} \sim 0.3 \left(\frac{R}{10\,\mathrm{AU}}\right)^{4/7} \left(\frac{0.01}{Z}\right) \,, \tag{4-11}$$

where we assume Epstein drag, appropriate for the outer disk. We use the result of hydrostatic balance that $\Sigma_{\rm g} \sim \rho_{\rm g} c_{\rm s}/\Omega$. When the collision time exceeds the drift time, collisional growth is ruled out. Even when the two are close, growth requires an efficient rate of sticking per collision. This constraint is most severe in the outer disk.

While turbulent motions increase collision speeds, they do not increase the collision rate above the geometric estimate used to derive eq. (4-11). The reason is that turbulence also increases the particle layer thickness, $H_{\rm p}$, thereby decreasing the mean particle density, $\rho_{\rm p}$. We can compute the collision rate due to turbulence as $t_{\rm coll}^{-1} \sim n\sigma v$. Here the particle number density is $n \sim \Sigma_{\rm p}/(H_{\rm p} m_{\rm p})$, where $m_{\rm p}$ is the particle mass. The particle layer thickness due to turbulent stirring is[4]

$$H_{\rm p} = H_\alpha = \sqrt{\frac{\alpha_D}{\tau_{\rm s}}} H_{\rm g} \, . \tag{4-12}$$

This well-known result (Cuzzi et al. 1993; Carballido et al. 2006; Youdin & Lithwick 2007) normalizes the turbulent diffusion, D, to the dimensionless parameter, $\alpha_D \equiv D/(c_{\rm s} H_{\rm g})$. The cross section is $\sigma \sim s^2$ and the relative velocity due to turbulent motions is, $v \sim \sqrt{\alpha \tau_{\rm s}/(1+\tau_{\rm s}^2)} c_{\rm s}$ (Markiewicz et al. 1991; Chiang & Youdin 2010). For $\tau_{\rm s} > 1$, the collision rate necessarily agrees with the optical depth estimate. For $\tau_{\rm s} < 1$, the collision rate is also independent of the strength of turbulence as $t_{\rm coll}^{-1} \sim Z\Omega$. These cases agree at $\tau_{\rm s} \sim 1$ and confirm the constraint set by eq. (4-11).

Collision rates are not the only concern. Collisions can also result in bouncing or fragmentation that stalls, or even reverses, growth. Below speeds of ~ 1 m s^{-1}, small dust grains stick efficiently as a consequence of van der Waals interactions and the efficient dissipation of kinetic energy (Chokshi et al. 1993; Blum & Wurm 2000). As particles grow and as collision speeds increase, the collisional kinetic energy increases. Short range sticking forces cannot match this increase in kinetic energy, because they are surface area limited (Youdin 2004). Experimental work confirms that collisions between equal mass objects do not produce growth beyond $\sim$ mm-sizes (Blum & Wurm 2008).

Collisions between lower mass projectiles and higher mass targets offer another route to growth. In this scenario impact speeds exceed the meters-per-second value expected to produce growth. As explained above, since small solids are tied to the gas flow, they impact larger solids (which decouple from the gas) at the full headwind speed, $\eta v_{\rm K} \gtrsim 25$ m s^{-1}. Indeed when the latest experimental results are combined with dynamical estimates of collision speeds for a dispersion of particle sizes, growth stalls at only millimeter sizes (Zsom et al. 2010).

Based on observed SEDs, disks likely find a way to overcome these obstacles and grow solids beyond mm-sizes (Williams & Cieza 2011). The mechanisms responsible for enhanced coagulation remain unclear. The particle concentration mechanisms discussed below could augment particle sticking. As shown explicitly in Johansen et al. (2009b), collision speeds are reduced in dense particle clumps.

Most experimental work on grain-grain collisions uses porous silicates. If ices are stickier, growth beyond mm-sizes is possible. In the low pressure of disks, ices sublimate; there is no liquid available to make the equivalent of wet snow. Saturn's rings are an excellent laboratory to explore the outcomes of gentle, $\sim$ mm s^{-1}, collisions between ices (Youdin & Shu 2002). Here, sticking

[4]To accommodate the even mixing of small grains (not our current concern) we require $H_{\rm p} \leq H_{\rm g}$.

forces are constrained by their inability to overcome tidal shear and produce growth beyond ~ 5 m objects. Terrestrial experiments on low temperature ices suggest that cm-sized frosty objects stick at collision speeds below ~ 0.1 m s^{-1} (Supulver et al. 1997). While possibly a crucial ingredient, this limit appears insufficient to allow icy surfaces to bridge the meter-size barrier.

4.2. Gravitational Collapse of Solids into Planetesimals

Self-gravity provides a qualitatively different route to the formation of planetesimals. Instead of bottom-up growth, the gravitational instability (GI) hypothesis of Safronov (1969) and Goldreich & Ward (1973) offers a top-down approach. In this theory, a sea of small solids collapses coherently into a gravitationally bound planetesimal. This collapse does not rely on sticking forces, proceeds faster than radial drift, and bypasses the meter-size barrier.

The gravitational collapse hypothesis encounters several theoretical difficulties. The crucial issue is the ability of turbulent gas to prevent collapse (Weidenschilling 1995). Until recently, these theoretical obstacles seemed insurmountable. Progress in coupled particle-gas dynamics has led to a revival (Youdin & Shu 2002; Johansen et al. 2006, 2007; Cuzzi et al. 2008; Youdin 2011a). Some of these mechanisms use aerodynamic concentration as the initial concentration mechanism (S4.3) but all eventually rely on self-gravity for the final collapse to solid densities.

We focus in this subsection on "pure" gravitational collapse from a relatively smooth background. Although separating these processes from aerodynamic concentration is artificial, this historical approach allows us to isolate the main issues of each mechanism. We first discuss the standard model of gravitational collapse of a disk of solids, which has many similarities to gravitational instabilities in a gas disk (§5). We then briefly describe how gas drag changes this standard picture, a research area where progress is still being made.

The simplest criterion for gravitational collapse requires self-gravity to overcome the tidal distortion of the central star. This condition is met when the particle density exceeds the Roche limit,

$$\rho_{\rm p} > \rho_{\rm R} \simeq 0.6 \frac{M_\star}{R^3} \simeq 130 \frac{\sqrt{m_\star}}{F} \left(\frac{R}{\rm AU} \right)^{-3/14} \rho_{\rm g} \,, \tag{4-13}$$

where $m_\star = M_\star / M_\odot$ and F is the mass enhancement factor for the MMSN from §2. Sekiya (1983) derives this result for the case of a disk midplane with solids perfectly coupled to an incompressible gas, making use of the powerful formalism of Goldreich & Lynden-Bell (1965). The relation of this critical density to the Toomre (1964) Q criterion for GI is discussed (in the context of planetesimals) by Chiang & Youdin (2010) and Youdin (2011a).

For a given particle surface density, eq. (4-13) implies that planetesimals form with a mass $M_{\rm ptml} \sim \Sigma_{\rm p}^3 / \rho_{\rm R}^2$. After contraction to solid densities, the planetesimal size is

$$R_{\rm ptml} \sim \frac{\Sigma_{\rm p}}{\rho_\bullet^{1/3} \rho_{\rm R}^{2/3}} \approx 5 \frac{F Z_{\rm rel}}{m_\star} \sqrt{\frac{R}{\rm AU}} \ {\rm km} \,. \tag{4-14}$$

Though the current relevance is not so clear, this kind of estimate played a key role in defining the canonical planetesimal size to be near a kilometer.

To satisfy the density criterion of eq. (4-13), solids must settle vertically to a midplane layer with thickness $H_{\rm R} = \Sigma_{\rm p} / \rho_{\rm R}$. Even the faintest whiff of turbulence probably produces a much

thicker layer. Although the disk midplane could be a "dead zone" devoid of magnetized turbulence (Gammie 1996), interactions among particles can drive enough turbulence to halt settling (Youdin 2010).

Vertical shear instabilities usually prevent the sedimentation of small particles into a layer thinner than $H_\eta \simeq \eta R$ (Weidenschilling 1980; Youdin & Shu 2002). As particle inertia in the midplane increases from sedimentation, solids begin to drag the midplane gas towards the full Keplerian speed. As in the Kelvin-Helmholz instability, the vertical shear with the overlying particle-poor gas drives overturning. With $H_\eta / H_\mathrm{R} \sim 200$, GI seems ruled out.

The revival of the GI hypothesis requires abandoning two faulty assumptions. The surface density of solids can increase above MMSN — or any initial — values. The evolution of solid and gas components decouples due to drift motions (Stepinski & Valageas 1996). The radial drift of small solids from the outer disk generically leads to "particle pileups," a snowplow effect that increases the surface density in the inner disk (Youdin & Shu 2002; Youdin & Chiang 2004). The local concentration mechanisms discussed in §4.3 can be even more powerful.

The critical Roche density is also too stringent. Planetesimal formation can be triggered when $\rho_\mathrm{p} \gtrsim \rho_\mathrm{g}$, a criterion about a hundred times less severe than the Roche limit in eq. (4-13). Several interesting effects arise when the particle density approaches the gas density. Vertical shear instabilities lose their ability to overturn a layer that is so heavy (Sekiya 1998; Youdin & Shu 2002). When disk rotation is included, the case for particle inertia halting vertical overturning is less clear (Gómez & Ostriker 2005; Lee et al. 2010). However, when perfect coupling is relaxed, and streaming instabilities appear, the relevance of $\rho_\mathrm{p} \gtrsim \rho_\mathrm{g}$ reemerges as the threshold for strong clumping, as described below.

When gas drag is present, the Roche density is not the relevant criteria for GI. Ward (1976, 2000) investigated a dissipative mode of GI that has no formal stability threshold. Collapse always occurs in principle, but it becomes slower and spans a larger radial extent for small particles. Youdin (2011a) included radial turbulent diffusion, and showed that radial spreading — not vertical stirring — is the dominant stabilizing influence for dissipative GI. When vertical stirring is accounted for, it turns out that $\rho_\mathrm{p} \gtrsim \rho_\mathrm{g}$ is typically required for dissipative GI to proceed faster than radial drift. The result that dissipative GI depends so simply on particle inertia is mostly a numerical coincidence and relies on the fact that $Q_\mathrm{g}\sqrt{2\eta} \sim 1$ in the MMSN, see eq. (55) of Youdin (2011a). The important point is that the relevance of particle inertia — specifically the $\rho_\mathrm{p} \gtrsim \rho_\mathrm{g}$ criterion — has been established for a range of mechanisms.

Although this lesser degree of particle settling is substantial, it may require a local enrichment of the disk metallicity, $Z = \Sigma_\mathrm{p}/\Sigma_\mathrm{g}$. If the particle scale-height is set by particle-driven turbulence to H_η, then the particle density exceeds the gas density if

$$Z > \frac{\eta R}{\sqrt{2\pi} H_\mathrm{g}} \simeq 0.014 \frac{1}{\sqrt{m_\star}} \left(\frac{R}{\mathrm{AU}} \right)^{2/7} , \tag{4-15}$$

again with $m_\star = M_\star / M_\odot$. The near agreement with Solar abundances is remarkable and could be related to the correlation of giant planets with host star metallicity (Youdin & Shu 2002). Assuming that the stellar photospheres reflect the abundance of solids in the disk (Fischer & Valenti 2005), the early formation of planetesimals could be a crucial factor in the formation of gas giants (Johansen et al. 2009b).

Though poorly constrained, the role of external (not particle-driven) midplane turbulence may be interesting. For small solids, constraints on the level of turbulence that allows settling to $\rho_{\rm p} \gtrsim \rho_{\rm g}$ are quite stringent. Using eq. (4-12), sedimentation to $\rho_{\rm p} > \rho_{\rm g}$ requires that midplane turbulence satisfy

$$\alpha_D \lesssim 2\pi Z^2 \tau_{\rm s} \approx 10^{-4} Z_{\rm rel}^2 \frac{s}{\rm cm} \left(\frac{R}{10 \text{ AU}} \right)^{3/2} . \tag{4-16}$$

Thus when trying to form planetesimals via GI it helps to have some combination of weak turbulence, particle growth and enriched metallicity ($\Sigma_{\rm p}/\Sigma_{\rm g}$). These requirements become more stringent towards the inner disk (Youdin 2011a).

Thus even in the GI hypothesis, particle growth by coagulation plays a crucial role. Particles must grow until they decouple from the gas. Provided this growth occurs, GI — likely aided by other concentration mechanisms — provides a plausible way past the meter-size barrier.

4.3. Aerodynamic Particle Concentration

We now consider aerodynamic processes that can concentrate particles even when self-gravity is negligible. Many of these processes rely on the presence of turbulence in the disk. This connection raises a general question: does turbulence help or hinder planetesimal formation? By stirring particles, turbulence increases their collision speeds which can lead to more destructive collisions. Furthermore, the diffusive effects of turbulence oppose particle settling and concentration. On the other hand, turbulence can concentrate particles in a variety of ways. Which tendency wins depends on details, notably particle size. Since small solids with $\tau_{\rm s} \ll 1$ drift and settle slowly, they require much weaker turbulence to participate in aerodynamic concentration.

Localized pressure maxima are very powerful particle traps. When the pressure bump takes the form of an axisymmetric ring, the trap is very effective (Whipple 1972). Solids migrate into these rings and accumulate at the center where they encounter no headwind. The MRI naturally produces axisymmetric pressure bumps, via the generation of zonal flows that are somewhat analogous to the surface winds of Jupiter (Johansen et al. 2009a; Fromang & Stone 2009). The relevance of MRI-induced pressure maxima is subject to two caveats: turbulent stirring associated with MRI may lead to destructive collisions and the disk midplane may be insufficiently ionized for the MRI to operate (Turner et al. 2010).

Non-axisymmetric pressure maxima can also trap particles. When the disk is young and massive, spiral arms in the gas probably provide an important source of turbulence (Rice et al. 2006). However, this phase of disk evolution may be too turbulent and/or brief for significant planetesimal formation. Isolated pressure maxima take the form of anticyclonic vortices (Chavanis 2000). Vortices are embedded in, and thus flow with, the sub-Keperian gas (Youdin 2010). Although the vortex center is not a stable point for particle concentration, a point upstream (in the direction of orbital motion) is. The implications for vortex size is discussed in Youdin (2010). The formation and survival of vortices is a topic of ongoing research (Lithwick 2009).

We have so far focused on particle concentration over many orbits where disk rotation and Coriolis forces play a central role. Small turbulent eddies have short turnover times, $t_{\rm eddy} \ll 1/\Omega$, and are unaffected by rotation. In this regime pressure maxima occur not at the centers of anticyclonic vortices, but between vortices of either sign. The concentration of heavy particles in these

regions of low enstrophy (vorticity-squared) was first described in the fluid dynamics community (Maxey 1987).

Cuzzi et al. (2001) applied small-scale concentration to protoplanetary disks. They showed that ~ 1 mm solids — specifically the chondrules that are discussed in §4.4 — can concentrate at the "inner" or dissipation scale of turbulence. These are the smallest eddies that have the shortest turnover time $t_{\rm i}$. Particles with a matching stopping time, $t_{\rm s}, \sim t_{\rm i} \sim 30$ s, are preferentially flung from the eddies and concentrated between them. Chondrules can plausibly satisfy this condition. The ability to concentrate such small particles makes this mechanism unique. The relevance of such brief concentrations is unclear. The characteristic mass involved is also quite small, at most that of a 10 cm rock (Chiang & Youdin 2010).

To overcome these issues, Cuzzi et al. (2008) developed a model that concentrates chondrules on larger scales that contain enough mass to form ~ 100 km-planetesimals. This model involves a somewhat speculative extrapolation. In particular, it assumes that all scales of a turbulent cascade contribute equally to the concentration of chondrule-sized particles. This assumption is a significant deviation from the original mechanism that requires eddy and stopping times to match. See Chiang & Youdin (2010) for further discussion, which concludes that more study of this intriguing mechanism is required.

Clearly particle concentration mechanisms are fraught with uncertainties in the detailed dynamical behavior of gas in protoplanetary disks. Some — certainly not all — of these uncertainties are overcome by the realization that particles can cause their own concentration by collectively altering the gas dynamics (Goodman & Pindor 2000). In the streaming instability of Youdin & Goodman (2005), particle concentrations arise spontaneously from radial drift motions. As described in §4.1.1 these drift motions are an inevitable consequence of pressure support in disks. The linear growth of streaming instabilities is strongest for $\rho_{\rm p} > \rho_{\rm g}$, because particle inertia must be large for drag feedback to influence gas motions. When $\rho_{\rm p} < \rho_{\rm g}$, growth is fastest for $\tau_{\rm s} \approx 1$, when drift speeds are fastest (Youdin & Johansen 2007). While streaming instabilities involve complex dynamics — 3D motions of both the gas and solid components — simplified toy models (Goodman & Pindor 2000; Chiang & Youdin 2010) and considerations of geostrophic balance (Jacquet et al. 2011) help explain how particle density perturbations self-reinforce.

Numerical simulations show that the non-linear clumping from the streaming instability can be quite strong (Johansen & Youdin 2007; Johansen et al. 2009b; Balsara et al. 2009; Bai & Stone 2010a). Particle densities $\gtrsim 10^3 \rho_{\rm g}$ are achieved in the absence of self-gravity, and clumping tends to increase with numerical resolution. The conditions for strong clumping are similar to those giving rapid linear growth: partial decoupling, $\tau_{\rm s} \gtrsim 0.1$, and large particle inertia $\rho_{\rm p} \gtrsim 0.2 \rho_{\rm g}$.

When vertical stratification is included, the midplane particle density evolves consistently due to settling and stirring by both streaming and vertical shearing instabilities. In these simulations, there is a critical disk metallicity for particle clumping which is slightly super-Solar (Johansen et al. 2009b; Bai & Stone 2010a), consistent with eq. (4-15). This metallicity varies with the radial pressure gradient, η; smaller gradients promote clumping (Johansen et al. 2007; Bai & Stone 2010b).

In §4.2, we noted that GI depends on particle growth by coagulation. Since particle sedimentation to $\rho_{\rm p} \gtrsim \rho_{\rm g}$ is a crucial prerequisite, particle growth remains essential when the streaming instability provides the initial particle concentration. However growth need not result in a single particle size, or a very narrow size distribution. Though the smallest solids participate less in

clumping by streaming instabilities, including a dispersion in particle sizes does not prevent strong clumping (Johansen et al. 2007).

The particle concentration produced by the streaming instability is more than sufficient to trigger gravitational collapse. Johansen et al. (2007) formed gravitationally bound objects equivalent to ~ 500 km planetesimals within only a few orbits of initial collapse. More recent simulations suggest the formation of lower mass objects with equivalent ~ 100 — 200 km radii (Johansen et al. 2009b). The crucial differences are the inclusion of the MRI in the earlier study and smaller particle sizes in the second. A more thorough investigation of parameter space, combined with resolution studies, is required. These results exceed the standard estimate of km-sized planetesimals because gravitational collapse occurs not from a smooth background, but from aerodynamically concentrated clumps.

4.4. Observational Constraints on Planetesimal Formation

We now discuss how observations constrain dynamical theories of planetesimal formation. The Solar System provides the most detailed information on planetesimals, and allows comparison between the inner asteroidal reservoir and the Kuiper belt objects and comets of the outer Solar System. The crucial issue is to what extent today's planetesimals reveal the clues of their formation, especially after ~ 4 Gyr of dynamical, collisional and thermal evolution.

Primitive, undifferentiated meteorites give us a hands-on view of the composition of planetesimals. The most common of these are the aptly named "ordinary chondrites." With filling factors up to 90%, they are primarily composed of 0.1-1 mm chondrules. Chondrules are glassy spheres, poetically referred to as "fiery drops of rain" (Sorby 1863). The origin of chondrules — in particular their source of heating — is debated and beyond our scope, see Hewins (1996). The prevalence of chondrules in ordinary chondrites strongly motivates further investigation of the mechanisms that could concentrate solids this small (Cuzzi et al. 2001, 2008).

Despite this attractive conclusion, chondrules may not be the universal building blocks of all planetesimals. Because their abundances most closely match Solar, the CI class of chondrites is considered the most primitive (Lodders 2003). Yet CI chondrites contain no chondrules. It is also unclear whether chondrules were present in the first generation of planetesimals. Most chondrules formed at least 1.5 Myr and up to 4 Myr after the rarer CAIs (Calcuim-Aluminum Inclusions; Connelly et al. 2007; Krot et al. 2007). Thus, planetesimals probably formed before major chondrule forming events, especially the planetesimals that formed the cores of Jupiter and Saturn. Since planetesimals that form early will trap more radioactive heat and differentiate, it seems likely that the undifferentiated chondrites represent a later phase of planetesimal formation (Kleine et al. 2005). The relation between chondrules, meteorites and planetesimal formation continues to be the focus of intense interdisciplinary research.

Planetesimals that remain in the asteroid belt can also provide clues to their formation. The radially banded zonation of different spectral classes of asteroids is well known (Gradie & Tedesco 1982). This observation suggests separate formation epochs, with each event creating a "clan" of chemically and spectrally similar planetesimals. Youdin (2011a) proposed large-scale, drag mediated GI as the cause of these events.

The size distribution of objects within planetesimal belts provides other clues to their for-

mation. Breaks in the size distribution — i.e. changes in its powerlaw slope — point to shifts in formation and/or erosion processes. The asteroid belt has a break near a radius $\sim$ 50 km. Morbidelli et al. (2009a) argue that the asteroids with radii $\gtrsim$ 50 km reflect their initial sizes. Specifically they assert that the largest asteroids have undergone minimal collisional evolution and could not have formed via collisional growth of smaller planetesimals. Since most of the mass is contained in the largest asteroids, their model plausibly produces the numerous small objects below the break via collisional disruption. That interpretation places GI as the preferred formation mechanism. By including streaming instabilities, the simulations of Johansen et al. (2007) predicted that large initial sizes were possible. Conclusively proving that a size distribution is unobtainable by collisional growth is rather difficult. Weidenschilling (2010) contends that collisional growth of asteroids can be accomplished starting with 0.1 km planetesimals — which themselves presumably grew by coagulation past the meter-size barrier.

Curiously, the Kuiper belt also has break in its size distribution at $\sim$ 50 km radii (Bernstein et al. 2004). This break is not measured directly; a combination of an observed luminosity distribution and an estimate of the albedo yields the distribution of radii (Petit et al. 2008). Ongoing surveys of the Kuiper belt seek to provide constraints on the size distribution for the various components of the Kuiper belt.

Understanding the origin of the break requires a model for KBO formation and dynamical interactions with gas giants. Reproducing the observed size distribution with collisional growth models requires an initially massive Kuiper belt followed by dynamical depletion; a break occurs when depletion excites erosive collisions among KBOs with radii below the break (Kenyon & Bromley 2004c). The break radius depends on excitation; more (less) excitation by more (less) massive gas giants yields a break at larger (smaller) radii. Matching the location of the break and the apparent slope of the KBO size distribution below the break requires numerical calculations with growth and depletion, which are an active area of research (Kenyon et al. 2008a; Morbidelli et al. 2008).

The relative roles of collisional and dynamical depletion affect the interpretation of the KBO size break. Pan & Sari (2005) argue that the break is not primordial but due to ongoing collisional erosion that continues to push the break to larger sizes. However Nesvorný et al. (2011) claim that this collisional history is ruled out on two grounds. First the collisional strengths required for such destruction are too weak. Second, such an intense collisional bombardment would destroy the observed Kuiper belt binaries.

The observed binary fraction in the cold, classical Kuiper belt is $\gtrsim$ 20% (Noll et al. 2008). The colors of the two components of Kuiper belt binaries are nearly identical, a fact interpreted as representing a common chemical composition (Benecchi et al. 2009). This observation provides the most compelling support for the GI hypothesis in the outer Solar System, or perhaps anywhere. Gravitational collapse can naturally produce binary planetesimals as a consequence of angular momentum conservation during the contraction of a swarm of small solids (Nesvorný et al. 2010). Binaries — and higher-order multiples — formed this way should have the same chemical composition since they formed from the same well-mixed clump of small solids. While mechanisms for the dynamical capture of KBO binaries are well developed (Goldreich et al. 2002; Noll et al. 2008), these models do not obviously explain matching colors. Moreover the physical conditions require for capture, make the collisional survival of these binaries questionable (Nesvorný et al. 2011), especially for wide binaries (Parker & Kavelaars 2012).

Outside the solar system, exoplanets and debris disks inform the prevalence and consequences of planetesimal formation. The higher incidence of giant planets around stars with super-Solar metallicities (discussed in §2.3) might be tied to planetesimal formation. As shown in eq. (4-15), this connection is strongly suggested by the super-Solar *disk* metallicity threshold for strong clumping by streaming instabilities. Since the disk metallicity can increase over time (Youdin & Chiang 2004), this threshold does not imply that lower metallicity stars can never form planetesimals.

Indeed, the streaming instability/GI model explains why lower metallicity and lower mass stars should form less massive planets (Johansen et al. 2009b). Either directly or by the passage of time, enriching the disk metallicity involves the loss of gas. Thus the initially low metallicity systems that require enrichment are less likely to form giant planets. This conclusion is especially true in the lower mass disks thought to surround lower mass stars. These general trends are revealed by radial velocity surveys (Sousa et al. 2008; Johnson et al. 2010). The *Kepler* transit survey will test these trends, since it is finding striking numbers of small, short period planets (Howard et al. 2011; Youdin 2011b). Characterization of the *Kepler* stars will thus powerfully constrain planetesimal formation models.

5. PLANETESIMALS TO PLANETS

Once planetesimals become larger than a few kilometers — potentially they are born much larger as discussed above — gravitationally focused collisions dominate growth into protoplanets. The size when "planetesimals" become "protoplanets" is vague. Although we use the terms interchangeably, ∼1000 km is a useful threshold. Depending on location and gas temperature, ∼1000 km protoplanets are the smallest planets capable of binding disk gas into an atmosphere.

We describe the accretion of solid protoplanets in §5.1. We start by discussing the processes that operate in a gas-free disk, including gravitationally focused collisions (§5.1.2), velocity excitation (§5.1.3) and collisional fragmentation (§5.1.4). Wh then describe planetesimal interactions with the gaseous disk (§5.1.5). Section 5.1.6 describes simulations of terrestrial planet formation that put these ingredients together. The accretion of a gaseous atmosphere (§5.2) affects planetesimal accretion (§5.2.2) and transforms a planetary core into a gas giant (§5.2.3, §5.2.4). We discuss numerical simulations combining the growth of giant planet cores and atmospheres in §5.2.5. Finally, a young, massive gas disk might fragment directly into a gas giant or a brown dwarf. Section 5.3 describes this formation channel and whether it might explain some exoplanets, especially massive giants at large radial distances.

5.1. Growth of Solid Protoplanets

Unlike planetesimal formation, it is easy to understand why planetesimals grow into larger protoplanets, even if the details are complicated. For the largest planetesimal in any region of the disk, collisions essentially always result in growth. Planetesimal velocities cannot be locally excited above the escape speed of the largest protoplanet. Consequently, the kinetic energy of collisions does not exceed the gravitational potential at the surface of the largest protoplanet. Collisions dissipate a fraction, sometime quite large, of the impact kinetic energy. Even if the impacting planetesimal shatters, growth is assured.

Collisions among smaller planetesimals, however, often lead to erosion or catastrophic fragmentation. When an external, massive perturber stirs a belt of planetesimals, planetesimals collide at velocities larger than their escape velocity. These high velocity collisions tend to erode or completely shatter planetesimals. The dust and changes in the planetesimal size distribution that result from these collisions are relevant for debris disks and for asteroids and Kuiper Belt objects.

Unlike the planetesimal formation phase, aerodynamic drag no longer plays a starring role in protoplanet growth. However drag can still help regulate planetesimal velocities. The accretion of atmospheres (see §5.2) also affects planetesimal capture.

Deriving the precise evolution of a swarm of planetesimals is a complex numerical problem being attacked from several angles (§5.1.6). However, we can develop a reasonably accurate picture of the evolution with the "two groups approximation" reviewed in greater detail by Goldreich et al. (2004). This approximation considers interactions between small, low mass planetesimals with mass m_s and larger, more massive planetesimals with mass m_l. The planetesimal masses $m_{s,l} = 4\pi r_{s,l}^3 \rho_\bullet / 3$ are related to their radii $r_{s,l}$ and internal mass density, which we fix at $\rho_\bullet = 2\,\mathrm{g\,cm^{-3}}$ unless stated otherwise. Neighboring planetesimals have similar semimajor axes, a, and orbital frequencies, Ω. Though detailed treatments need not make this approximation, we equate orbital eccentricities $e_{s,l}$ and inclinations (in radians), but allow e_s and e_l to differ. The random velocities relative to a circular orbit are thus $v_{s,l} \approx e_{s,l} \Omega a$ and the vertical scale heights of the planetesimal disks are $H_{s,l} \approx v_{s,l}/\Omega$. When the nature of the planetesimal is unspecified, we drop the s and l subscripts.

5.1.1. Basic Length and Velocity Scales

A useful scale for studying interactions of planetesimals and protoplanets is the Hill (1878) radius

$$R_H = \left(\frac{m}{3 M_\star} \right)^{1/3} a \ . \tag{5-1}$$

Planetesimals separated by $\lesssim R_H$ are within the Hill sphere where their mutual gravitational attraction dominates the tidal gravity from the central star. While a mutual Hill radius can be defined, in practice it suffices to consider the more massive planetesimal.

The size of a planetesimal in Hill units defines the parameter

$$\psi \equiv \frac{r}{R_H} = \left(\frac{3\rho_\star}{\rho_\bullet} \right)^{1/3} \frac{R_\star}{a} \simeq 6 \times 10^{-3} \left(\frac{\mathrm{M}_\star}{\mathrm{M}_\odot} \right)^{1/3} \left(\frac{\mathrm{AU}}{a} \right) \ , \tag{5-2}$$

where $\rho_\star$ is the mean mass density of the central star. Since $3\rho_\star/\rho_\bullet \sim 1$, the parameter $\psi \sim R_\star/a$ is roughly the angular size of the central star as observed from the planetesimal. The smallness of ψ represents the fact that physical collisions are rare compared to gravitational scattering.

At the Hill radius, the orbital speed about the protoplanet is the Hill velocity

$$v_H = \Omega R_H = \left(\frac{m}{3 M_\star} \right)^{1/3} v_K \ . \tag{5-3}$$

When planetesimal random velocities exceed v_H, two-body encounters are "dispersion-dominated," negligibly affected by orbital shear. Random speeds below v_H cause "shear-dominated" encounters

that involve (restricted) three-body dynamics. We describe below how the Hill velocity divides different accretion regimes.

The outcome of a shear dominated encounter between planetesimals depends on the difference in semimajor axes δR, relative to the Hill radius (Petit & Henon 1986). When $\delta R \lesssim 1$–$2\ R_H$, the two planetesimals are deflected on a horseshoe orbit. More distant encounters with $\delta R \gtrsim 2\sqrt{3}R_H$ result in small angle scattering. For intermediate separations, $1\text{–}2\ R_H \lesssim \delta r \lesssim 2\sqrt{3}R_H$, planetesimals enter the Hill sphere, experience chaotic deflections, and (if no collision occurs) leave the Hill sphere with typical relative velocity v_H.

In Hill units, the escape speed from the surface of a protoplanet, $v_{esc} = [2Gm/r]^{1/2}$, is $v_{esc} \sim v_H/\psi^{1/2}$. Planetesimal velocities can be gravitationally excited up to the escape speed of the largest protoplanet. To estimate when a massive protoplanet might eject nearby planetesimals (or protoplanets), we compare the escape velocity of the protoplanet to the orbital escape velocity, $v_{esc,\star} \approx \sqrt{2}v_K$. When

$$\frac{v_{esc}}{v_{esc,\star}} \approx 0.15 \left(\frac{m}{\mathrm{M}_\oplus}\right)^{1/3} \left(\frac{a}{\mathrm{AU}}\right)^{1/2} \left(\frac{\mathrm{R}_\star}{\mathrm{R}_\odot}\right)^{-1/2} \tag{5-4}$$

exceeds unity, a planet of mass m can eject other nearby protoplanets. Terrestrial planets like Earth are too low mass and too close to the Sun to eject objects. The four Solar System giants can all eject planetesimals; Jupiter is the most efficient at ejecting comets (and spacecraft) from the Solar System (Fernandez & Ip 1984). Aside from collisional grinding, eq. (5-4) implies that planetesimal formation is more efficient closer to a star.

The concepts of the Hill sphere and the Roche lobe are identical, though often used in different contexts. Both describe the region where the gravity of an object exceeds the tidal perturbation from its companion. Formally, both volumes are defined by the critical equipotential containing the L_1 and L_2 Lagrange points. The Roche lobe is more distorted than a sphere when it describes binary stars that are similar in mass. The Roche radius or Roche limit describes the distance from a primary object at which the secondary becomes tidally disrupted and might form planetary rings. Aside from order unity corrections due to fluid effects or internal strength, the concept of individual vs. tidal gravity is again identical. To summarize, a secondary is at the Roche limit from the primary when it fills its own Hill sphere (or Roche Lobe). For an ensemble of very small planetesimals trying to become a much larger planetesimal, the Roche limit sets the critical density for gravitational collapse (eq. [4-13]).

5.1.2. Gravitationally Focused Collisions

In this section, we describe the growth rates of large protoplanets (subscripted by l) accreting either large protoplanets or smaller planetesimals (unsubscripted). Gravitational focusing is the most important aspect of growth. Smaller random velocities for accreted planetesimals yield larger gravitational focusing factors and shorter growth times. We defer to later sections the self consistent calculation of planetesimal velocities and assume the standard case, $v_l < v_s$. Greenberg et al. (1984), Wetherill & Stewart (1993), Kenyon & Bromley (2008), and references in each paper describe more detailed expressions for growth rates.

We begin with the dispersion-dominated regime where $v > v_{H,l}$. The mass accretion rate results from the usual isotropic expression as $\dot{m}_l = mn\sigma v$. Adopting the surface mass density of

planetesimals, Σ, the number density of planetesimals, n, is

$$mnv = \Sigma\Omega \ . \tag{5-5}$$

The cross section

$$\sigma = \pi(r_l + r)^2 f_{G,disp} \ , \tag{5-6}$$

is the product of the geometric area and the gravitational focusing factor $f_{G,disp}$. If the velocity of the incoming planetesimal at infinity is $v > v_{esc,l}$, there is no gravitational focusing and $f_{G,disp} = 1$. When $v \ll v_{esc,l}$, the speed on impact is roughly $v_{esc,l}$. Angular momentum conservation during a two body encounter sets the impact parameter for a grazing collision as $r_l v_{esc,l}/v$. This expression yields $f_{G,disp} \approx (v_{esc,l}/v)^2$. Including energy conservation gives both cases simultaneously as

$$f_{G,disp} = 1 + \beta(v_{esc,l}/v)^2 \ , \tag{5-7}$$

where $\beta = 1$ for a pure two body interaction and $\beta \approx 2.7$ accounts for anisotropic effects introduced by orbital dynamics (Greenzweig & Lissauer 1990; Spaute et al. 1991; Wetherill & Stewart 1993).

Putting these results together and ignoring order unity coefficients gives the dispersion-dominated growth timescale $m_l/\dot{m}_l$ as

$$t_{disp} \approx \frac{\rho_\bullet r_l}{\Sigma\Omega f_{G,disp}} \ . \tag{5-8}$$

This result is just the geometric collision time over the focusing factor.

For shear-dominated encounters with $v < v_{H,l}$, collision rates are affected by chaotic trajectories inside the Hill sphere (Greenberg et al. 1991; Dones & Tremaine 1993). In this regime, planetesimal disks are thinner than the Hill radius, $H \sim v/\Omega < R_{H,l}$. Thus planetesimals enter the Hill sphere at the 2D mass accretion rate, $\dot{m}_H \sim \Sigma R_{H,l}^2 \Omega$. The probability, P, of a collision within the Hill sphere has two cases. Both use the maximum impact parameter for gravitationally focused collisions $b_{\max} \sim r_l v_{esc,l}/v_{H,l} \sim \psi^{1/2} R_{H,l}$. If the scale height of the disk is (relatively) thick with $H \sim v/\Omega > b_{\max}$, the collision probability $P \sim b_{\max}^2/(R_{H,l}H)$ is the ratio of the collision cross-section to the area of the accreting disk of planetesimals. For a thinner planetesimal disk, $P \sim b_{\max}/R_{H,l}$ is the ratio of the impact parameter to the Hill radius.

Combining the mass flow rate through the Hill sphere with both limits of the collision probability yields the shear dominated growth timescale, $m_l/(P \cdot \dot{m}_H)$, as

$$t_{shear} \sim \frac{\rho_\bullet r_l}{\Sigma\Omega f_{G,shear}} \ . \tag{5-9}$$

This timescale is again expressed as the product of the geometric collision time and a gravitational focusing factor

$$f_{G,shear} \sim \left(\psi\frac{v}{v_{H,l}} + \psi^{3/2}\right)^{-1} \ . \tag{5-10}$$

Thus for $v < \psi^{1/2} v_{H,l}$, gravitational focusing reaches its maximum value of $f_G \sim \psi^{-3/2}$, resulting in the fastest possible growth rate. Because inclination excitation is weak in the shear dominated regime, this fastest thin-disk accretion rate likely applies for all large protoplanets with $v_l < v_{H,l}$ (Goldreich et al. 2004). Aside from this issue of anistropic velocities, the dispersion and shear dominated focusing factors match at $v \sim v_{H,l}$ with $f_G \sim 1/\psi$.

For numerical estimates of growth timescales we consider three cases. For the slow case we take $v > v_{esc,l}$ and no gravitational focusing. For the intermediate case, we identify $v \approx v_{H,l} \approx \psi^{1/2} v_{esc,l}$ as the transition between shear- and dispersion-dominated. The fast case considers the maximum focusing factor $f_G \approx \psi^{-3/2}$ appropriate for $v \lesssim \psi^{1/2} v_{H,l} \approx \psi v_{esc,l}$ (and possibly for higher speeds when planetesimal $i \ll e$). Using eq. (2-2) for the surface density of planetesimals, the growth times become

$$t_{\rm slow} \approx \frac{\rho_\bullet r_l}{\Sigma \Omega} \approx 10^7 \left(\frac{m_l}{\rm M_\oplus}\right)^{1/3} \left(\frac{1}{F Z_{\rm rel}}\right) \left(\frac{a}{\rm AU}\right)^3 {\rm yr} \ . \tag{5-11a}$$

$$t_{\rm int} \approx \frac{\rho_\bullet r_l}{\Sigma \Omega} \psi \approx 5 \times 10^4 \left(\frac{m_l}{\rm M_\oplus}\right)^{1/3} \left(\frac{1}{F Z_{\rm rel}}\right) \left(\frac{a}{\rm AU}\right)^2 {\rm yr} \ . \tag{5-11b}$$

$$t_{\rm fast} \approx \frac{\rho_\bullet r_l}{\Sigma \Omega} \psi^{3/2} \approx 4000 \left(\frac{m_l}{\rm M_\oplus}\right)^{1/3} \left(\frac{1}{F Z_{\rm rel}}\right) \left(\frac{a}{\rm AU}\right)^{3/2} {\rm yr} \ . \tag{5-11c}$$

These mass doubling times increase with protoplanet mass. Thus if gravitational focusing stays fixed or decreases (far from a certainty) these estimates also give the total accumulation time. These expressions omit the dependence on stellar mass and planet density for clarity but the growth times scale $\propto \rho_\bullet^{2/3} / {\rm M_\star}^{1/2}$, $\rho_\bullet^{1/3} / {\rm M_\star}^{1/6}$, and $\rho_\bullet^{1/6} {\rm M_\star}^0$ for the three cases, respectively. Though stellar mass is not a major dynamical effect, it could correlate with disk mass or metallicity (here meaning planetesimal to gas ratio), normalized above by F and $Z_{\rm rel}$, respectively. Higher density protoplanets have smaller cross-sections and grow more slowly, but this effect becomes much less significant as gravitational focusing increases.

Gravitational focusing dramatically speeds up the growth of protoplanets, especially in the outer disk. Without focusing, planets accumulate in $t_{\rm slow} \sim$ tens of Myr inside a few AU and more than 1 Gyr outside 5 AU. While a long growth time for terrestrial planets is acceptable, gas giants must form within a few Myr. Thus, formation of giant planet cores in the outer disk requires strong focusing, when the growth time for a 10 $\rm M_\oplus$ core at 50 AU, $t_{\rm fast} \sim 3$ Myr, is close to the lifetime of most gas disks. If strong focusing occurs, the formation of distant gas giants depends on the ability of cores to accrete gas (Rafikov 2011).

Protoplanet accretion also depends on how the velocity distribution evolves. In dispersion-dominated gravitational focusing, the growth time $t_{disp} \propto 1/r_l$; larger planetesimals grow faster than smaller ones. Although it is not the fastest regime, this "runaway" growth requires that gravitational focusing factors remain in the dispersion-dominated regime. With $v_{esc}/v_H \sim \psi^{-1/2} \propto a^{1/2}$, runaway growth persists longer in the outer disk (Greenzweig & Lissauer 1990).

When the largest protopanets enter the shear-dominated regime, runaway growth ends. For the thick disk case, $t_{shear} \propto r_l^0$ is independent of size. With either no focusing, $t_{\rm slow} \propto r_l$, or the fastest (thin disk) shear-dominated accretion $t_{\rm fast} \propto r_l$, smaller protoplanets grow faster and can catch up to the larger ones. In this "oligarchic" growth, many oligarchs compete to accrete small planetesimals, leading to an ensemble of oligarchs throughout the disk.

As the largest protoplanets grow, they try to accrete all solid material in their vicinity. Two planets on circular orbits separated by a little more than $2\sqrt{3}\ R_H$ are stable (Gladman 1993). However, a fairly stable system with more planets requires larger separations, $\sim B R_H$ with B = 7–10 (Lissauer 1987; Kokubo & Ida 1998). Planets that accrete all material within $B R_H$ are

"isolated." Setting $m_{iso} = 2\pi\Sigma a B R_H$ leads to the isolation mass,

$$m_{iso} = \frac{(2\pi B\Sigma)^{3/2}}{(3\mathrm{M}_\star)^{1/2}} a^3 \approx 0.08 \left(\frac{B}{7}\right)^{3/2} \left(\frac{F Z_{\rm rel}}{0.33}\right)^{3/2} \left(\frac{\mathrm{M}_\star}{\mathrm{M}_\odot}\right)^{-1/2} \left(\frac{a}{\mathrm{AU}}\right)^{3/4} \mathrm{M}_\oplus \quad . \tag{5-12}$$

With $F = 1$ and $Z_{\rm rel} = 0.33$, isolated objects in the terrestrial zone have masses comparable to Mercury and Mars. The MMSN has room for 30–50 isolated objects between the orbits of Mercury and Mars. Because their escape velocities are much smaller than their orbital velocities (eq. [5-4]), isolated protoplanets eventually collide and merge to form Earth-mass planets (Fig. 8).

Outside the snow line, $Z_{\rm rel} = 0.78$ at 5 AU yields an isolation mass of roughly 1 $\mathrm{M}_\oplus$. As we show later, this mass is too small to bind the gas required for a gas giant. Increasing the mass of the MMSN ($F \approx 5$) increases the isolation mass to the 'typical' core mass of 10 $\mathrm{M}_\oplus$ needed for a massive atmosphere. Thus, the MMSN is fine for the terrestrial planets, but it is not massive enough to allow formation of gas giants Simialr to Jupiter and Saturn. The extra mass required is consistent with observations of disks around the youngest stars (§2).

5.1.3. Planetesimal Velocity Evolution

As the previous section makes clear, the evolution of planetesimal velocities establishes the rate protoplanets accrete smaller planetesimals. Gravitational scattering is more common than physical collisions; thus, planetesimal velocities rapidly adjust as large protoplanets grow.

Several processes modify the random velocities of planetesimals. The source of random kinetic energy is known as viscous stirring. This process uses planetesimal encounters — predominantly gravitational scattering — to extract energy from orbital shear. Dynamical friction redistributes kinetic energy among planetesimals of different masses, pushing them towards equipartition. Thus, smaller (larger) planetesimals damp (excite) the random velocities of the larger (smaller) planetesimals (Wetherill & Stewart 1989; Kokubo & Ida 1995; Kenyon & Luu 1998). Ignoring ejections and gas drag, physical collisions are the only source of kinetic energy damping. Collisional damping is especially effective for small planetesimals, $r \lesssim$ 1–100 m, that collide frequently (Ohtsuki 1992; Kenyon & Luu 1998). When collisions produce small fragments that collide even more frequently, damping is very efficient. Goldreich et al. (2004) discuss order-of-magnitude derivations of these processes. As with accretion, behaviors vary between the dispersion- and shear-dominated regimes. It is common to refer to the excitation and damping of planetesimal velocities as "heating" and "cooling," respectively.

The main goal of this introduction to velocity evolution is to show that planetesimals cannot be heated above — and can sometimes be cooled significantly below — the escape velocity of the large protoplanets. We focus on dispersion-dominated encounters to explain this result, which is crucial for ensuring the gravitationally focused collisions required to make planets on reasonable timescales.

We first consider the simple case where all planetesimals have the same size. When $v < v_{esc}$, viscous stirring is dominated by gravitational scattering and occurs on the scattering timescale. This heating timescale is well approximated by the two body relaxation time from stellar dynamics (Binney & Tremaine 2008). For the $n\sigma v$ estimate of the gravitational scattering rate, we use eq. (5-5) and compute the cross section $\sigma \sim b_{\rm scatt}^2$ from the impact parameter for strong gravitational

scattering, $b_{\rm scatt} \sim Gm/v^2$. Together, these give the viscous stirring timescale (Ida & Makino 1993)

$$t_{stir,disp} \simeq C_1 \frac{v^4}{G^2 m \Sigma \Omega} \sim \frac{\rho_\bullet r}{\Sigma \Omega} \left(\frac{v}{v_{esc}} \right)^4 \ , \tag{5-13}$$

where the constant $C_1 \approx 1/40$ arises from a more detailed analysis (Ohtsuki et al. 2002), and is similar to the Coulomb logarithm, $\ln \Lambda$, in stellar dynamics (and plasma physics). The final approximate expression in eq. (5-13) facilitates comparison with the collision rates.

The cooling rate is the gravitationally focused collision rate, which follows from eq. (5-8) as

$$t_{cool,disp} \sim \frac{\rho_\bullet r}{\Sigma \Omega} \left(\frac{v}{v_{esc}} \right)^2 \ , \tag{5-14}$$

Balancing the stirring and cooling rates implies $v \sim v_{esc}$. While the correct answer, the reasoning is incomplete. Gravitational focusing is weak for $v \gtrsim v_{esc}$. In this regime, stirring and collisional cooling rates are comparable. A slight imbalance in favor of heating could lead to runaway growth of v and an eventual collisional cascade. This runaway requires nearly elastic physical collisions, as in the collision of two basketballs. In the idealized model of Goldreich & Tremaine (1978), collisions among planetesimals with coefficients of restitution $\gtrsim 0.63$ (comparable to a baseball, but smaller than a basketball or a table tennis ball) bounce often enough to lead to runaway heating. Coefficients of restitution for planetesimals are probably much smaller than 0.5 (Porco et al. 2008); the velocity runaway is unlikely. Similarly sized planetesimals will excite random velocities to the surface escape speed, $v \sim v_{esc}$.

Returning to the two groups approximation, we consider stirring of small planetesimals by large protoplanets. Dynamical friction ensures $v_s > v_l$ (confirmed below); planetesimals dominate the encounter speed. The stirring of small planetesimals by larger ones then occurs on a timescale

$$t_{\rm stir,disp} \sim \frac{\rho_\bullet r_l}{\Sigma_l \Omega} \left(\frac{v_s}{v_{esc,l}} \right)^4 \ . \tag{5-15}$$

Comparison with eq. (5-13) shows that large planetesimals dominate the stirring of small planetesimals when $\Sigma_l m_l > \Sigma_s m_s$. Initially, $\Sigma_s > \Sigma_l$; small planetesimals contain enough mass to affect growth. To dominate stirring, however, large planetesimals can contain a minority of the mass.

Due to stronger stirring by large protoplanets, small planetesimals are excited to $v_s > v_{esc,s}$. At these speeds, collisions between small planetesimals generally cause collisional fragmentation or erosion. The resulting smaller planetesimals then collisionally cool more efficiently. Even without this extra cooling, gravitational focusing arises. When $v_s > v_{esc,s}$, small planetesimals cool by colliding with other small planetesimals on the geometric timescale, $t_{cool} \sim \rho_\bullet r_s / (\Sigma_s \Omega)$. Balancing these heating and cooling rates gives

$$v_s \sim \left(\frac{\Sigma_l}{\Sigma_s} \frac{r_s}{r_l} \right)^{1/4} v_{esc,l} \ . \tag{5-16}$$

When $\Sigma_s > \Sigma_l$, $v_s \ll v_{esc,l}$; small planetesimal accretion is strongly gravitationally focused.

We now consider whether the growth of large protoplanets is dominated by the accretion of small planetesimals or other large protoplanets. Planetesimals with the larger product of surface

density and gravitational focusing, Σf_G, drive the fastest growth (eq. [5-8–5-9]). A balance of viscous self-stirring and cooling by dynamical friction against small planetesimals then sets the velocity dispersion of large protoplanets. For dispersion-dominated encounters this balance gives (for details, see Goldreich et al. 2004)

$$\frac{v_l}{v_s} \sim \left(\frac{\Sigma_l}{\Sigma_s}\right)^{1/4} \quad . \tag{5-17}$$

Since $\Sigma f_{G,disp} \propto \Sigma / v^2$, small planetesimals contribute more to the growth of large protoplanets, by a factor $(\Sigma_s/\Sigma_l)^{1/2} > 1$.

This introduction only begins to touch on the complexities of planetesimal velocity evolution. However even these simple considerations show that gravitationally focused accretion of small planetesimals by large protoplanets is likely. Earlier, we explained that collisional erosion plays a key role in cooling small planetesimals to $v_s > v_{esc,s}$. Now, we turn to even more violent encounters, with $v_s \gg v_{esc,s}$, which lead to catastrophic disruption.

5.1.4. Fragmentation

As large planetesimals grow, they stir up the velocities of smaller planetesimals to the disruption velocity. Instead of mergers, collisions then yield smaller planetesimals and debris. Continued disruptive collisions lead to a collisional cascade, where leftover planetesimals are slowly ground to dust (Dohnanyi 1969; Williams & Wetherill 1994; Kobayashi & Tanaka 2010). Radiation pressure from the central star ejects dust grains with $r \lesssim$ 1–10 μm; Poynting-Robertson drag pulls larger grains into the central star (Burns et al. 1979; Artymowicz 1988; Takeuchi & Artymowicz 2001). Eventually, small planetesimals are accreted by the large planetesimals or ground to dust.

To understand the origin of the collisional cascade, we consider the outcome of a head-on collision between two identical planetesimals. During the impact, some kinetic energy heats up the planetesimals; the rest goes into the internal energy of material in the planetesimals. When the impact energy is small, the extra internal energy is small compared to the binding energy of either planetesimal; the two objects merge into a single, larger planetesimal. When the impact energy is larger than the binding energy, the collision shatters the planetesimals into a few smaller planetesimals and a lot of dust.

Estimating the binding energy of planetesimals relies on two approaches (Davis et al. 1985; Housen & Holsapple 1990, 1999; Holsapple 1994; Benz & Asphaug 1999; Leinhardt et al. 2008; Leinhardt & Stewart 2009). Sophisticated collision experiments yield the internal strengths of small rocky and icy objects, $r \lesssim$ 10–100 cm. Theoretical investigations derive the strength from analytic or numerical models of the crystalline structure and the equation-of-state of the material. In both cases, investigators derive the energy Q_D^* required to remove half of the combined mass of two colliding planetesimals and eject this mass to infinity. Although more sophisticated approaches include the impact velocity in Q_D^*, we focus on a simpler expression that depends only on radius,

$$Q_D^* = Q_b r_s^{\beta_b} + \rho Q_g r_s^{\beta_g} \quad . \tag{5-18}$$

Here $Q_b r_s^{\beta_b}$ is the bulk (tensile) component of the binding energy and $\rho Q_g r_s^{\beta_g}$ is the gravity component of the binding energy.

Laboratory experiments and detailed numerical collision simulations yield a broad range of results for Q_D^* (Fig. 7; Housen & Holsapple 1990; Benz & Asphaug 1999; Holsapple et al. 2002; Leinhardt et al. 2008). In the strength regime at small sizes, the binding energy of a planetesimal depends on the number of flaws – cracks, fissures, etc – in the material. Larger planetesimals have more flaws and smaller strengths. In the gravity regime at large sizes, the binding energy depends on the internal pressure. Larger planetesimals have larger internal pressures and larger strengths. The lower density and weaker crystalline structure of ice leads to smaller strengths than basalts and other rocks.

Models for the breakup of comet Shoemaker-Levy 9 suggest a smaller component of the bulk strength (Asphaug & Benz 1996), implying small disruption energies for small planetesimals (Fig. 7; "Rubble Pile"). A low strength is consistent with numerical simulations of "rubble piles", structures with countless flaws held loosely together. This structure probably results after icy or rocky planetesimals suffer numerous impacts which disrupt the internal structure (removing most of the tensile component of the binding energy) but do not destroy the object.

The collisional cascade begins when the impact energy of colliding small planetesimals equals Q_D^*. Because the random velocities of small planetesimals equal the escape velocities of large planetesimals, the impact energy depends only on the mass of a large planetesimal. Equating this energy to Q_D* allows us to derive the "disruption mass," the mass of a large planetesimal at the onset of the collisional cascade. With $v_{esc,s} \ll v_{esc,l}$, the impact energy per unit mass in the center-of-mass frame is roughly $v^2/8 \approx v_{esc,l}^2/8$. Setting this energy equal to Q_D^*, we solve for the disruption mass:

$$m_d = \left(\frac{3}{4\pi\rho_\bullet}\right)^{1/2} \left(\frac{8Q_D^*}{G}\right)^{3/2} \sim 3.5 \times 10^{-6} \rho_\bullet^{-1/2} \left(\frac{Q_D^*}{10^7 \text{ erg g}^{-1}}\right)^{3/2} \text{M}_\oplus. \quad (5\text{-}19)$$

When small planetesimals have sizes exceeding $\sim$ 1 km, Q_D^* is fairly independent of their composition. For typical $Q_D^* \approx 10^7 - 10^9$ erg g^{-1}, the disruption mass is roughly 0.003–3 Pluto masses. Collisional cascades begin well before planets reach their final masses.

Once disruption commences, the final mass of a planet depends on the timescale for the collisional cascade (Kenyon & Bromley 2004a, 2008; Leinhardt & Richardson 2005). If disruptive collisions produce dust grains much faster than planets accrete planetesimals, planets cannot grow much larger than the disruption radius and have a maximum mass $m_{l,max} \approx m_d$. However, if planets accrete grains and leftover planetesimals effectively, planets reach the isolation mass before collisions and radiation pressure remove material from the disk ($m_{l,max} \approx m_{iso}$; Goldreich et al. 2004).

In a gas-free environment, larger m_d in the inner disk enables planets to accrete much of the debris before destructive collisions and radiative processes remove it. Rocky planet masses then approach the isolation mass. In the outer disk, smaller planets cannot accrete debris before it is lost. Icy planets cannot grow much larger than m_d.

5.1.5. Planetesimal Accretion with Gas Damping

Gas slows the random velocities of smaller planetesimals. Larger protoplanets are less affected by drag and are damped by dynamical friction. The drag force, F_D, of eq. (4-4) damps the kinetic

energy of planetesimals (now with size r_s, not the size s of dust, pebbles, and boulders) at a rate $t_{gas} \equiv v_s(dv_s/dt)^{-1} = v_s(F_D/m_s)^{-1}$. With $\rho_{\rm g} \sim \Sigma_{\rm g}\Omega/c_{\rm s}$, where $c_{\rm s}$ is the gas sound speed,

$$t_{gas} \sim \frac{1}{C_D}\frac{\rho_\bullet r_s}{\Sigma_{\rm g}\Omega}\frac{c_{\rm s}}{v_s} \ . \tag{5-20}$$

To understand the impact of damping, we consider an ensemble of small planetesimals stirring themselves (eq. [5-13]). Without gas, small planetesimals excite their velocities to $v_s \sim v_{esc,s}$. If $t_{gas} < t_{coll} \sim \rho_\bullet r_s/(\Sigma_s\Omega)$, drag exceeds collisions as the dominant cooling mechanism. This switch happens when

$$r_s \gtrsim \frac{1}{C_D}\frac{\Sigma_s}{\Sigma_{\rm g}}\frac{c_{\rm s}}{\sqrt{G\rho_\bullet}} \sim 30\left(\frac{R}{\rm AU}\right)^{-3/14} Z_{\rm rel} \quad {\rm km} \ . \tag{5-21}$$

To be damped by gas drag, planetesimals must exceed this minimum size. This somewhat counter-intuitive result (drag is often more significant for smaller bodies) arises from (i) non-linear drag laws and (ii) a velocity scale, $v_{esc,s}$, that increases with size. The numerical value of the size threshold decreases if $Z_{\rm rel}$ is reduced due to an inefficiency of turning dust into planetesimals.

When eq. (5-21) holds, the stronger damping of self-stirred planetesimals ensures $v_s < v_{esc,s}$. Collisions are gravitationally focused and runaway growth begins earlier than in a disk without gas.

As growth proceeds, larger protoplanets dominate the stirring of smaller planetesimals. With stronger stirring, smaller and smaller planetesimals are damped by non-linear gas drag instead of collisions. Even if collisions are initially more significant, gas drag becomes the dominant coolant as growth proceeds. To compute the random speeds of small planetesimals, we assume dispersion-dominated encounters and balance the heating of eq. (5-15) with the cooling of eq. (5-20) to get

$$\frac{v_s}{v_{esc,l}} \sim \left(\frac{1}{C_D}\frac{r_s}{r_l}\frac{\Sigma_l}{\Sigma_{\rm g}}\right)^{1/5} \ . \tag{5-22}$$

With more mass in small planetesimals $\Sigma_l < \Sigma_s \ll \Sigma_{\rm g}$, gravitational focusing, $f_{G,disp} \sim (v_{esc,l}/v_s)^2$, becomes strong. Accretion of small planetesimals can become shear-dominated. As described in §5.1.2, runaway growth transitions to oligarchy (but does not slow down) in the transition to shear-dominated accretion. A self-consistent analysis of these processes is facilitated by the numerical calculations summarized in §5.1.6.

Details aside, the large oligarchs stir small planetesimals past their escape speed and up to the disruption velocity (§5.1.3). Disruptive collisions among small planetesimals produce a collisional cascade, which grinds planetesimals into smaller and smaller objects. Without gas, planetesimals are ground into small dust grains which are dragged into the star by Poynting-Robertson drag or ejected from the planetary system by radiation pressure. With gas damping, the collisional cascade halts at some intermediate size ($\sim$ 10 cm to 10 m), depending on factors such as the mass of the oligarchs, gas density, material strength, and orbital distance. The damped velocities are then slow enough that the oligarchs accrete these small rocks rapidly. This rapid accretion enables oligarchs to reach the isolation mass on short timescales, even in the outer disk (Rafikov 2004; Kenyon & Bromley 2009).

Collisional grinding a set of small planetesimals into small dust grains requires a very depleted gas disk. For the cascade to proceed down to 1–10 μm particles, these grains must decouple from the

gas (on an orbital timescale, we assume for simplicity). Epstein drag applies for low gas densities (and long gas mean free paths). From eq. (4-3a), particles with sizes $s \gtrsim \Sigma_g/\rho_\bullet$ decouple from the gas. From eq. (2-1) the depletion factor (relative to the MMSN) required to avoid entrainment is

$$F \lesssim 10^{-7} \frac{s}{\mu\mathrm{m}} \left(\frac{R}{\mathrm{AU}}\right)^{3/2} \quad . \tag{5-23}$$

This low mass disk may not last very long. Nevertheless, current observational limits only constrain gas surface densities in debris disks to $F \lesssim 1\%$ of the MMSN, not yet sufficient to asses the dynamical significance of gas. ALMA should should place much tighter constraints (see chapter by Moro-Martin).

5.1.6. Numerical Simulations of Low Mass Planet Formation

Analytic estimates provide a good understanding of each piece of the planet formation process. However, putting the whole set of processes into a coherent theory requires numerical calculations. Clusters of computers can now finish an end-to-end calculation in a reasonable amount of time. Several groups are building towards this simulation, but no complete calculation exists.

Constructing numerical simulations of planet formation involves identifying and solving a set of coupled differential equations which describe the evolution of the gaseous disk and the masses and orbital properties of solid objects. Selecting the proper approach depends on the nature of the problem. Hydrodynamics codes address the evolution of the gaseous disk and how planets accrete material and migrate within the disk (D'Angelo et al. 2003; Nelson & Papaloizou 2004). Smooth particle hydrodynamics allows detailed solutions to outcomes of binary collisions between large protoplanets (e.g., Earth-Moon and Pluto-Charon formation; Canup 2008, 2011). Solving the coagulation equation with a fragmentation algorithm yields the mass and time evolution of solid particles ranging in size from 1 μm up to roughly 1000 km (Safronov 1969; Wetherill & Stewart 1993; Kenyon & Luu 1999; Birnstiel et al. 2010). To treat the dynamical evolution of large planets, N-body treatments provide accurate and often fast solutions (Chambers & Wetherill 1998; Chambers 2001; Raymond et al. 2004; Nagasawa et al. 2005; Kokubo et al. 2006).

Most investigations of terrestrial planet formation employ a coagulation code or an N-body code. An N-body code cannot possibly follow the trajectories of the $\gtrsim 10^{12}$ small planetesimals expected in a MMSN. Coagulation models, which treat planetesimals as a statistical ensemble of objects with a distribution of e and i, can solve for the time evolution of their masses and orbits throughout runaway and oligarchic growth (Wetherill & Stewart 1993). Once most of the solid mass is in a few protoplanets, the statistical approach fails. N-body codes can then follow the evolution during the late stages of oligarchic growth and throughout chaotic growth.

Several hybrid codes combine aspects of both approaches (Spaute et al. 1991; Weidenschilling et al. 1997; Bromley & Kenyon 2006; Charnoz & Morbidelli 2007; Raymond et al. 2011). To follow the evolution of the gaseous disk together with the solids, Bromley & Kenyon (2011) solve the radial diffusion equation for the gaseous disk (eq. [3-4]) and employ a merged coagulation + N-body code for the solids. In these treatments, the coagulation code follows solids with masses smaller than the promotion mass, m_{pro}; the N-body code tracks protoplanets with $m > m_{pro}$. Comparisons with other simulations and with analytic theory provide tests of these techniques (e.g., Kenyon & Luu 1998; Fraser 2009; Morbidelli et al. 2009b).

To illustrate the formation process, we summarize results for several calculations of terrestrial planets and gas giant cores. Because this aspect of this field is growing so rapidly, we focus on a few simple examples.

Coagulation codes begin with an ensemble of planetesimals in place at $t = 0$ (Kenyon & Bromley 2010). Planetesimals are placed in concentric annuli according to a fixed initial surface density relation. These planetesimals often have a single size of 1–100 km; sometimes calculations begin with a distribution of sizes. Because dynamical friction efficiently damps the velocities of the largest planetesimals, planets grow faster in calculations with a size distribution of planetesimals. Starting with an ensemble of small planetesimals leads to faster growth than an ensemble of large planetesimals. The initial surface density sets the growth time. Planets grow faster in more massive disks. In many calculations, the planetesimals evolve in a gaseous disk which also evolves in time; the disk evolution may be proscribed in advanced or calculated along with the planetesimals.

Fig. 8 shows the evolution of oligarchs in an evolutionary sequence starting with an ensemble of 1 km planetesimals at 0.4–2 AU. Following a short runaway growth phase, protoplanets with $m \gtrsim m_{\rm pro}$ appear in a wave that propagates out through the planetesimal grid. As these oligarchs continue to accrete planetesimals, dynamical friction maintains their circular orbits and they evolve into "isolated" protoplanets. Eventually, large oligarchs start to interact dynamically at the inner edge of the grid; a wave of chaotic interactions then moves out through the disk until all oligarchs interact dynamically. Once a few large oligarchs contain most of the mass in the system, dynamical friction between the oligarchs and a few leftover planetesimals starts to circularize their orbits. This process excites the lower mass oligarchs and leftover planetesimals, which are slowly accreted by the largest oligarchs. At the end of the calculation, the masses, semimajor axes, and orbital eccentricities of stable planets are similar to those of the terrestrial planets in the Solar System.

Comparisons between the results of hybrid and N-body calculations show the importance of including planetesimals in the evolution. Both approaches produce a few terrestrial mass planets in roughly circular orbits. Because dynamical friction between leftover planetesimals and the largest oligarchs is significant, hybrid calculations produce planets with more circular orbits than traditional N-body calculations. In most hybrid calculations, lower mass planets have more eccentric orbits than the most massive planets, as observed in the Solar System. In both approaches, the final masses of the planets grow with the initial surface density; the number of planets is inversely proportional to the initial surface density of solid planetesimals. However, the overall evolution is faster in hybrid calculations: oligarchs start to interact earlier and produce massive planets faster.

In hybrid calculations, the isolation mass and the number of oligarchs are more important as local quantities than as global quantities. As waves of runaway, oligarchic, and chaotic growth propagate from the inner disk to the outer disk, protoplanets growing in the inner disk become isolated at different times compared to protoplanets growing in the outer disk. Thus, the isolation mass in hybrid models is a function of heliocentric distance, initial surface density, and *time*, which differs from the classical definition (eq. [5-12]).

During oligarchic growth of the simulation in Fig. 8, viscous stirring excites leftover planetesimals to the disruption velocity. A series of separate simulations demonstrates that the collisional cascade produces copious amounts of dust, which absorb and scatter radiation from the central star. Following the growth of protoplanets, the cascade begins at the inner edge of the disk and moves outward. For calculations with a solar-type central star, it takes ~ 0.1 Myr for dust to form

throughout the terrestrial zone (0.4–2 AU). The timescale is ~ 1 Myr for the terrestrial zone of an A-type star (3–20 AU). As the collisional cascade proceeds, protoplanets impose structure on the disk (Fig. 9, left panel). Bright rings form along the orbits of growing protoplanets; dark bands indicate where a large protoplanet has swept up dust along its orbit. In some calculations, the dark bands are shadows, where optically thick dust in the inner disk prevents starlight from shining on the outer disk (Grogan et al. 2001; Kenyon & Bromley 2004a; Durda et al. 2004).

In the terrestrial zones of A-type and G-type stars, the dust emits mostly at mid-IR wavelengths. In calculations with G-type central stars, formation of a few lunar mass objects at 0.4–0.5 AU leads to copious dust production in a few thousand years (Fig. 9, right panel). As protoplanets form farther out in the disk, the disk becomes optically thick and the mid-IR excess saturates. Once the orbits of oligarchs start to overlap (~ 1 Myr), the largest objects sweep the disk clear of small planetesimals. The mid-IR excess fades. During this decline, occasional large collisions generate large clouds of debris that produce remarkable spikes in the mid-IR excess (Kenyon & Bromley 2002, 2005).

In A-type stars, the terrestrial zone lies at greater distances than in G-type stars. Thus, debris formation in calculations with A-type stars begins later and lasts longer than in models with G-type stars (Fig. 9, right panel). Because the disks in A-type stars contain more mass, they produce larger mid-IR excesses. At later times, individual collisions play a smaller role, which leads to a smoother evolution in the mid-IR excess with time. Although the statistics for G-type stars is incomplete, current observations suggest that mid-IR excesses are larger for A-type stars than for G-type stars (see Chapter by Moro-Martin).

Collisional cascades and debris disk formation may impact the final masses of terrestrial planets. Throughout oligarchic growth, roughly $\sim 25\%$ to 50% of the initial mass in planetesimals is converted into debris. For solar-type stars, the disk is optically thick, so oligarchs probably accrete the debris before some combination of gas drag, Poynting-Robertson drag, and radiation pressure remove it. In the disks of A-type stars, the debris is more optically thin. Thus, these systems may form lower mass planets per unit surface density than disks surrounding less massive stars. Both of these assertions require tests with detailed numerical calculations.

5.2. Accretion of Atmospheres

Protoplanetary atmospheres have a rather different character than the mature planetary atmospheres of Solar System planets and exoplanets. The crucial distinction is that protoplanets orbit within a gas disk. The disk supplies the atmosphere's gas and provides an external binding pressure until the planet opens a clean gap. The protoplanetary atmospheres inherits its composition from the disk. However, the fraction of heavy elements that wind up in the core – versus the dust and ablated planetesimals that remain in the atmosphere – is a key uncertainty. This uncertainty crucially affects the mean molecular weight, μ, and opacity, κ, of the atmosphere.

5.2.1. Static Protoplanet Atmospheres

As protoplanets grow, they become massive enough to bind a gaseous atmosphere. The atmosphere is significantly denser than the surrounding disk gas when the core's gravitational binding

energy exceeds the thermal energy of the gas. For a solid core of mass m_c and radius r_c, this occurs when $r_B > r_c$, where the Bondi radius

$$r_B = Gm/c_{\rm s}^2 \ , \tag{5-24}$$

where total planet mass $m = m_c + m_a$, including the gravitationally bound atmosphere's mass, m_a. Equivalently a core with an atmosphere must exceed the Bondi mass

$$m_c > m_B \equiv \sqrt{\frac{3}{4\pi\rho_\bullet}} \frac{c_{\rm s}^3}{G^{3/2}} \simeq 10^{-3} \left(\frac{a}{\rm AU}\right)^{-9/14} \frac{l_\star^{3/8}}{\tilde{\mu}^{3/2}} \ \ {\rm M}_\oplus \tag{5-25}$$

where we use the gas temperature in an irradiated disk (eq. [3-29]) and normalize the stellar luminosity as $l_\star = {\rm L}_\star/{\rm L}_\odot$ and the gas mean molecular weight as $\tilde{\mu} = \mu/(2.4\ m_H)$.

As the core mass increases beyond m_B the atmosphere becomes denser and more massive. The outer boundary of the atmosphere, $r_{out} = \min(r_B, R_H)$, is set by the Bondi radius until the atmosphere fills the Hill sphere. This transition occurs for massive protoplanets, as $r_B > R_H$ requires

$$m > m_{\rm trans} = \frac{c_s^3}{\sqrt{3}G\Omega} \simeq 3 \left(\frac{a}{\rm AU}\right)^{6/7} \frac{l_\star^{3/8}}{\sqrt{m_\star}\tilde{\mu}^{3/2}} \ \ {\rm M}_\oplus \ . \tag{5-26}$$

Comparing to the disk's gas scale-height $H_g = c_s/\Omega$, the criteria $r_B > H_g$ and $R_H > H_g$ also reproduce eq. (5-26) within order unity constants ($m_{\rm trans}$ increases by $3^{3/2}$ for the $R_H > H_g$ criterion). Thus when $m > m_{\rm trans}$ the protoplanet is no longer uniformly embedded in the disk midplane. It can feel the top and bottom of the disk and start to open a gap (see chapter by Morbidelli). Outside ~ 5 AU, the core accretion instability generally occurs for $m < m_{\rm trans}$. Thus the 3D structure of the gas disk can usually be ignored when describing the onset of core accretion (§5.2.3) but not its final evolution (§5.2.4).

The structure of an proplanetary atmosphere obeys the equations (which also govern stellar structure) of hydrostatic balance

$$\frac{dP}{dr} = -\frac{Gm}{r^2}\rho = -\rho g \ , \tag{5-27}$$

mass conservation

$$\frac{dm}{dr} = 4\pi r^2 \rho \ , \tag{5-28}$$

and energy transport by optically thick, $\tau \sim \kappa P/g > 1$, radiative diffusion,

$$\frac{16\sigma_{\rm SB}T^3}{3\kappa\rho}\frac{dT}{dr} = -\frac{L}{4\pi r^2} \ . \tag{5-29}$$

Wherever radiative diffusion would satisfy the Schwarzchild criterion, $d\ln T/d\ln P > \nabla_{\rm ad}$, the energy transport becomes convective. The adiabatic index $\nabla_{\rm ad} = 2/7$ for an ideal diatomic gas, but in general must be determined from detailed equation of state calculations (Saumon et al. 1995; Saumon & Guillot 2004). Because convective transport is efficient, the temperature profile follows an adiabat, $T \propto P^{\nabla_{\rm ad}}$ instead of eq. (5-29) in convective regions. For the ideal gas equation of state, $P = \rho\mathcal{R}T$, with the (specific) gas constant $\mathcal{R} = k_B/\mu m_H$.

The masses of stable atmospheres (that do not undergo the core accretion instability) place interesting constraints on planet formation. In the terrestrial zone, typical isolation masses (eq.

[5-12]) are roughly 0.1 $M_\oplus$. For almost any accretion time, these planets have stable atmospheres with masses much smaller than the planet's mass. Icy planets formed at tens of AU, however, have much larger isolation masses of several $M_\oplus$, and can support much more massive atmospheres. In the Solar System, the dichotomy between terrestrial planets with thin atmospheres and icy planets with massive atmospheres is consistent with our estimates. Once we have a large sample of rocky/icy exoplanets with well characterized atmospheres, we will see if the same dichotomy persists.

5.2.2. Enhanced Planetesimal Accretion

For low mass protoplanets with $r_{out} = r_B$ the size of the atmosphere relative to the core is

$$\frac{r_{out}}{r_c} \simeq 800 \left(\frac{m_c}{10\ M_\oplus} \right)^{2/3} \left(\frac{a}{5\,\mathrm{AU}} \right)^{3/7} \frac{\tilde{\mu}}{l_\star^{1/4}} \ . \tag{5-30}$$

For Mars-mass planets and larger, the radius of the atmosphere is 10 or more times larger than the radius of the core. Extended atmospheres can significantly enhance planetesimal accretion.

When a planetesimal encounters the atmosphere of a protoplanet, it experiences enhanced gas drag. Capture results if the planetesimal loses enough orbital energy. A thin atmosphere has little impact on very large planetesimals; the collisional cross-section is still $\pi r^2 f_g$. For sufficiently small planetesimals, any encounter with the atmosphere allows the planet to capture the planetesimal; the collisional cross-section is then $\pi r_{out}^2 f_g$. For intermediate sizes, the effective cross-section lies somewhere between $\pi r^2 f_g$ and $\pi r_{out}^2 f_g$. To address this regime, Inaba & Ikoma (2003) define an "enhanced radius" r_e, where the collisional cross-section is $\pi r_e^2 f_g$. In this approach, $r_e = r$ for accreting very large planetesimals and $r_e = r_{out}$ for accreting very small planetesimals. However very small rocks and dust grains will be too tightly coupled to the gas to accrete.

Compared to the estimates for dispersion- and shear-dominated growth in §5.1, atmospheres can enhance accretion rates by 1–2 orders of magnitude (Chambers 2008). When leftover small planetesimals have typical radii of 0.1–10 km, an isolated terrestrial planet with a thin atmosphere has a small radius enhancement, $r_e \approx 1 - 2$. Thus, these isolated objects never experience rapid growth from an enhanced radius. Isolated icy planets are more massive and support massive atmospheres. These objects have $r_e \approx 10$ for accreting 0.1–10 km planetesimals and $r_e \approx 3$ for accreting 100+ km planetesimals. Once they develop atmospheres, icy isolated objects rapidly sweep up any leftover planetesimals along their orbits.

5.2.3. The Core Accretion Instability

Low mass protoplanets (near m_B) have low mass, optically thin atmospheres. More massive cores bind thicker atmospheres, which trap the heat of planetesimal accretion. As the heat is radiated away, the atmosphere becomes denser and more massive. When the atmosphere's mass exceeds roughly the core mass, the atmosphere cannot maintain hydrostatic equilibrium and collapses (Harris 1978; Mizuno 1980). This collapse — referred to as the "core accretion instability" — leads to rapid gas accretion and the birth of a gas giant. The critical core mass (sometimes

called the "crossover mass" because collapse occurs when the core and atmosphere masses roughly match) for this instability is often, but not always, ~ 10 M$_\oplus$ (Ikoma et al. 2000; Rafikov 2006).

Near the crtical core mass, real protoplanetary atmospheres are convective in the interior and (for low enough planetesimal accretion rates) radiative in the exterior region that matches onto the disk (Rafikov 2006). However an illustrative, and historically important, calculation by Stevenson (1982) demonstrates the essential features of the core accretion instability by (incorrectly) assuming the atmosphere is completely radiative with constant opacity κ. We summarize this calculation before comparing it to more detailed computations.

Following Stevenson (1982), we calculate the structure and mass in the atmosphere by keeping the mass, m, constant in the hydrostatic balance equation (5-27), i.e. neglecting the detailed variation from $m = m_c$ at the core to $m = m_c + m_a$ at the top. Equations (5-27) and (5-29) then give (temporarily omitting order unity coefficients for clarity)

$$T^3 dT/dP \sim \kappa L/(\sigma_{\rm SB} G m) \ . \tag{5-31}$$

To integrate this equation, we assume (correctly) that P and T are significantly higher at the base of the atmosphere than in the disk. We further keep L constant, appropriate if accreted planetesimals release their kinetic energy at the core's surface. This assumption yields $L = G m_c \dot{m}/r_c$, where $\dot{m}$ is the planetesimal accretion rate. The slowing of planetesimals as they fall through the atmosphere is a minor correction included in detailed numerical models.

With these approximations, eq. (5-31) integrates to a simple $T - P$ profile

$$T \sim \left(\frac{\kappa L}{\sigma_{\rm SB} G m} P \right)^{1/4} \ . \tag{5-32}$$

To obtain the density profile, we use the fact that for a barotropic relation $P \propto T^{\nabla_\infty}$ ($\nabla_\infty = 1/4$ for our example of a constant opacity), the hydrostatic balance equation for an ideal gas integrates to

$$T = \nabla_\infty \frac{G m}{\mathcal{R} r} \tag{5-33}$$

in the atmospheric interior. The density profile follows as

$$\rho \sim \frac{\sigma_{\rm SB}}{\kappa L} \left(\frac{G m}{\mathcal{R}} \right)^4 \frac{1}{r^3} \ . \tag{5-34}$$

More generally, $\rho \propto r^{1-1/\nabla_\infty}$, which is left as an exercise.

The atmosphere's mass follows by integrating eq. (5-28) from r_c to r_{out}:

$$m_a = \frac{\pi^2}{3} \chi \frac{\sigma_{\rm SB}}{\kappa L} \left(\frac{G m}{\mathcal{R}} \right)^4 \simeq 2.0 \frac{\sigma_{\rm SB} \chi}{\kappa \mathcal{R}^4} \frac{G^3 m^4}{\rho_\bullet^{1/3} m_c^{5/3}} t_{acc} \ . \tag{5-35}$$

with $\chi \equiv \ln(r_{out}/r_c)$ and order unity coefficients reinstated (despite the overall approximate nature of the calculation). The final expression relates the protoplanet luminosity to the (current) core growth timescale, $t_{acc} = m_c/\dot{m} = G m_c^2/(r_c L)$. Setting $m = m_c$ we can numerically evaluate

$$m_a \approx 9.4 \left(\frac{m_c}{10 \ {\rm M}_\oplus} \right)^{7/3} \frac{\tilde{\mu}^4}{\kappa_1} \frac{t_{acc}}{\rm Gyr} \ \ {\rm M}_\oplus, \tag{5-36}$$

with $\chi = 6.7$ (from eq. [5-30]) and $\kappa_1 = \kappa/(1\,\mathrm{cm^2\,g^{-1}})$. For the chosen parameters, we are near the crossover mass, $m_a \sim m_c \sim 10$ M$_\oplus$. Fig. 10 shows the behavior of this simple atmosphere model. We emphasize that the numerical values of this simple model are only meant to be illustrative. For instance the core must actually accrete in $t_{acc} \lesssim 10$ Myr $\ll$ Gyr.

The existence of an instability arises from the non-linearities in m_a. Expressing

$$m = m_c + k\frac{m^4}{m_c^{5/3}} \tag{5-37}$$

where k incorporates all the constants in eq. (5-35), we can show that beyond a critical core mass the total mass (unphysically) declines as m_c increases. Using calculus, the turnover[5] occurs where $dm_c/dm = 0$ at $m = m_c^{5/9}(4k)^{-1/3}$ and $m_c = 0.19k^{-3/4}$.

This simple derivation at least qualitatively explains many features of more detailed core accretion models. The strong dependence of the atmospheric mass on μ is supported by studies showing that envelope pollution lowers the critical core mass (Hori & Ikoma 2011). The opacity is very sensitive to the amount and sizes of dust grains (Pollack et al. 1985). One popular way to speed up core accretion is to reduce the opacity (Hubickyj et al. 2005). The "correct" choice of opacity likely varies between planets and is poorly constrained. It is unclear how much dust from ablated planetesimals will remain in the atmosphere. Small grains both contribute significantly to opacity and settle slowly.

High planetesimal accretion rates increase the critical core mass. For very high accretion rates, especially in the inner disk, the protoplanet atmosphere will be fully convective (Rafikov 2006). The atmosphere then matches onto the same adiabat (constant entropy curve) as the disk gas and thus has the lowest possible mass. In this case the formation of gas giants is quite unlikely. If planetesimal accretion stops (or becomes suitably small), the relevant luminosity comes from the Kelvin-Helmolz contraction of the atmosphere. Models that omit planetesimal accretion (but correctly compute contraction) thus provide a meaningful lower limit on the critical core mass (Papaloizou & Nelson 2005).

It has long been postulated that the cores of Solar System giants might correspond to an isolation mass, $\sim$ 5–20 M$_\oplus$, at 5–10 AU, even though this would require a massive planetesimal disk (Pollack et al. 1996). To understand why this assumption is reasonable, we turn to Fig. 10. Initially a low mass planet accretes planetesimals rapidly. With a short accretion time, the puffy atmosphere is well below the crossover mass. As the core grows in mass, two effects bring the atmosphere closer to instability, (i) extra compression of the gas and (ii) fewer and fewer planetesimals to accrete and heat the atmosphere. As the atmosphere cools, the critical core mass drops until it reaches the actual core mass. This cooling is most likely to happen after most planetesimals have been accreted, i.e. at the isolation mass.

[5]Our values differ slightly from Stevenson (1982) because we assume constant accretion time instead of constant mass accretion rate. Further the 3/4 exponent in his eq. (15) is a typo that should be 3/7.

5.2.4. Direct Accretion of Disk Gas (and How it Stops)

When the envelope collapses, the planet starts to accrete gas directly from the protostellar disk. This dynamical process is not amenable to a stellar structure calculation. Direct accretion of gas is similar to accretion of planetesimals by oligarchs; the accretion rate is roughly the product of the planet's cross-section (or impact parameter in the 2D limit), the local gas density (or surface density), and the encounter velocity, which is dominated by Keplerian shear for circular orbits.

Shortly after the core accretion instability, the planet crosses the transition mass (eq. [5-26]) and the relevant accretion radius is the Hill radius, R_H. Since the transition mass also corresponds to the Hill radius exceeding the gas scale height (see discussion after eq. [5-26]) accretion is not at the classic Bondi rate (e.g. Shu 1992). Instead the two dimensional mass accretion rate applies,

$$\dot{m}_{\rm g} \sim \Sigma_{\rm g} \Omega R_H^2 \sim 10^5 \frac{F}{m_\star^{1/6}} \left(\frac{m}{60 \ {\rm M}_\oplus} \right)^{2/3} \left(\frac{5 \ {\rm AU}}{a} \right) \ \frac{{\rm M}_\oplus}{\rm Myr} \ . \tag{5-38}$$

At $5 \times 10^{-7} {\rm M}_\odot \ {\rm yr}^{-1}$, this rate exceeds the accretion rate onto most pre-main sequence T Tauri stars!

Clearly, something must stop this influx of gas. The gaseous isolation mass is one natural stopping point. Applying eq. (5-12) to the gas disk gives

$$m_{\rm iso,g} = \frac{(2\pi B \Sigma_{\rm g})^{3/2}}{(3{\rm M}_\star)^{1/2}} a^3 \approx 2 \frac{F^{3/2}}{m_\star} \left(\frac{a}{5 \ {\rm AU}} \right)^{3/4} \ {\rm M_J} \ . \tag{5-39}$$

While this result appears plausible for Jupiter, most disk models for Jupiter's core require $F \gtrsim 5$, requiring a second mechanism to halt gas accretion (Lissauer et al. 2009).

Opening a gap in the disk — which begins when eq. (5-26) is satisfied — can slow down accretion so that the disk dissipates before the planet reaches the gaseous isolation mass. Since disk lifetimes are at least at least 1–3 Myr, accretion times must be at least this slow to halt growth (without invoking a fine-tuning of core accretion and disk dissipation timescales). Only a wide and relatively clean gap can slow accretion enough to explain final planet masses (D'Angelo & Lubow 2008). The effective viscosity of the disk must be low for a clean gap, which is an especially strong concern for self-gravitating disks (Kratter et al. 2010b, §5.3).

5.2.5. Numerical Simulations of Gas Giant Planet Formation

To conclude this section, Fig. 11 illustrates the evolution of the semimajor axes of icy and gas giant planets from one simulation of material outside the terrestrial zone (e.g., Bromley & Kenyon 2011). The calculation begins with a single 1000 km planetesimal and an ensemble of ~ 1 cm planetesimals in each of 96 annuli from 3 AU to 30 AU. Because the system has large gravitational focusing factors at $t = 0$, each large planetesimal rapidly sweeps up the small planetesimals along its orbit. With growth times proportional to the orbital period (eq. [5-11a]), protoplanets at 3–7 AU grow much faster than those at larger a. Growth produces many isolated mass objects packed closely together. Early on, gravitational interactions among these objects jostle them around into overlapping orbits. After ~ 0.3 Myr, the most massive of these protoplanets begin to scatter lower mass protoplanets to smaller and larger a. Scattered protoplanets sweep up and scatter the large

pre-existing planetesimals in these orbits, accelerating the growth of all large protoplanets. At ~ 1 Myr, the largest protoplanets begin to accrete gas from the disk. As they grow, they scatter lower mass protoplanets to larger and larger a; eventually, they eject some of these low mass protoplanets from the planetary system.

At the end of the calculation at 100 Myr, six planets remain on stable orbits. Two gas giants, with 1 and 3 Jupiter masses, have $a = 5$ AU and 10 AU. Inside these gas giants, a super-Earth with $m \approx 10$ $M_\oplus$ lies on a fairly circular orbit, $e \approx 0.02$ at $a \approx 1.5$ AU. Outside the gas giants, two more super-Earths occupy orbits in a 2:1 resonance. After many exchanges, the orbits of these two planets are likely stable. Finally, a planet with roughly 1.5 times the mass of Saturn rests in an orbit with modest eccentricity, $e \approx 0.1$ at $a \approx 50$ AU. The outcome of this simulation combines some properties of the Solar System – four gas giants at 5–30 AU – along with some properties of known exoplanets – a super-Earth at 1–2 AU.

This example illustrates several important differences between terrestrial and gas giant planet formation.

- Oligarchs form at 1 AU before they form at 5 AU. From eq. ([5-11a]), the growth time scales with the orbital period and the enhancement of the surface density at the snow line. Comparing timescales at 0.4 AU and at 4 AU, we expect a factor of ~ 300 from the orbital period and a factor of 1/2.4 from the snow line enhancement. The factor of ~ 10 ratio of growth times at 0.4 AU and 4 AU in the simulations agrees well with expectations.

- Oligarchs reach chaotic growth faster at 5 AU than at 1 AU. From the discussion in §5.1.2, icy oligarchs at 5 AU have larger isolation masses than rocky oligarchs at 1 AU (eq. [5-12]). Thus, their gravitational interactions are stronger and lead to chaotic growth sooner.

- While rocky planets scatter low mass protoplanets a few tenths of an AU, gas giant planets scatter some low mass protoplanets close to the host star and eject many others from the planetary system. Fortunately, the Solar System avoided either outcome. However, many exoplanets close to their host stars have large e. Although orbital migration probably accounts for exoplanets with small a and nearly circular orbits (Chapter by Morbidelli), producing super-Earths with $a \lesssim 0.4$ AU and $e \gtrsim 0.1$ probably requires planet-planet scattering, as in Fig. 11 (Jurić & Tremaine 2008; Raymond et al. 2011). In a few years, exoplanet statistics will allow critical tests of the ability of migration and scattering to explain the observed (a, e) distribution.

5.3. Direct Formation of Brown Dwarfs and Gas Giants

Though the core accretion is remarkably successful at explaining the diversity of planetary systems, it cannot be proved. It is thus useful to develop alternate theories. Ideally each theory would make testable predictions, but consistency with physics and existing astronomical observations is also provides stringent constraints. Here we consider the leading alternate theory, that a gravitationally unstable gas disk might fragment into bound objects that survive as gas giant planets (Kuiper 1951; Cameron 1978; Bodenheimer et al. 1980; Boss 2000). This theory should not be confused with the hypothesis that the solid component of the proplanetary disk gravitationally collapses into planetesimals (Safronov 1969; Goldreich & Ward 1973; Youdin & Shu 2002, §4.2).

Section 3.6 introduced the idea that disks are gravitationally unstable when the Toomre (1964) criterion,

$$Q = \frac{c_{\rm s}\Omega}{\pi G \Sigma_{\rm g}} \lesssim 1 \ , \tag{5-40}$$

is satisfied for a surface mass density, Σ. There, we outlined basic constraints on the accretion rate and temperature for stable disks. For a fragment to survive it must cool quickly, so that it contracts on an orbital timescale. Analytic theory suggests bound fragments are possible but have the typical masses of brown dwarfs (Rafikov 2005; Kratter et al. 2010b); so far, numerical simulations are inconclusive (D'Angelo et al. 2010; Cai et al. 2010).

To outline the basic issues for gravitational instability, we consider a density perturbation in a disk which satisfies the Toomre Q criterion. For this fragment to continue to contract, it must cool on a sufficiently short timescale (Gammie 2001),

$$t_c < \xi \Omega^{-1} \ . \tag{5-41}$$

For likely conditions within a protoplanetary disk, numerical simulations suggest that the critical value of $\xi \approx 3$ (Gammie 2001; Rice et al. 2003), with uncertainties due to the equation of state and the opacity. Fragments that cannot cool on the orbital timescale will be sheared apart. For the cooling time in a viscous disk with an α-viscosity (eq. [3-14]), this constraint places a limit on α:

$$\alpha \gtrsim 4/[9\xi\gamma(\gamma-1)] \sim 0.3 \, . \tag{5-42}$$

Fragmenting disks also have very high accretion rates.

For the inner disk ($R < 10$ AU), combining the Toomre ($Q \lesssim 1$) and cooling criteria yields fragments only in hot, massive disks (Rafikov 2005; Matzner & Levin 2005). With disk masses comparable to the stellar mass, these conditions probably produce a bound stellar companion instead of a lower mass planet. Although colder, lower mass disks can have $Q \lesssim 1$, their slow cooling times do not allow the fragment to survive.

Forming planet-mass fragments in the outer disk, at 50 - 100 AU, is more attractive. Irradiation (instead of viscous transport) then dominates the energy budget of the disk (D'Alessio et al. 1998). Although estimates for the cooling time are more complicated, an irradiated disk is thought to fragment more readily once it reaches $Q \lesssim 1$ (Rice et al. 2011; Kratter & Murray-Clay 2011).

In any part of the disk, the initial mass of a gravitational fragment is typically $\sim \Sigma_{\rm g} H_{\rm g}^2$ in terms of the disk scale-height $H_{\rm g}$. For the most optimistic assumptions about cooling – specifically that the optical depth $\tau = 1$ – fragment masses are $\gtrsim 5$ M$_{\rm J}$ at 100 AU (Rafikov 2005). Less efficient cooling ($\tau \neq 1$) and closer orbital separations increase the fragment mass. These minimum masses require very cold disks ($T \lesssim 10$ K), which might be achievable in the outer portions of disks in low mass star forming regions like Ophiuchus (Andrews et al. 2009).

While making a fragment with a mass below ~ 10 M$_{\rm J}$ is challenging, keeping the fragment mass low is an even more difficult problem. Disks are likely to fragment before infall from the surrounding molecular cloud ceases. Preventing the disk fragment from accreting this infalling mass is a challenge. As explained in §5.2.4, stopping the flow of disk gas onto a planet requires a low mass and fairly quiescent disk, exactly opposite to the conditions required for an unstable disk. Kratter et al. (2010b) quantifies these issues and concludes that disks in nearby star-forming regions are more likely to produce 25–75 M$_{\rm J}$ brown dwarfs than 1-10 M$_{\rm J}$ planets. The mass problem might

be helped if fragments cool just rapidly enough to remain bound. Then if they migrate inward they would overflow their Roche lobes and be "tidally downsized" (Boley et al. 2010; Nayakshin 2010). This intriguing suggestion cannot yet be considered a solution.

Even if bound Jupiter-mass fragments form, understanding the time evolution of fragments within a $Q \sim 1$ disk requires sophisticated numerical calculations. In smooth particle hydrodynamics (SPH), an ensemble of particles represents the gas; each particle has a set of physical properties and responds to gravity, radiation pressure, and other forces (Benz et al. 1986; Monaghan 1992). Grid-based calculations lay out a set of points where the physical conditions of the gas are specified; solving a set of coupled differential equations yields the time evolution of the conditions at each point (Black & Bodenheimer 1975; Tohline 1980; Pickett et al. 1998).

In both approaches, disks close to the stability limit develop multi-arm spiral structure (Kratter et al. 2010a; Mayer et al. 2002). Spiral modes generate turbulence throughout the disk (Nelson et al. 1998; Gammie 2001). The large amplitudes of these modes create a rippled surface above the disk midplane (Durisen et al. 2001). When the cooling rate is near the critical value ξ, the spiral structure maintains a rough equilibrium, where the amplitude of the spiral modes increases as the cooling rate declines (Mejía et al. 2005; Cai et al. 2006).

When the cooling time is smaller than the local rotational period, as in equation (5-41), the disk fragments (Gammie 2001; Johnson & Gammie 2003; Rice et al. 2003). For astrophysically relevant conditions, fragmentation requires the disk mass be at least 10% of the stellar mass. As the disk mass grows, spiral waves propagate throughout the disk. Within a few rotation periods, fragments form in the densest portions of the spirals (Boley et al. 2010). If the fragments continue to cool rapidly, they grow in mass and become bound objects, otherwise they are sheared apart (Mayer et al. 2004).

The long-term evolution of bound fragments in self-gravitating disks is unclear. Because the numerical calculations involve such a wide range of scales, none can evolve a bound fragment long enough to determine its final fate. If the cooling time is short, and accretion from the disk inefficient bound fragment could become gas giant planets, or more likely brown dwarfs. Such objects might also grow to full-fledged stellar companions (Bonnell & Bate 1994). Overcoming the numerical limits on the calculations requires faster computers and innovative techniques to follow the evolution of fragments in a time-dependent disk.

6. SUMMARY

In the last decade or two, observations have revolutionized our understanding of planetary astronomy. In the 1990's, the thrilling discovery of the Kuiper belt nearly doubled the empirical size of the disk of the Solar System (Jewitt & Luu 1993). A few years later, Mayor & Queloz (1995) discovered an extraordinary exoplanet orbiting only 0.05 AU from the solar-type star 51 Peg. Now, the number of known Kuiper belt objects easily exceeds 1000, including a grand variety of dynamical and taxonomic classes that place interesting constraints on the origin and early evolution of the protosolar nebula (Barucci et al. 2008). Although there are only $\sim$ 1000 confirmed exoplanets, data from *Kepler* and many ground-based programs will certainly push the count past 10,000 in the next decade. Some of these will certainly challenge current ideas about planet formation.

Throughout this onslaught, theorists responded quickly with new ideas (dead zones in disks,

migration, symplectic N-body codes) and variants on old ideas (collisional cascades, disk instabilities, multiannulus coagulation codes). Rapid developments in computing hardware fueled many advances; new analytical approaches drove others.

Today, we have a good basic theory of disk evolution. Despite uncertainties about the initial mass and temperature distribution and the origin of disk viscosity, analytic and numerical disk models provide a good framework for interpreting observations and for exploring the origin of planetary systems. Current research involves combining more elaborate versions of the basic theory (§3) with detailed models for the chemical evolution of disk material. Within the next decade, these investigations should improve our insight into the overall evolution of the disk and the growth and composition of dust grains with sizes $\sim$ 1–10 mm.

We also understand how km-sized or larger planetesimals become planets (§5). Although there are major uncertainties about the onset and the end of gas accretion and the interactions of massive planets with the gas disk, analytic theory and numerical simulations demonstrate that – on 1–10 Myr timescales – ensembles of planetesimals can evolve into terrestrial and gas giant planets within $\sim$ 50 AU of the central star. Comparisons of observations with the predicted masses and orbital properties of planets and the predicted dust masses and luminosity evolution of debris disks are promising and will eventually produce stringent tests of the theory.

Despite these successes, we are still in search of a robust theory for planetesimal formation (§4). Excellent progress on the meter-size barrier isolates the importance of radial drift and the problems associated with direct coagulation models. Some type of instability – either by direct gravitational collapse or a concentration mechanism such as the streaming instability – seems necessary to produce planetesimals on fast timescales. Larger numerical simulations will undoubtedly yield a better understanding of these instabilities. Exploring other physical mechanisms for particle growth and evolution is also essential.

Understanding fragmentation in protostellar disks promises to unify our understanding of star and planet formation. Although many physical and numerical issues remain unresolved, fragmentation is a promising way to produce gas giants and brown dwarfs at $\gtrsim$ 50–100 AU from the parent star. Despite the current lack of large samples of planets in this domain, direct imaging surveys are starting to discover 1–30 M_J objects with $a \sim$ 10–100 AU (Kalas et al. 2008; Marois et al. 2008; Lagrange et al. 2010; Currie et al. 2010; Kraus et al. 2011). With large uncertainties in model atmospheres, assessing the formation mechanism of these objects is difficult. Once large samples of planets and brown dwarfs at 10–100 AU are available, their properties will allow a robust assessment of the core accretion and disk instability mechanisms.

We thank Ben Bromley, Margaret Geller, Paul Kalas, and Kaitlin Kratter for advice and comments on the manuscript. Portions of this project were supported by *NASA's Astrophysics Theory Program* and the *Origin of Solar Systems Program* through grant NNX10AF35G and by Endowment Funds of the Smithsonian Institution.

REFERENCES

Adachi, I., Hayashi, C., & Nakazawa, K. 1976, Progress of Theoretical Physics, 56, 1756

Adams, F. C., Ruden, S. P., & Shu, F. H. 1989, ApJ, 347, 959

Adams, F. C., & Shu, F. H. 1986, ApJ, 308, 836

Alexander, R. D., & Armitage, P. J. 2009, ApJ, 704, 989

Andrews, S. M., & Williams, J. P. 2005, ApJ, 631, 1134

Andrews, S. M., Wilner, D. J., Hughes, A. M., Qi, C., & Dullemond, C. P. 2009, ApJ, 700, 1502

Artymowicz, P. 1988, ApJ, 335, L79

Asphaug, E., & Benz, W. 1996, Icarus, 121, 225

Backman, D. E., & Paresce, F. 1993, in Protostars and Planets III, ed. E. H. Levy & J. I. Lunine, 1253–1304

Bai, X., & Stone, J. M. 2010a, ApJ, 722, 1437

—. 2010b, ApJ, 722, L220

Balbus, S. A., & Hawley, J. F. 1991, ApJ, 376, 214

Balsara, D. S., Tilley, D. A., Rettig, T., & Brittain, S. D. 2009, MNRAS, 397, 24

Barucci, M. A., Boehnhardt, H., Cruikshank, D. P., Morbidelli, A., & Dotson, R. 2008, The Solar System Beyond Neptune, ed. Barucci, M. A., Boehnhardt, H., Cruikshank, D. P., Morbidelli, A., & Dotson, R.

Bath, G. T., & Pringle, J. E. 1982, MNRAS, 199, 267

Bell, K. R., & Lin, D. N. C. 1994, ApJ, 427, 987

Benecchi, S. D., Noll, K. S., Grundy, W. M., Buie, M. W., Stephens, D. C., & Levison, H. F. 2009, Icarus, 200, 292

Benz, W., & Asphaug, E. 1999, Icarus, 142, 5

Benz, W., Slattery, W. L., & Cameron, A. G. W. 1986, Icarus, 66, 515

Bernstein, G. M., Trilling, D. E., Allen, R. L., Brown, M. E., Holman, M., & Malhotra, R. 2004, AJ, 128, 1364

Binney, J., & Tremaine, S. 2008, Galactic Dynamics: Second Edition (Princeton University Press)

Birnstiel, T., Dullemond, C. P., & Brauer, F. 2010, A&A, 513, A79+

Black, D. C., & Bodenheimer, P. 1975, ApJ, 199, 619

Blum, J., & Wurm, G. 2000, Icarus, 143, 138

—. 2008, ARA&A, 46, 21

Bodenheimer, P., Grossman, A. S., Decampli, W. M., Marcy, G., & Pollack, J. B. 1980, Icarus, 41, 293

Boley, A. C., Hayfield, T., Mayer, L., & Durisen, R. H. 2010, Icarus, 207, 509

Bonanno, A., Schlattl, H., & Paternò, L. 2002, A&A, 390, 1115

Bonnell, I. A., & Bate, M. R. 1994, MNRAS, 269, L45

Boss, A. P. 2000, ApJ, 536, L101

Bouvier, J., Alencar, S. H. P., Harries, T. J., Johns-Krull, C. M., & Romanova, M. M. 2007, Protostars and Planets V, 479

Bromley, B. C., & Kenyon, S. J. 2006, AJ, 131, 2737

—. 2011, ApJ, 731, 101

Brush, S. G. 1990, Reviews of Modern Physics, 62, 43

Burns, J. A., Lamy, P. L., & Soter, S. 1979, Icarus, 40, 1

Cai, K., Durisen, R. H., Michael, S., Boley, A. C., Mejía, A. C., Pickett, M. K., & D'Alessio, P. 2006, ApJ, 636, L149

Cai, K., Pickett, M. K., Durisen, R. H., & Milne, A. M. 2010, ApJ, 716, L176

Cameron, A. G. W. 1962, Icarus, 1, 13

—. 1978, Moon and Planets, 18, 5

Canup, R. M. 2008, Icarus, 196, 518

—. 2011, AJ, 141, 35

Carballido, A., Fromang, S., & Papaloizou, J. 2006, MNRAS, 373, 1633

Cassen, P., & Moosman, A. 1981, Icarus, 48, 353

Chambers, J. 2008, Icarus, 198, 256

Chambers, J. E. 2001, Icarus, 152, 205

—. 2009, ApJ, 705, 1206

Chambers, J. E., & Wetherill, G. W. 1998, Icarus, 136, 304

Charnoz, S., & Morbidelli, A. 2007, Icarus, 188, 468
Chavanis, P. H. 2000, A&A, 356, 1089
Chiang, E., & Youdin, A. N. 2010, Annual Review of Earth and Planetary Sciences, 38, 493
Chiang, E. I., & Goldreich, P. 1997, ApJ, 490, 368
Chokshi, A., Tielens, A. G. G. M., & Hollenbach, D. 1993, ApJ, 407, 806
Connelly, J. N., Amelin, Y., Krot, A. N., & Bizzarro, M. 2007, in Workshop on the Chronology of Meteorites and the Early Solar System, 46–47
Connolly, Jr., H. C., Desch, S. J., Ash, R. D., & Jones, R. H. 2006, in Meteorites and the Early Solar System II, ed. Lauretta, D. S. & McSween, H. Y., 383–397
Cumming, A., Butler, R. P., Marcy, G. W., Vogt, S. S., Wright, J. T., & Fischer, D. A. 2008, PASP, 120, 531
Currie, T., Bailey, V., Fabrycky, D., Murray-Clay, R., Rodigas, T., & Hinz, P. 2010, ApJ, 721, L177
Currie, T., Kenyon, S. J., Balog, Z., Rieke, G., Bragg, A., & Bromley, B. 2008, ApJ, 672, 558
Currie, T., & Sicilia-Aguilar, A. 2011, ApJ, 732, 24
Cuzzi, J. N., Dobrovolskis, A. R., & Champney, J. M. 1993, Icarus, 106, 102
Cuzzi, J. N., Hogan, R. C., Paque, J. M., & Dobrovolskis, A. R. 2001, ApJ, 546, 496
Cuzzi, J. N., Hogan, R. C., & Shariff, K. 2008, ApJ, 687, 1432
D'Alessio, P., Canto, J., Calvet, N., & Lizano, S. 1998, ApJ, 500, 411
D'Angelo, G., Durisen, R. H., & Lissauer, J. J. 2010, in Exoplanets, ed. Seager, S., 319–346
D'Angelo, G., Henning, T., & Kley, W. 2003, ApJ, 599, 548
D'Angelo, G., & Lubow, S. H. 2008, ApJ, 685, 560
Dauphas, N., & Chaussidon, M. 2011, Annual Review of Earth and Planetary Sciences, 39, 351
Davis, D. R., Chapman, C. R., Weidenschilling, S. J., & Greenberg, R. 1985, Icarus, 63, 30
Dohnanyi, J. S. 1969, J. Geophys. Res., 74, 2531
Dones, L., & Tremaine, S. 1993, Icarus, 103, 67
Durda, D. D., Bottke, W. F., Enke, B. L., Merline, W. J., Asphaug, E., Richardson, D. C., & Leinhardt, Z. M. 2004, Icarus, 170, 243
Durisen, R. H., Mejia, A. C., Pickett, B. K., & Hartquist, T. W. 2001, ApJ, 563, L157
Espaillat, C., et al. 2012, ApJ, 747, 103
Fernandez, J. A., & Ip, W.-H. 1984, Icarus, 58, 109
Fischer, D. A., & Valenti, J. 2005, ApJ, 622, 1102
Fraser, W. C. 2009, ApJ, 706, 119
Friedjung, M. 1985, A&A, 146, 366
Fromang, S., & Stone, J. M. 2009, A&A, 507, 19
Gammie, C. F. 1996, ApJ, 457, 355
—. 2001, ApJ, 553, 174
Ghosh, P., & Lamb, F. K. 1979, ApJ, 232, 259
Gladman, B. 1993, Icarus, 106, 247
Goldreich, P., Lithwick, Y., & Sari, R. 2002, Nature, 420, 643
—. 2004, ARA&A, 42, 549
Goldreich, P., & Lynden-Bell, D. 1965, MNRAS, 130, 97
Goldreich, P., & Tremaine, S. D. 1978, Icarus, 34, 227
Goldreich, P., & Ward, W. R. 1973, ApJ, 183, 1051
Gómez, G. C., & Ostriker, E. C. 2005, ApJ, 630, 1093
Gonzalez, G. 1997, MNRAS, 285, 403
Goodman, J., & Pindor, B. 2000, Icarus, 148, 537
Gould, A., et al. 2010, ApJ, 720, 1073
Gradie, J., & Tedesco, E. 1982, Science, 216, 1405
Greenberg, R., Bottke, W. F., Carusi, A., & Valsecchi, G. B. 1991, Icarus, 94, 98

Greenberg, R., Weidenschilling, S. J., Chapman, C. R., & Davis, D. R. 1984, Icarus, 59, 87
Greenzweig, Y., & Lissauer, J. J. 1990, Icarus, 87, 40
Grogan, K., Dermott, S. F., & Durda, D. D. 2001, Icarus, 152, 251
Harris, A. W. 1978, in Lunar and Planetary Institute Science Conference Abstracts, Vol. 9, Lunar and Planetary Institute Science Conference Abstracts, 459–461
Hartmann, L., & Kenyon, S. J. 1996, ARA&A, 34, 207
Hayashi, C. 1981, Progress of Theoretical Physics Supplement, 70, 35
Herbig, G. H. 1962, Advances in Astronomy and Astrophysics, 1, 47
Hewins, R. H. 1996, in Chondrules and the Protoplanetary Disk, ed. R. H. Hewins, R. H. Jones, & E. R. D. Scott, 3–9
Hill, G. 1878, Am. Journ. Math., 1, 5, 129, 245
Holsapple, K., Giblin, I., Housen, K., Nakamura, A., & Ryan, E. 2002, in Asteroids III, ed. W. F. Bottke, A. Cellino, P. Paolicchi, & R. P. Binzel (University of Arizona Press, Tucson, AZ), 443–462
Holsapple, K. A. 1994, Planet. Space Sci., 42, 1067
Hori, Y., & Ikoma, M. 2011, MNRAS, 416, 1419
Housen, K. R., & Holsapple, K. A. 1990, Icarus, 84, 226
—. 1999, Icarus, 142, 21
Howard, A. W., et al. 2011, ArXiv e-prints
Hubickyj, O., Bodenheimer, P., & Lissauer, J. J. 2005, Icarus, 179, 415
Hueso, R., & Guillot, T. 2005, A&A, 442, 703
Ida, S., & Makino, J. 1993, Icarus, 106, 210
Ikoma, M., Nakazawa, K., & Emori, H. 2000, ApJ, 537, 1013
Inaba, S., & Ikoma, M. 2003, A&A, 410, 711
Isella, A., Carpenter, J. M., & Sargent, A. I. 2009, ApJ, 701, 260
Jacquet, E., Balbus, S. A., & Latter, H. N. 2011, ArXiv e-prints
Jeffreys, H. 1929, The Observatory, 52, 173
Jewitt, D., Chizmadia, L., Grimm, R., & Prialnik, D. 2007, Protostars and Planets V, 863
Jewitt, D., & Luu, J. 1993, Nature, 362, 730
Johansen, A., Klahr, H., & Henning, T. 2006, ApJ, 636, 1121
Johansen, A., Oishi, J. S., Mac Low, M.-M., Klahr, H., Henning, T., & Youdin, A. 2007, Nature, 448, 1022
Johansen, A., & Youdin, A. 2007, ApJ, 662, 627
Johansen, A., Youdin, A., & Klahr, H. 2009a, ApJ, 697, 1269
Johansen, A., Youdin, A., & Mac Low, M. 2009b, ApJ, 704, L75
Johnson, B. M., & Gammie, C. F. 2003, ApJ, 597, 131
Johnson, J. A., Aller, K. M., Howard, A. W., & Crepp, J. R. 2010, PASP, 122, 905
Johnson, J. A., et al. 2011, AJ, 141, 16
Joy, A. H. 1945, ApJ, 102, 168
Jurić, M., & Tremaine, S. 2008, ApJ, 686, 603
Kalas, P., et al. 2008, Science, 322, 1345
Kennedy, G. M., & Kenyon, S. J. 2008, ApJ, 673, 502
Kenyon, S. J., & Bromley, B. C. 2002, ApJ, 577, L35
—. 2004a, AJ, 127, 513
—. 2004b, ApJ, 602, L133
—. 2004c, AJ, 128, 1916
—. 2005, AJ, 130, 269
—. 2008, ApJS, 179, 451
—. 2009, ApJ, 690, L140
—. 2010, ApJS, 188, 242
Kenyon, S. J., Bromley, B. C., O'Brien, D. P., & Davis, D. R. 2008a, in The Solar System Beyond Neptune, ed. Barucci, M. A., Boehnhardt, H., Cruikshank, D. P., Morbidelli, A., & Dotson, R. (University of Arizona Press, Tucson, AZ), 293–313
Kenyon, S. J., Gómez, M., & Whitney, B. A. 2008b, in Handbook of Star Forming Regions, Volume I, ed. Reipurth, B., 405–+
Kenyon, S. J., & Hartmann, L. 1987, ApJ, 323, 714

Kenyon, S. J., & Luu, J. X. 1998, AJ, 115, 2136
—. 1999, AJ, 118, 1101
Kenyon, S. J., Yi, I., & Hartmann, L. 1996, ApJ, 462, 439
Kleine, T., Mezger, K., Palme, H., Scherer, E., & Münker, C. 2005, Geochim. Cosmochim. Acta, 69, 5805
Kleine, T., et al. 2009, Geochim. Cosmochim. Acta, 73, 5150
Kobayashi, H., & Tanaka, H. 2010, Icarus, 206, 735
Kokubo, E., & Ida, S. 1995, Icarus, 114, 247
—. 1998, Icarus, 131, 171
Kokubo, E., Kominami, J., & Ida, S. 2006, ApJ, 642, 1131
Kratter, K. M., Matzner, C. D., Krumholz, M. R., & Klein, R. I. 2010a, ApJ, 708, 1585
Kratter, K. M., & Murray-Clay, R. A. 2011, ApJ, 740, 1
Kratter, K. M., Murray-Clay, R. A., & Youdin, A. N. 2010b, ApJ, 710, 1375
Kraus, A. L., Ireland, M. J., Martinache, F., & Hillenbrand, L. A. 2011, ApJ, 731, 8
Krot, A., et al. 2007, in Workshop on the Chronology of Meteorites and the Early Solar System, 98–99
Kuiper, G. P. 1951, Proceedings of the National Academy of Science, 37, 1
Lagrange, A.-M., et al. 2010, Science, 329, 57
Lee, A. T., Chiang, E., Asay-Davis, X., & Barranco, J. 2010, ApJ, 725, 1938
Leinhardt, Z. M., & Richardson, D. C. 2005, ApJ, 625, 427
Leinhardt, Z. M., & Stewart, S. T. 2009, Icarus, 199, 542
Leinhardt, Z. M., Stewart, S. T., & Schultz, P. H. 2008, in The Solar System Beyond Neptune, ed. Barucci, M. A., Boehnhardt, H., Cruikshank, D. P., Morbidelli, A., & Dotson, R., 195–211
Lin, D. N. C., & Pringle, J. E. 1987, MNRAS, 225, 607
—. 1990, ApJ, 358, 515
Lissauer, J. J. 1987, Icarus, 69, 249
Lissauer, J. J., Hubickyj, O., D'Angelo, G., & Bodenheimer, P. 2009, Icarus, 199, 338
Lithwick, Y. 2009, ApJ, 693, 85
Lodato, G., & Rice, W. K. M. 2004, MNRAS, 351, 630
Lodders, K. 2003, ApJ, 591, 1220
Lynden-Bell, D., & Pringle, J. E. 1974, MNRAS, 168, 603
Markiewicz, W. J., Mizuno, H., & Voelk, H. J. 1991, A&A, 242, 286
Marois, C., Macintosh, B., Barman, T., Zuckerman, B., Song, I., Patience, J., Lafrenière, D., & Doyon, R. 2008, Science, 322, 1348
Matzner, C. D., & Levin, Y. 2005, ApJ, 628, 817
Maxey, M. R. 1987, Journal of Fluid Mechanics, 174, 441
Mayer, L., Quinn, T., Wadsley, J., & Stadel, J. 2002, Science, 298, 1756
—. 2004, ApJ, 609, 1045
Mayor, M., & Queloz, D. 1995, Nature, 378, 355
Mejía, A. C., Durisen, R. H., Pickett, M. K., & Cai, K. 2005, ApJ, 619, 1098
Mizuno, H. 1980, Progress of Theoretical Physics, 64, 544
Monaghan, J. J. 1992, ARA&A, 30, 543
Morbidelli, A., Bottke, W. F., Nesvorný, D., & Levison, H. F. 2009a, Icarus, 204, 558
—. 2009b, Icarus, 204, 558
Morbidelli, A., Levison, H. F., & Gomes, R. 2008, in The Solar System Beyond Neptune (The University of Arizona Press), 275–292
Nagasawa, M., Lin, D. N. C., & Thommes, E. 2005, ApJ, 635, 578
Najita, J. R., Carr, J. S., Glassgold, A. E., & Valenti, J. A. 2007, Protostars and Planets V, 507
Nakagawa, Y., Sekiya, M., & Hayashi, C. 1986, Icarus, 67, 375
Nayakshin, S. 2010, MNRAS, 408, L36
Nelson, A. F., Benz, W., Adams, F. C., & Arnett, D. 1998, ApJ, 502, 342
Nelson, R. P., & Papaloizou, J. C. B. 2004, MN-

RAS, 350, 849
Nesvorný, D., Bottke, W. F., Levison, H. F., & Dones, L. 2003, ApJ, 591, 486
Nesvorný, D., Vokrouhlický, D., Bottke, W. F., Noll, K., & Levison, H. F. 2011, AJ, 141, 159
Nesvorný, D., Youdin, A. N., & Richardson, D. C. 2010, AJ, 140, 785
Noll, K. S., Grundy, W. M., Chiang, E. I., Margot, J.-L., & Kern, S. D. 2008, in The Solar System Beyond Neptune, The University of Arizona Press, 345–363
Ohtsuki, K. 1992, Icarus, 98, 20
Ohtsuki, K., Stewart, G. R., & Ida, S. 2002, Icarus, 155, 436
Paczynski, B. 1978, Acta Astronomica, 28, 91
Pan, M., & Sari, R. 2005, Icarus, 173, 342
Papaloizou, J. C. B., & Nelson, R. P. 2003, MNRAS, 339, 983
—. 2005, A&A, 433, 247
Parker, A. H., & Kavelaars, J. J. 2012, ApJ, 744, 139
Pasquini, L., Döllinger, M. P., Weiss, A., Girardi, L., Chavero, C., Hatzes, A. P., da Silva, L., & Setiawan, J. 2007, A&A, 473, 979
Payne, C. H. 1925, PhD thesis, RADCLIFFE COLLEGE.
Petit, J., & Henon, M. 1986, Icarus, 66, 536
Petit, J.-M., Kavelaars, J. J., Gladman, B., & Loredo, T. 2008, in The Solar System Beyond Neptune (The University of Arizona Press), 71–87
Pickett, B. K., Cassen, P., Durisen, R. H., & Link, R. 1998, ApJ, 504, 468
Pollack, J. B., Hubickyj, O., Bodenheimer, P., Lissauer, J. J., Podolak, M., & Greenzweig, Y. 1996, Icarus, 124, 62
Pollack, J. B., McKay, C. P., & Christofferson, B. M. 1985, Icarus, 64, 471
Porco, C. C., Weiss, J. W., Richardson, D. C., Dones, L., Quinn, T., & Throop, H. 2008, AJ, 136, 2172
Pringle, J. E. 1981, ARA&A, 19, 137
Pudritz, R. E., Ouyed, R., Fendt, C., & Brandenburg, A. 2007, Protostars and Planets V, 277
Rafikov, R. R. 2004, AJ, 128, 1348
—. 2005, ApJ, 621, L69
—. 2006, ApJ, 648, 666
—. 2011, ApJ, 727, 86
Raymond, S. N., Quinn, T., & Lunine, J. I. 2004, Icarus, 168, 1
Raymond, S. N., et al. 2011, ArXiv e-prints
Rice, W. K. M., Armitage, P. J., Bonnell, I. A., Bate, M. R., Jeffers, S. V., & Vine, S. G. 2003, MNRAS, 346, L36
Rice, W. K. M., Armitage, P. J., Mamatsashvili, G. R., Lodato, G., & Clarke, C. J. 2011, MNRAS, 418, 1356
Rice, W. K. M., Lodato, G., Pringle, J. E., Armitage, P. J., & Bonnell, I. A. 2006, MNRAS, 372, L9
Rivkin, A. S., Howell, E. S., Vilas, F., & Lebofsky, L. A. 2002, Asteroids III, 235
Russell, S. S., Hartmann, L., Cuzzi, J., Krot, A. N., Gounelle, M., & Weidenschilling, S. 2006, in Meteorites and the Early Solar System II, 233–251
Safronov, V. S. 1960, Annales d'Astrophysique, 23, 979
—. 1969, Evoliutsiia doplanetnogo oblaka. (Evolution of the Protoplanetary Cloud and Formation of the Earth and Planets, Nauka, Moscow [Translation 1972, NASA TT F-677] (1969.)
Saumon, D., Chabrier, G., & van Horn, H. M. 1995, ApJS, 99, 713
Saumon, D., & Guillot, T. 2004, ApJ, 609, 1170
Sekiya, M. 1983, Progress of Theoretical Physics, 69, 1116
—. 1998, Icarus, 133, 298
Shakura, N. I., & Sunyaev, R. A. 1973, A&A, 24, 337
Shu, F., Najita, J., Ostriker, E., Wilkin, F., Ruden, S., & Lizano, S. 1994, ApJ, 429, 781
Shu, F. H. 1992, Physics of Astrophysics, Vol. II

(University Science Books)
Shu, F. H., Adams, F. C., & Lizano, S. 1987, ARA&A, 25, 23
Shu, F. H., Najita, J. R., Shang, H., & Li, Z. 2000, Protostars and Planets IV, 789
Sorby, H. C. 1863, Royal Society of London Proceedings Series I, 13, 333
Sousa, S. G., et al. 2008, A&A, 487, 373
Spaute, D., Weidenschilling, S. J., Davis, D. R., & Marzari, F. 1991, Icarus, 92, 147
Stepinski, T. F. 1998, Icarus, 132, 100
Stepinski, T. F., & Valageas, P. 1996, A&A, 309, 301
Stevenson, D. J. 1982, Planet. Space Sci., 30, 755
Stevenson, D. J., & Lunine, J. I. 1988, Icarus, 75, 146
Stone, J. M., & Balbus, S. A. 1996, ApJ, 464, 364
Supulver, K. D., Bridges, F. G., Tiscareno, S., Lievore, J., & Lin, D. N. C. 1997, Icarus, 129, 539
Takeuchi, T., & Artymowicz, P. 2001, ApJ, 557, 990
Terebey, S., Shu, F. H., & Cassen, P. 1984, ApJ, 286, 529
Tohline, J. E. 1980, ApJ, 235, 866
Toomre, A. 1964, ApJ, 139, 1217
Turner, N. J., Carballido, A., & Sano, T. 2010, ApJ, 708, 188
Ward, W. R. 1976, in Frontiers of Astrophysics, ed. E.H. Avrett, 1–40
Ward, W. R. 2000, in Origin of the Earth and Moon, 75–84
Warner, B. 1995, Cambridge Astrophysics Series, 28
Weidenschilling, S. J. 1977a, MNRAS, 180, 57
—. 1977b, Ap&SS, 51, 153
—. 1980, Icarus, 44, 172
—. 1995, Icarus, 116, 433
Weidenschilling, S. J. 2010, in Lunar and Planetary Institute Science Conference Abstracts, Vol. 41, 1453
Weidenschilling, S. J., Spaute, D., Davis, D. R., Marzari, F., & Ohtsuki, K. 1997, Icarus, 128, 429
Weidling, R., Güttler, C., & Blum, J. 2012, Icarus, 218, 688
Wetherill, G. W., & Stewart, G. R. 1989, Icarus, 77, 330
—. 1993, Icarus, 106, 190
Whipple, F. L. 1972, in From Plasma to Planet, ed. A. Elvius, 211–+
Williams, D. R., & Wetherill, G. W. 1994, Icarus, 107, 117
Williams, J. P., & Cieza, L. A. 2011, ArXiv e-prints
Wyatt, M. C. 2008, ARA&A, 46, 339
Youdin, A., & Johansen, A. 2007, ApJ, 662, 613
Youdin, A. N. 2004, in Astronomical Society of the Pacific Conference Series, Vol. 323, Star Formation in the Interstellar Medium, 319
Youdin, A. N. 2010, in EAS Publications Series, Vol. 41, EAS Publications Series, ed. T. Montmerle, D. Ehrenreich, & A.-M. Lagrange, 187–207
Youdin, A. N. 2011a, ApJ, 731, 99
—. 2011b, ApJ, 742, 38
Youdin, A. N., & Chiang, E. I. 2004, ApJ, 601, 1109
Youdin, A. N., & Goodman, J. 2005, ApJ, 620, 459
Youdin, A. N., & Lithwick, Y. 2007, Icarus, 192, 588
Youdin, A. N., & Shu, F. H. 2002, ApJ, 580, 494
Zolensky, M., & McSween, Jr., H. Y. 1988, in Meteorites and the Early Solar System, ed. Kerridge, J. F. & Matthews, M. S., 114–143
Zsom, A., Ormel, C. W., Güttler, C., Blum, J., & Dullemond, C. P. 2010, A&A, 513, A57

This preprint was prepared with the AAS LaTeX macros v5.2.

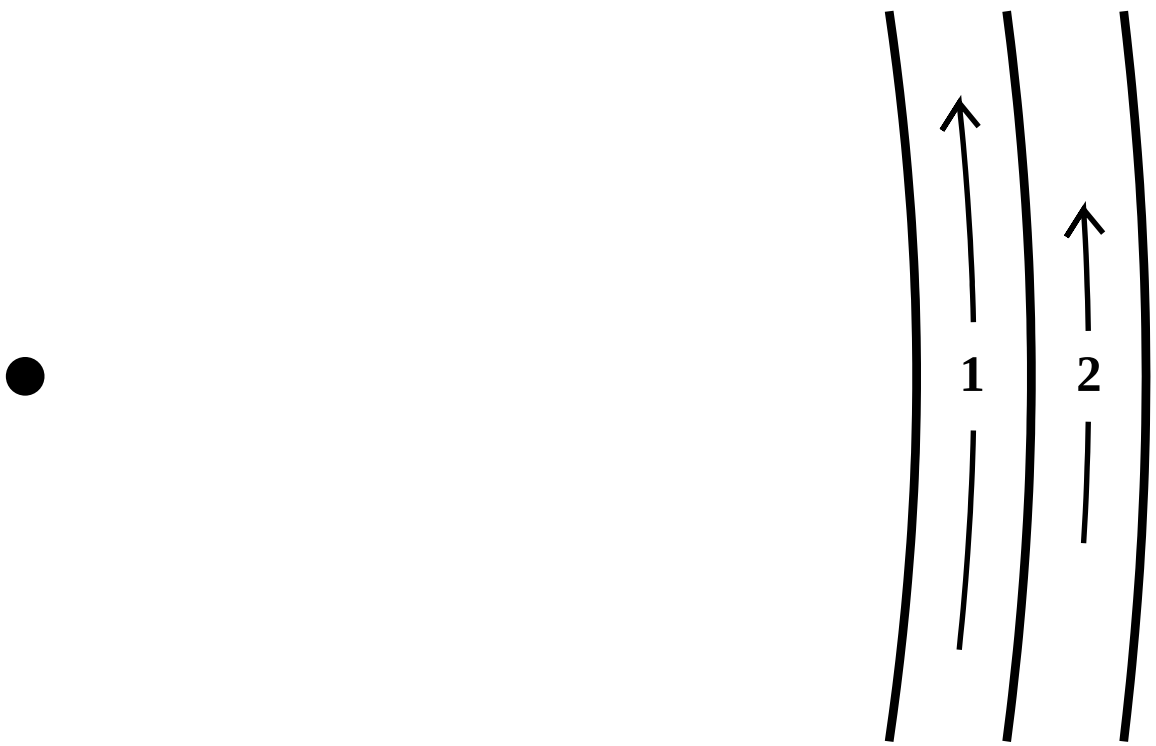

Fig. 1.— Schematic view of two adjacent annuli in a disk surrounding a star (black point at left). Annulus 1 lies inside annulus 2; material in annulus 1 orbits the star more rapidly than material in annulus 2 ($\Omega_1 > \Omega_2$).

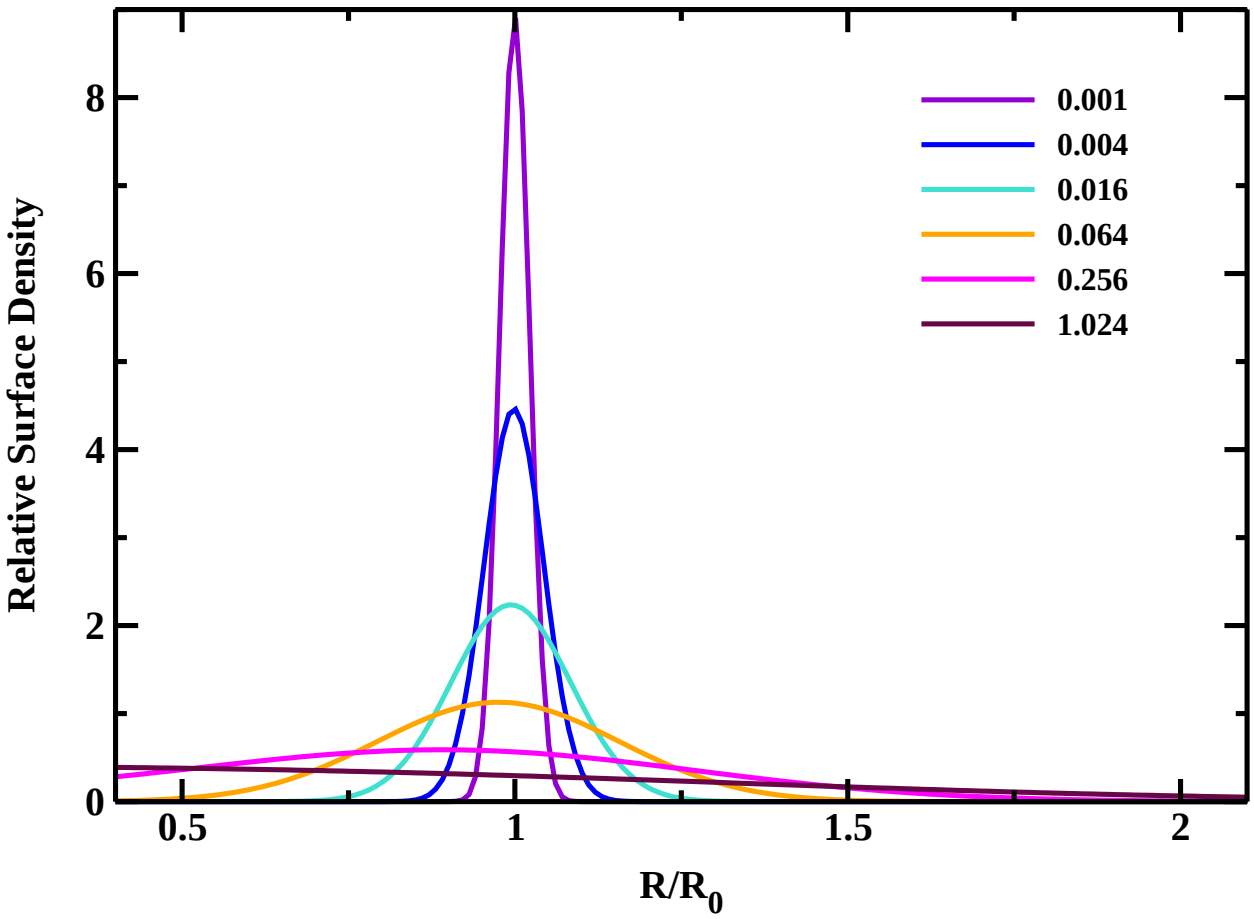

Fig. 2.— Time evolution of the surface density for a ring with constant viscosity (eq. [3-5]). Over time, viscous diffusion spreads the ring into a disk. The legend indicates the scaled time, τ, for each curve.

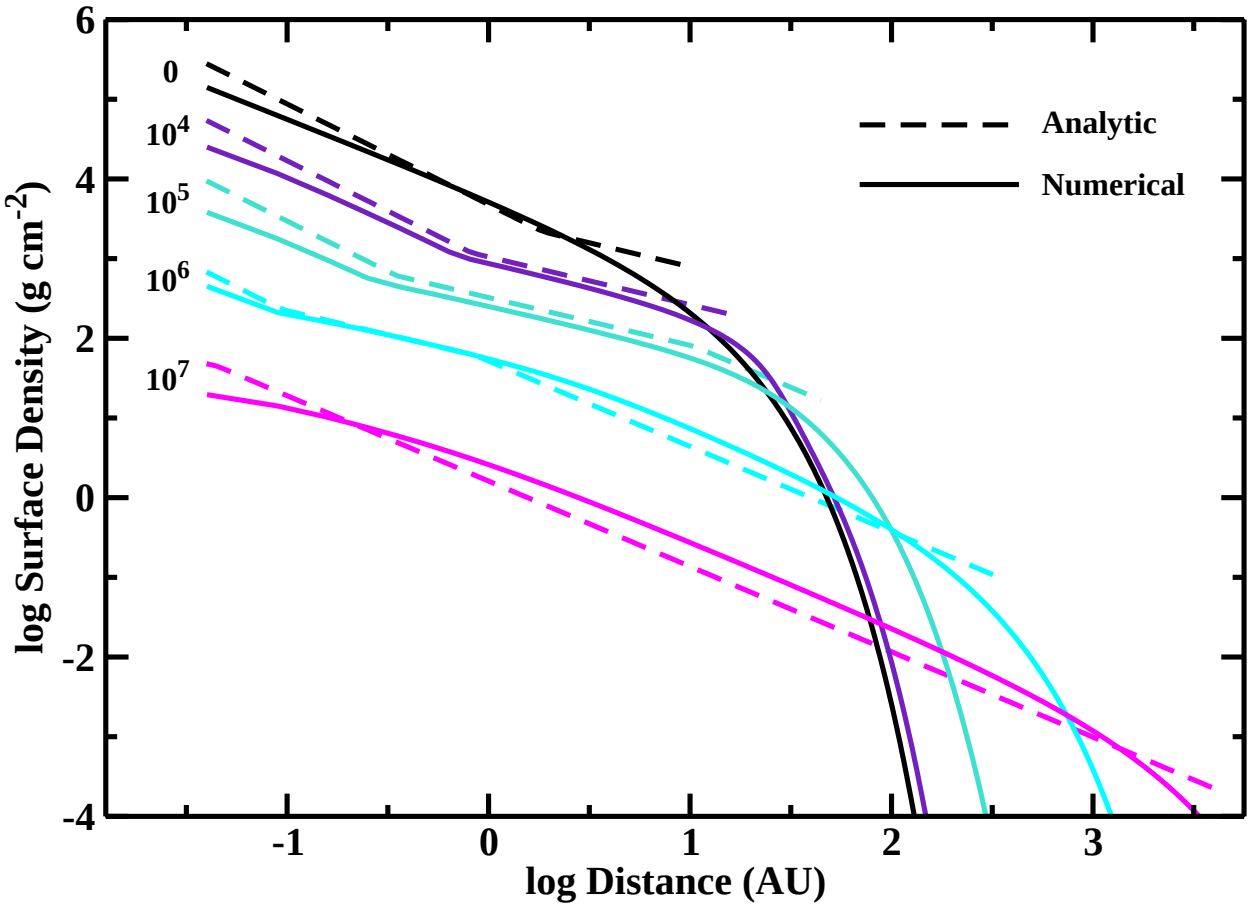

Fig. 3.— Time evolution of the surface density of a gaseous disk surrounding a 1 $M_\odot$ star. Dashed lines show results for the analytic disk model of Chambers (2009); solid lines show results for our numerical solution of the diffusion equation. Depsite small differences in the initial conditions, the numerical solution tracks the analytic model.

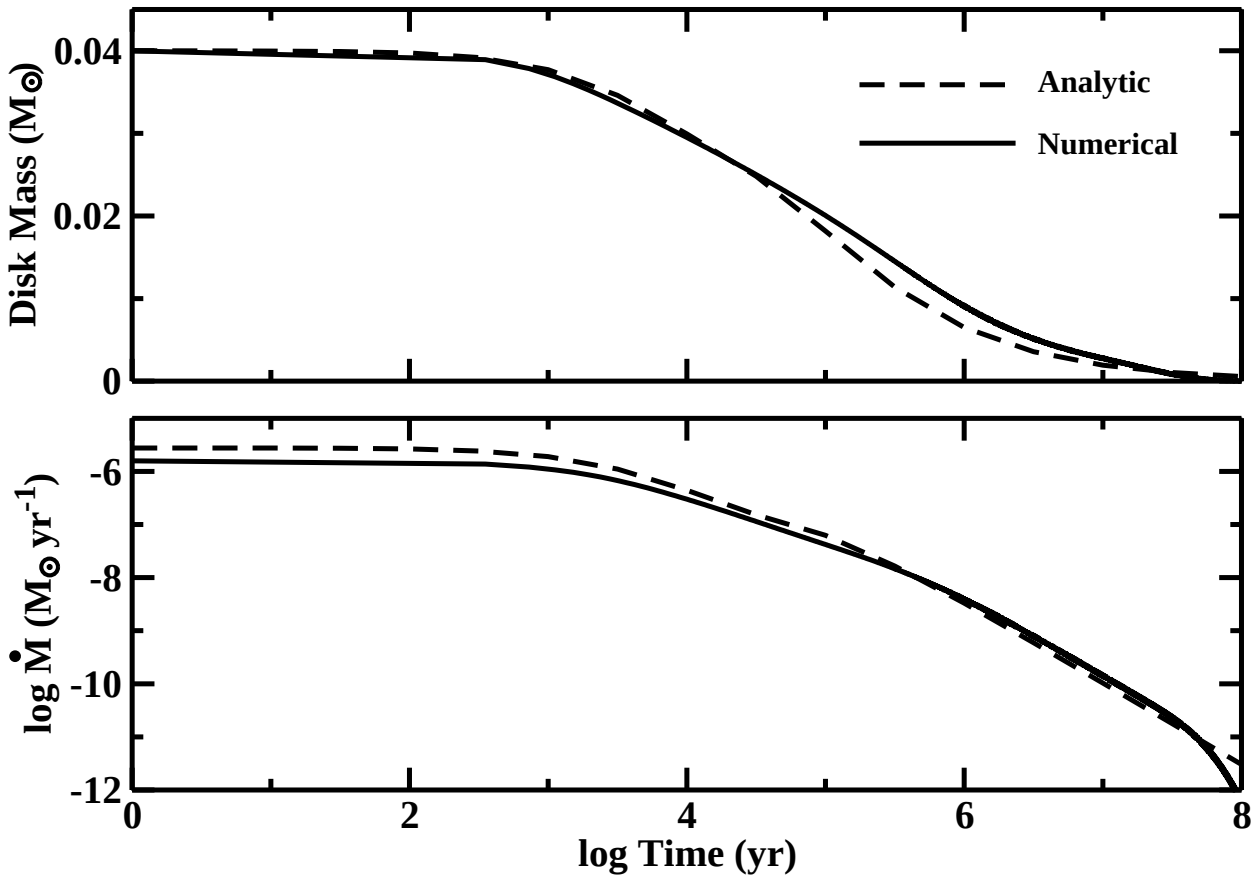

Fig. 4.— Time evolution of the disk mass (upper panel) and disk accretion rate onto the central star (lower panel) for the analytic and numerical solutions in Fig. 3.

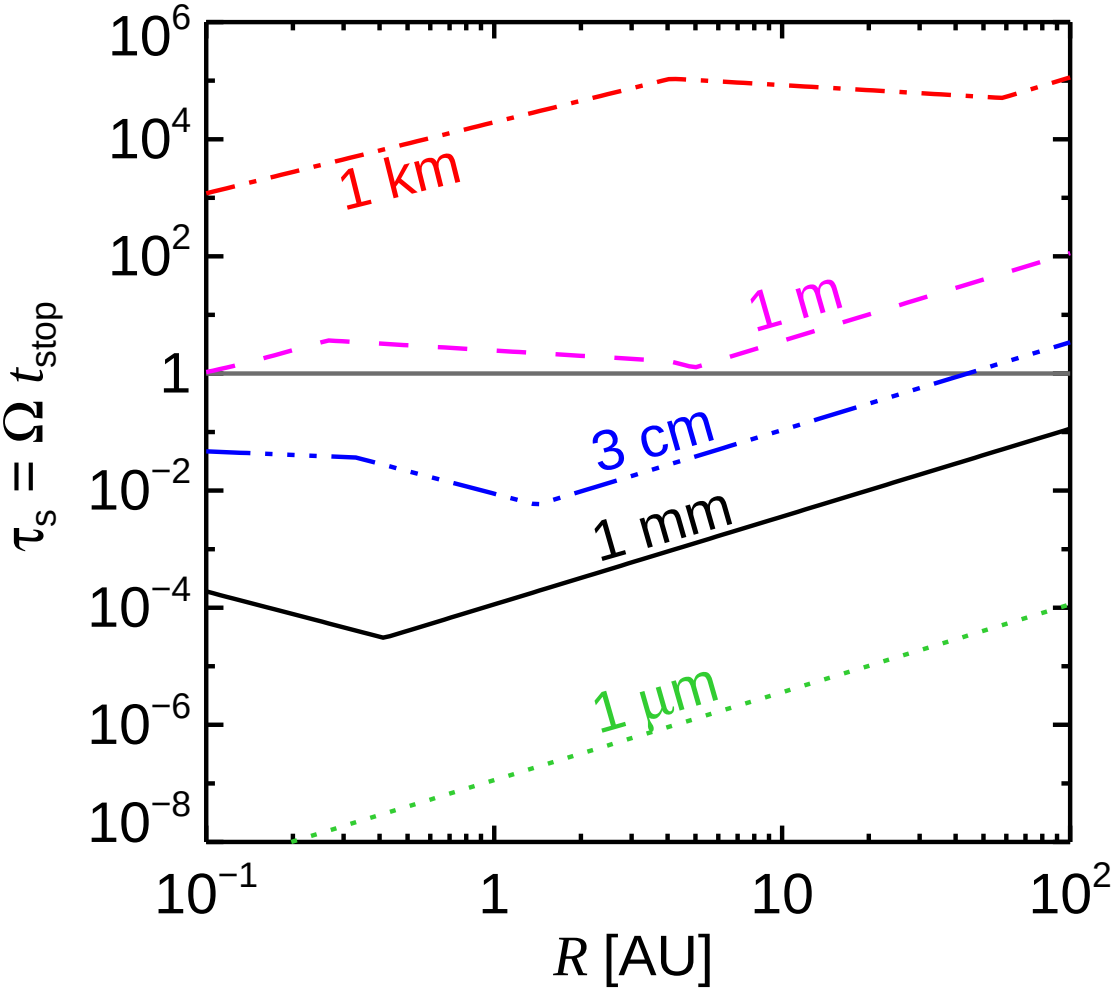

Fig. 5.— Aerodynamic stopping time normalized to the Keplerian orbital frequency for a range of particle sizes in our reference minimum mass disk model. Small (large) values of τ_s indicate strong (weak) coupling of solids to the gas disk. The breaks in the curves are due to transitions between different drag laws, as described by eq. (4-3). An internal density of $\rho_\bullet = 1\,\mathrm{g\,cm^{-3}}$ is assumed for the solids.

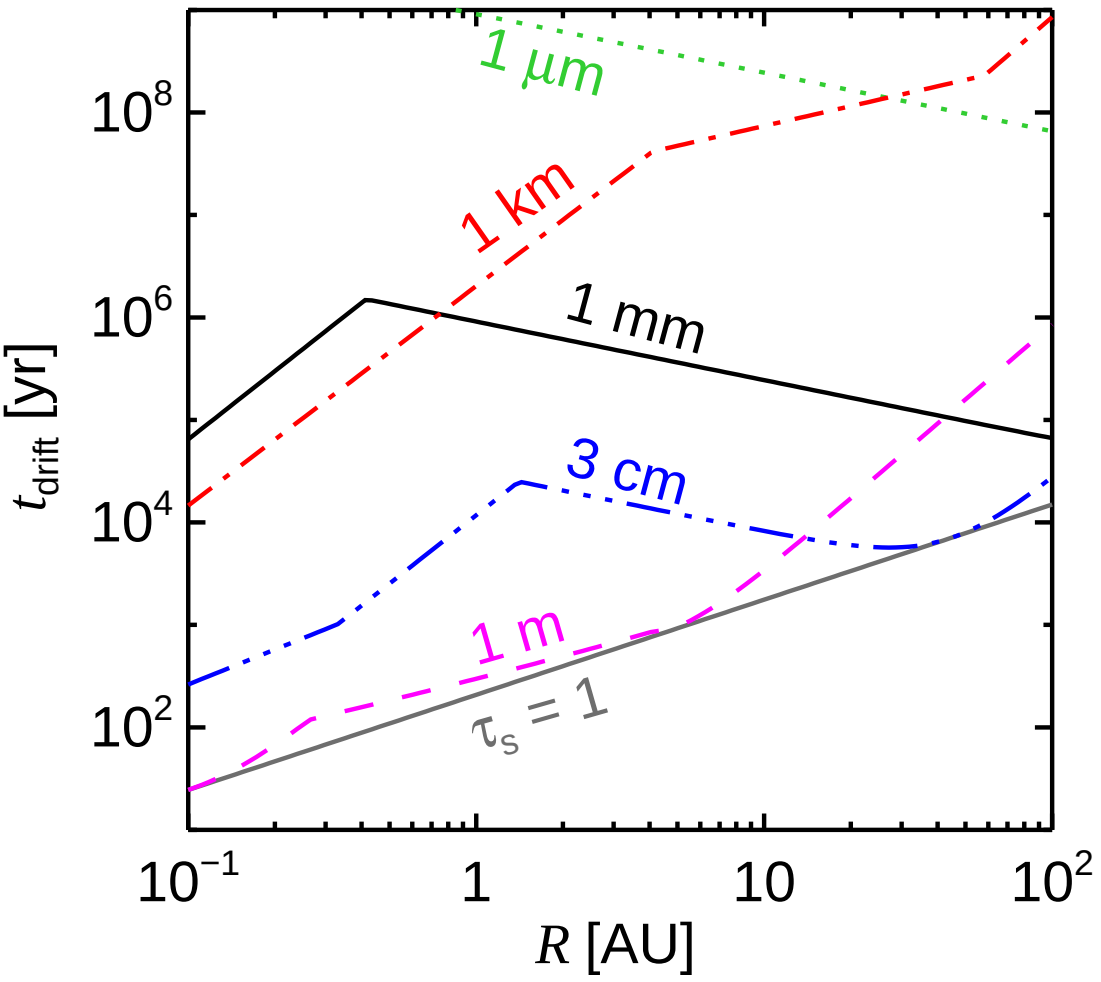

Fig. 6.— Radial drift timescales, $R/\dot{R}$, for the same disk models and particle sizes as in Fig. 5. The fastest drift timescale is for the particle size that has $\tau_s = 1$ as indicated by the grey curve. Drift timescales are much faster than disk lifetimes of a few Myr, especially near the "meter-sized" barrier.

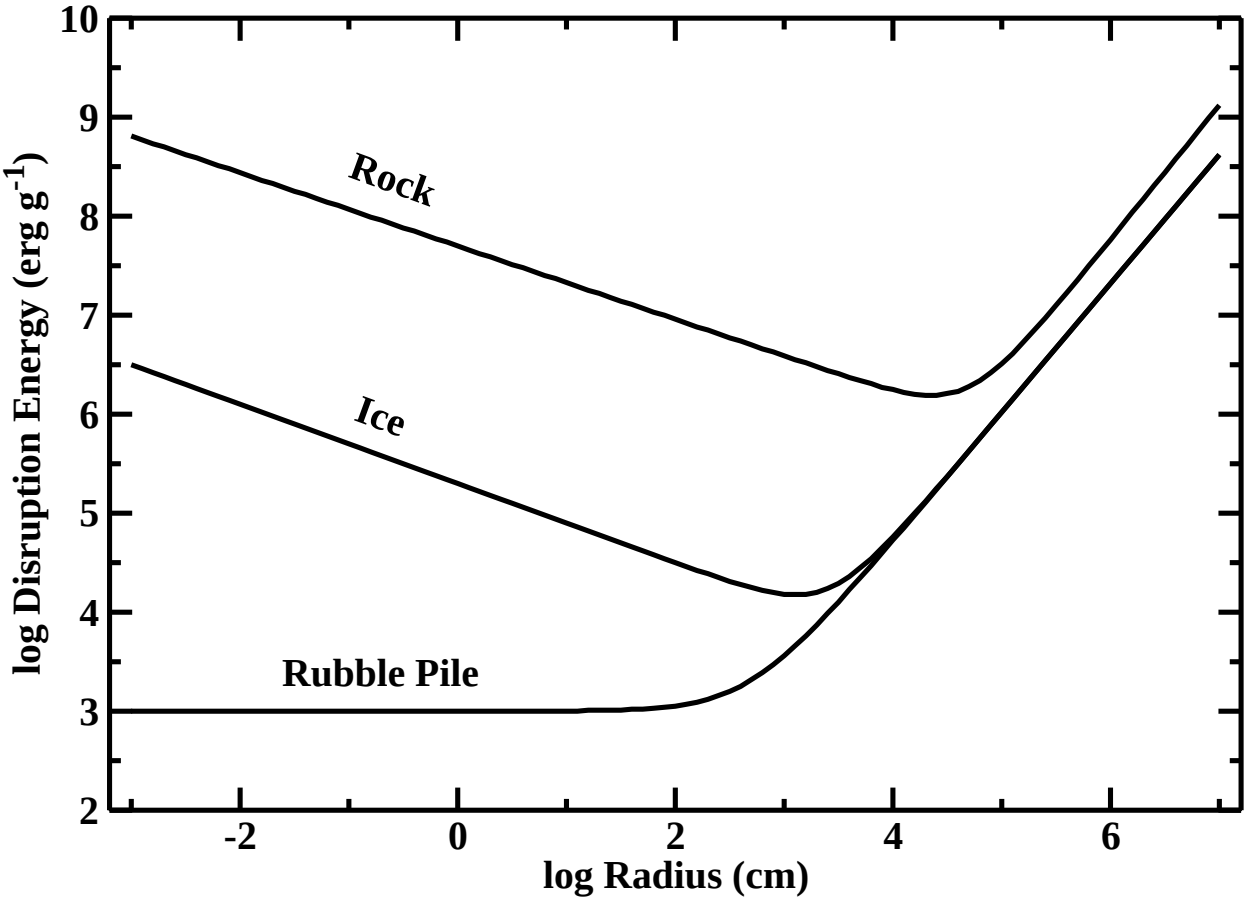

Fig. 7.— Disruption energy, Q_D^*, for icy objects. The solid curves plot typical results derived from numerical simulations of collisions (e.g., Benz & Asphaug 1999; Durda et al. 2004; Leinhardt & Stewart 2009) that include a detailed equation of state for basalt (rock) or crystalline ice (ice). In the strength regime ($r \lesssim 10^2$–10^4 cm), smaller particles are stronger. In the gravity regime ($r \gtrsim 10^5$ cm), larger objects are stronger. The "Rubble Pile" curve shows results consistent with model fits to comet breakups (e.g., Asphaug & Benz 1996).

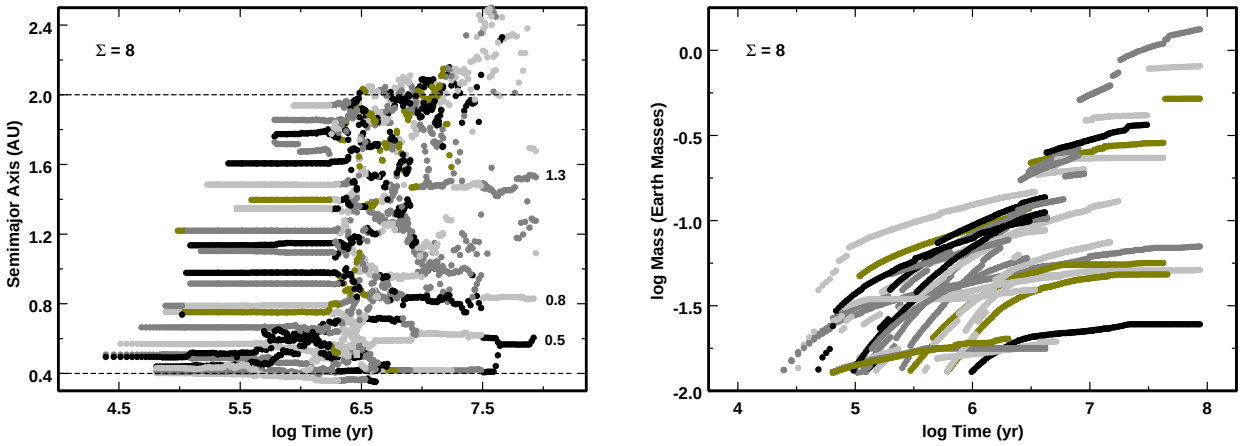

Fig. 8.— Evolution of oligarchs in the terrestrial zone. The calculation starts with 1 km planetesimals ($\rho_\bullet = 3$ g cm^{-3}) in a disk with $\Sigma_s = 8$ g cm^{-2} $(a/1 \text{ AU})^{-1}$. *Left panel:* The time evolution of semimajor axis shows three phases that start at the inner edge of the grid and propagate outward: (i) after runaway growth, isolated oligarchs with $m \gtrsim 4 \times 10^{25}$ g form and continue to grow very rapidly; (ii) oligarchs develop eccentric orbits, collide, and merge; and (iii) a few massive oligarchs eventually contain most of the mass and develop roughly circular orbits. The legend indicates masses (in $M_\oplus$) for the largest oligarchs. *Right panel:* The mass evolution of oligarchs shows an early phase of runaway growth (steep tracks) and a longer phase of oligarchic growth (flatter tracks), which culminates in a chaotic phase where oligarchs grow by captures of other oligarchs (steps in tracks). Despite the steeper appearance of some of the mass tracks during runaway growth, protoplanets grow more rapidly during oligarchic growth.

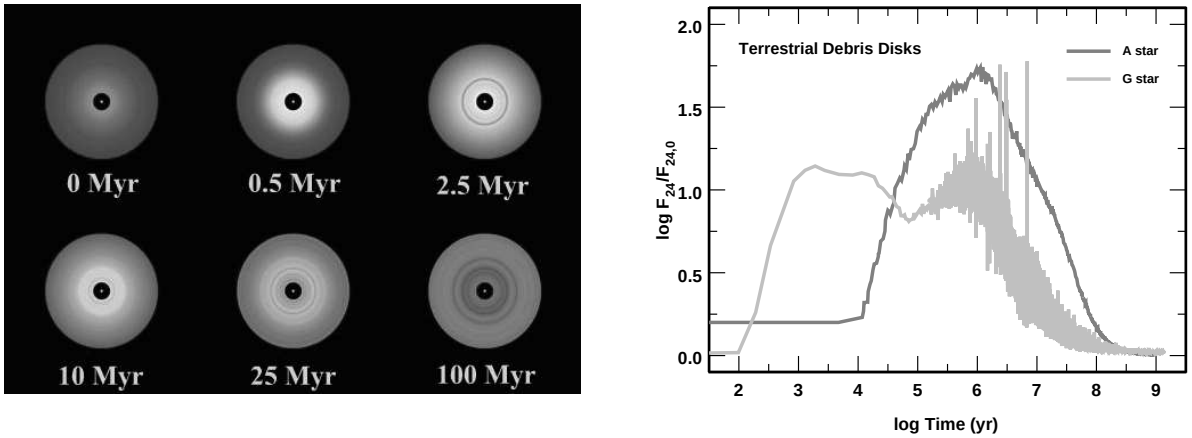

Fig. 9.— Evolution of debris disks in the terrestrial zone (Kenyon & Bromley 2004b, 2005). For an A-type star with a luminosity of $\sim 50\ L_{\odot}$, the range in blackbody temperatures of planetesimals at 3–20 AU (425–165 K) is similar to the range in the Solar System at 0.4–2 AU (440–200 K). *Left panel:* Images of a disk extending from 3–20 AU around an A-type star. The intensity scale indicates the surface brightness of dust, with black the lowest intensity and white the highest intensity. *Right panel:* Mid-IR excess for two debris disk models. The light grey line plots the ratio of the 24 μm flux from a debris disk at 0.4–2 AU disk relative to the mid-IR flux from a G-type star. The dark grey line shows the evolution for the A-star disk shown in the left panel.

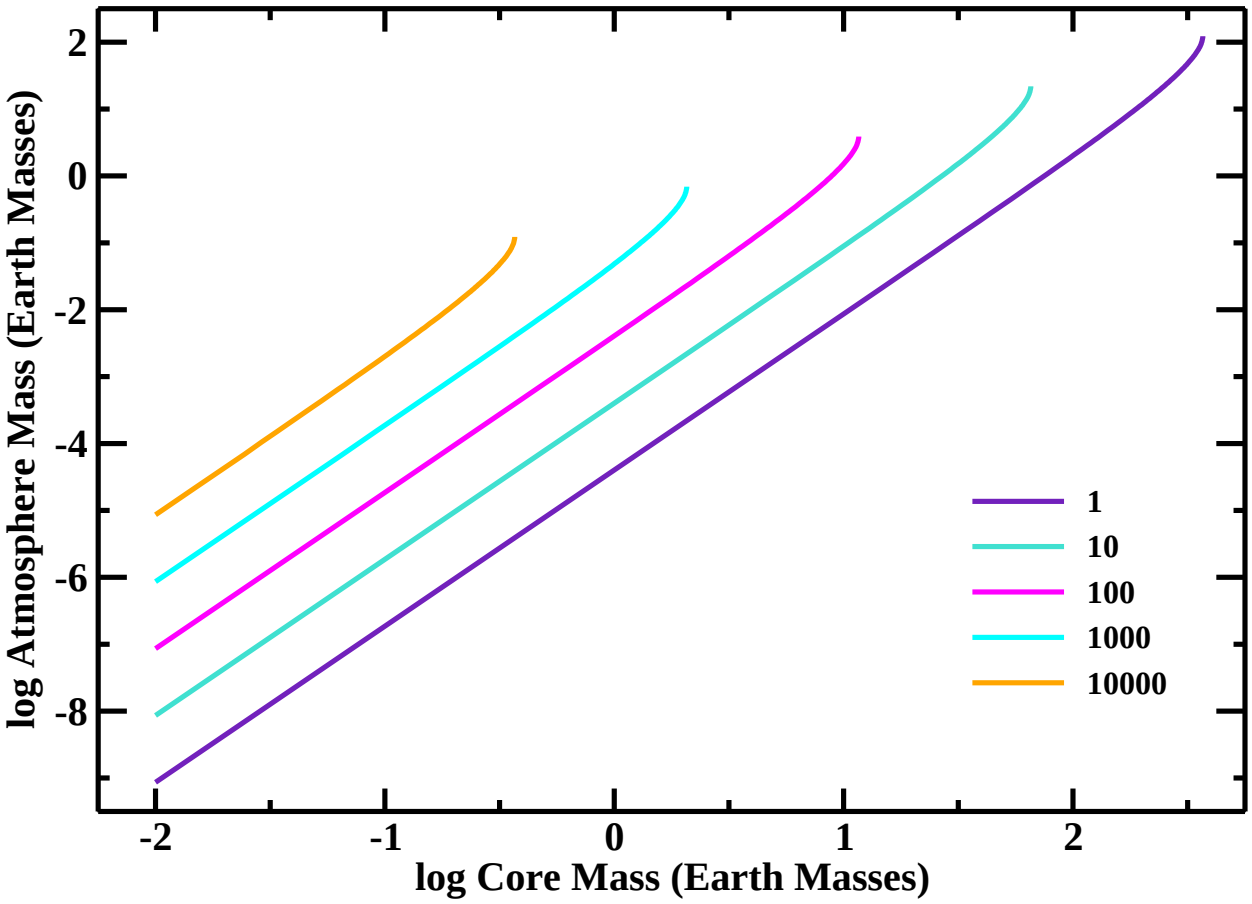

Fig. 10.— Mass of planet atmosphere as a function of core mass and accretion time (eq. [5-36]). The legend indicates the accretion time in Myr. At fixed core mass, the mass of the atmosphere grows with the accretion time. Longer accretion times allow more massive cores to have hydrostatic atmospheres.

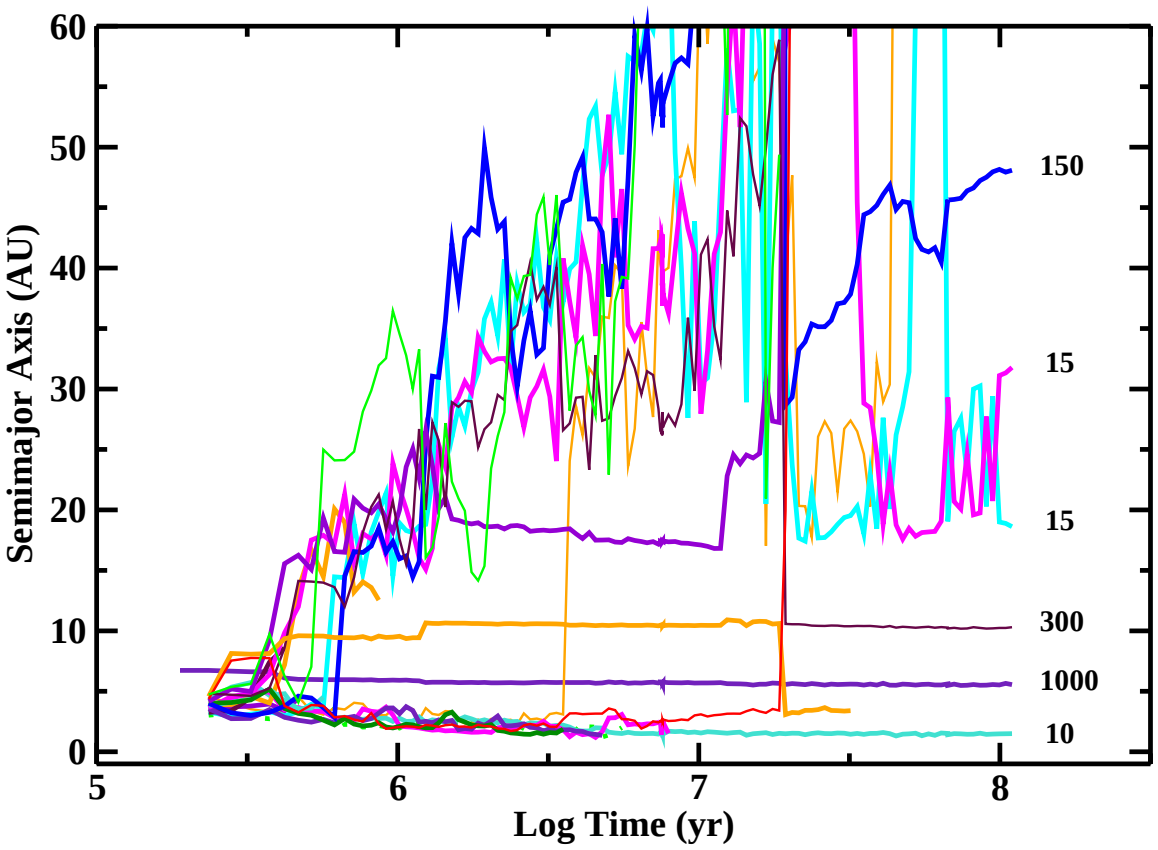

Fig. 11.— Orbital evolution of icy oligarchs. The calculation starts with 1 cm and 1000 km planetesimals ($\rho_\bullet$ = 1.5 g cm^{-3}) in a disk with initial Σ_s = 14g cm^{-2} $(a/3\ \mathrm{AU})^{-1} e^{-a/30\ \mathrm{AU}}$. During the first 3×10^5 yr, $\sim$ 20 oligarchs with $m \approx 0.05$ M$_\oplus$ form in a relatively narrow range of semimajor axis, 3–7 AU. As they grow, more massive oligarchs scatter lower mass oligarchs to large semimajor axes, $a \approx$ 1–20 AU. At $\sim$ 1 Myr, some oligarchs begin to accrete gas. Over the next 10 Myr, continued growth and scattering leads to collisions and mergers of oligarchs. Eventually, only a few oligarchs remain. The largest of these have masses comparable to the mass of Jupiter. The legend indicates masses (in $M_\oplus$) for the largest oligarchs in stable orbits around the central star.

Table 1:: Frequently Used Symbols

Symbol	Ref.	Meaning
General Physical Quantities		
AU	eq. (2-1)	astronomical unit
c	eq. (2-8)	speed of light
c_s	eq. (3-3)	sound speed
C_D	eq. (4-4)	drag coefficient
C_v	§3.2	specific heat
P	eq. (3-2)	gas pressure
t		time or timescale, often subscripted
T [$T_{\rm eq}$]	eq. (2-5)	[equilibrium] temperature
v_K	eq. (3-3)	Keplerian circular velocity
γ	eq. (3-3)	adiabatic index
κ	eq. (3-33)	radiative opacity
λ	eq. (2-6), §3.6	wavelength (light or other waves)
λ	§3.2, eq. (4-3)	gas mean free path
μ	§3.2	mean molecular weight
σ	§3.2	cross section
$\sigma_{\rm SB}$	eq. (3-23)	Stephan-Boltzmann constant
ρ		density (mass per volume) of quantity, often subscripted
$\rho_\bullet$	eq. (2-8)	Internal density of solid grain or planetesimal
Ω	§3.1	Keplerian orbital frequency
Stellar Quantities		
$\rm L_\star$ [$\rm L_\odot$]	eq. (2-5)	stellar [solar] luminosity
$l_\star$	eq. (5-26)	$\rm L_\star/L_\odot$, dimensionless stellar luminosity
$\rm M_\star$ [$\rm M_\odot$]	eq. (2-9)	stellar [solar] mass
$m_\star$		$\rm M_\star/M_\odot$, dimensionless stellar mass
$Z_{\rm Fe}$	eq. (2-9)	stellar metallicity
Disk Quantities		
D	eq. (3-18)	Dissipation (i.e. heating) rate, per area
F	eq. (2-1)	Disk mass relative to MMSN
H	eq. (3-13)	disk scaleheight
J [$\dot{J}$]	eq. (3-10)	angular momentum [torque]
$L_{\rm acc}$ [$L_{\rm d}$]	eq. (3-21) [eq. (3-19)]	Accretion luminosity [part released in the disk]
$\dot{M}$	eq. (3-1)	accretion rate through disk
Q	eq. (3-34)	dimensionless measure of gravitational stability
R	eq. (2-1)	distance from star (cylindrical radius)
$R_{\rm in}$	eq. (3-19)	radius of disk inner edge
R_J	eq. (3-17)	torque on inner disk edge, as length-scale
v_ϕ [v_R]	eq. (3-1)	orbital [radial] flow velocity
$Z_{\rm disk}$	eq. (2-2)	Disk "metallicity" as ratio of solids to gas

Table 1:: Frequently Used Symbols

Symbol	Ref.	Meaning
$Z_{\rm rel}$	eq. (2-4)	"Metallicity" relative to fiducial Solar value of 0.015
α	eq. (3-14)	dimensionless angular momentum transport coefficient
α_D	eq. (4-12)	dimensionless turbulent diffiusion coefficient
η	eq. (4-1)	fraction by which rotation is slower than Keplerian
θ	eq. (3-26)	grazing angle of starlight on disk surface
ν	eq. (3-4)	viscosity, usually "anomalous"
$\rho_{\rm R}$	eq. (4-13)	Roche density for gravitational binding
Σ	eq. (2-1), eq. (3-1)	Surface density (mass per area) of disk, e.g. gas (§3) or planetesimals (§5.1). Subscripted as needed.
Σ_g [Σ_p]	eq. (2-1) [eq. (2-2)]	Surface density of gas [particle] disks.
$\dot{\Sigma}$	eq. (3-4)	Inflow or outflow of mass from disk, per area
Protoplanet Quantities		
a	eq. (5-1)	semimajor axis (similar to disk R)
B	eq. (5-12)	width of feeding zone in R_H
f_G	eq. (5-7) & (5-10)	gravitational focusing factor for collisional cross section
m [m_c , m_a]	§5.1 [§5.2.1]	protoplanet mass, total or [core, atmosphere]
m_s [m_l]	§5.1	mass of small protoplanets, i.e. planetesimals [larger protoplanets]
$m_{\rm iso}$	eq. (5-12)	isolation mass
$\dot{m}$ [$\dot{m}_l$]	§5.1.2	accretion rate, for [large] protoplanet's mass growth
Q_D^*	eq. (5-18)	energy (per mass) threshold for catastrophic collisional disruption
r [r_s , r_l , r_c]	§5.1 , §5.2.1	radius of protoplanet [small, large, solid core]
$r_{\rm B}$	eq. (5-24)	Bondi radius for planet gravity to exceed thermal energy of disk gas
R_H	eq. (5-1)	Hill radius for planet gravity to dominate stellar tides
s	eq. (4-3)	radius of small grain or planetesimal
$t_{\rm s}$ [$\tau_{\rm s}$]	eq. (4-3) [eq. (4-5)]	[dimensionless] aerodynamic stopping timescale
v [v_s , v_l]	§5.1	velocity dispersion of [small, large] protoplanets
v_{esc} [v_H]	eq. (5-4) [eq. (5-3)]	escape speed from protoplanet's surface
Σ_s [Σ_l]	§5.1	surface mass density of small [large] protoplanets
χ	eq. (5-35)	log ratio of atmosphere to core radius
ψ	eq. (5-2)	r/R_H, radius in Hill units